

**EXPERIMENTAL AND ANALYTICAL INVESTIGATION OF
LOCALIZATION AND POST-PEAK BEHAVIOR OF STEEL
MEMBERS IN TENSION**

A Dissertation

presented to

the Faculty of the Graduate School

at the University of Missouri-Columbia

In Partial Fulfillment

of the Requirements for the Degree

Doctor of Philosophy

by

SAIF ALTAI

JULY 2019

ACKNOWLEDGEMENTS

I would sincerely like to thank my advisor Dr. Sarah Orton, co-advisor Zhen Chen for their expertise, ideas, time, feedback and support in carrying out this project work.

I would also like to acknowledge Dr. Gopal for his suggestions, guidance for making this dissertation even better.

I would like to express my gratitude to my family members (my parents, brother, sisters and father-in-law Anwer) who helped me, encouraged me and believed to get this work done perfectly.

Finally, huge thanks to my princess and my wife Sarah for her full support.

TABLE OF CONTENTS

ACKNOWLEDGEMENTS.....	ii
LIST OF FIGURES	vi
LIST OF TABLES.....	xii
ABSTRACT.....	xiv
CHAPTER 1: STATEMENT OF PROBLEM	1
1.1. Statement of Problem.....	1
1.2. Scope and Objectives.....	1
1.3. Contributions.....	2
1.4. Tasks	3
CHAPTER 2: LITERATURE REVIEW	5
2.1. Background.....	5
2.1.1. Post-Peak Behavior	5
2.1.2. Bifurcation	7
2.1.3. Localization Length	9
2.1.4. Size Effect.....	14
2.2. Numerical Models.....	15
2.3. Local models.....	16
2.4. Nonlocal Models.....	17
2.5. Recent Nonlocal models	18
2.6. Summary.....	22
CHAPTER 3: EXPERIMENTAL PROCEDURE AND RESULTS.....	23
3.1. Introduction.....	23
3.2. 3D DIC Setup.....	24
3.3. Specimens	31
3.4. Test Setup.....	31
3.5. Experimental Results	36
3.5.1. Engineering Strain Profile.....	39
3.6. Determination of Localization Length.....	43
3.6.1. Average Strain Method	43
3.6.2. Longitudinal Strain method	44
3.7. Evolution of Localization Length.....	46

3.8.	Stress Strain Behavior of Localization Length	50
3.9.	Summary of Localization Length Methods	55
3.10.	Strain Rate.....	56
3.11.	Summary and Conclusions	58
CHAPTER 4: ANALYTICAL AND NUMERICAL ANALYSIS		61
4.1.	Introduction.....	61
4.2.	Previous Experimental Results	63
4.3.	Numerical Localization Model	66
4.3.1.	Pre-Peak Behavior.....	67
4.3.2.	Post-Peak Behavior	69
4.3.3.	Bifurcation point	71
4.3.4.	Linear Post-Peak Model.....	76
4.3.1.	Bilinear Post-Peak Model	78
4.3.1.	Nonlinear Post-Peak Model	79
4.3.1.	Comparison of Numerical Post-Peak Models with Experiments.....	81
4.4.	Finite Element Analysis (FEA).....	84
4.4.1.	Modeling	85
4.4.2.	Geometrical and Material Properties	86
4.4.3.	Meshing.....	88
4.4.4.	Results.....	91
4.4.5.	Comparison the FEA Model with The Experiments.....	92
4.5.	Summary and Conclusions	96
CHAPTER 5: INFLUENCE OF THE POST-PEAK BEHAVIOR ON COLLAPSE OF STRUCTURAL SYSTEMS		99
5.1.	Introduction.....	99
5.2.	Analytical Study.....	100
5.2.1.	Analytical Models	101
5.2.1.1.	Bilinear Post-peak Model.....	102
5.2.1.2.	Modified Ramberg and Osgood Relationship.....	103
5.2.1.3.	Nonlinear Curve Fitting	103
5.2.2.	System Analysis	104
5.2.2.1.	V-Truss.....	104
5.2.2.2.	Tension Members in Parallel.....	108
5.2.3.	Analytical Conclusions	111

5.3.	Experimental Study.....	112
5.3.1.	Test Setup.....	114
5.3.2.	Experimental Results	116
5.3.2.1.	Single Member Tests.....	116
5.3.2.2.	Parallel Tension Tests	118
5.3.3.	Comparison of Numerical Bilinear Post-Peak Model with Experiments	124
5.4.	Summary and Conclusions	126
CHAPTER 6: CONCLUSIONS AND FUTURE WORK.....		128
6.1.	Summary.....	128
6.2.	Conclusions.....	129
6.3.	Future work.....	132
REFERENCES		133
VITA.....		139

LIST OF FIGURES

Fig. 2.1. Idealized load-displacement curve highlighting the post-peak region.....	6
Fig. 2.2. (a) Force-displacement curve, (b) undeformed specimen, (c) deformed specimen following the primary path (d) deformed specimen following the bifurcation path, and (e) longitudinal strain profile of specimen following bifurcation or primary path.	8
Fig. 2.3. (a) The behavior of longitudinal strain along x-axis after the peak load and (b) post-peak behaviors of three members of different lengths.....	10
Fig. 2.4. Effect of L_c on (a) lateral force versus displacement; (b) curvature distribution for peak lateral displacement of 250 mm (Sideris and Salehi 2016).....	11
Fig. 2.5. (a) Four loading instants along the post-peak region and (b) longitudinal strain at the four loading instants.....	13
Fig. 2.6. Evolution of localized length for simulations with different diameters and hardening (Kolwankar et al. 2017)	14
Fig. 2.7. The engineering stress-strain curves for different n ($n=L_c/L$) (Dai et al. 2011).	15
Fig. 2.8. Fiber-based simulation of localization processes through softening constitutive models (Kolwankar et al. 2017).....	17
Fig. 2.9. Engineering stress-strain response for cylindrical steel bar under tension from FEA and line model for (a) local formulation and (b) nonlocal formulation	20
Fig. 2.10. Longitudinal strain distribution for cylindrical steel bar under tension from FEA and line model for (a) local formulation and (b) nonlocal formulation (Kolwankar et al. 2017).....	20
Fig. 2.11. Schematic illustration of research methodology and components (Kolwankar et al. 2018)	21

Fig. 3.1. Random Speckle pattern.....	25
Fig. 3.2. Calibration card	27
Fig. 3.3. Region of Interest	28
Fig. 3.4. Facets and grid points.....	29
Fig. 3.5. Dimensions of steel specimen.	31
Fig. 3.6. Experimental Setup	33
Fig. 3.7. (a) Extensometer placed on 3 in. steel specimen, and (b) 3D DIC versus extensometer	34
Fig. 3.8. All tested specimens after rupture	34
Fig. 3.9. Sample result just before rupture.....	35
Fig. 3.10. Average of engineering stress vs. strain for specimens with the same length .	37
Fig. 3.11. Engineering stress vs. strain for all tested specimens	38
Fig. 3.12. Longitudinal engineering strain along length of specimen at rupture load.	40
Fig. 3.13. Transverse engineering strain along length of specimen at rupture load.	40
Fig. 3.14. (a) Engineering stress-strain curve of 24D-2 specimen, and (b) longitudinal Engineering strain.	42
Fig. 3.15. Determination of localization length using average strain method and (data from 12D-1 specimen).....	45
Fig. 3.16. Determination of localization length using longitudinal strain method (data from 12D-1 specimen).....	45
Fig. 3.17. The evolution of the localization length (a) and (b) Average strain method and	49

Fig. 3.18. Engineering stress-strain along localization zone calculated by average strain method at rupture load	52
Fig. 3.19. Engineering stress-strain along localization zone calculated by longitudinal strain method at bifurcation point.....	52
Fig. 3.20. Engineering stress-strain of instantaneous localization zone determined by average strain method	54
Fig. 3.21. Engineering stress-strain of instantaneous localization zone determined by longitudinal strain method.	54
Fig. 3.22. Strain rate at the center and outside the localization zone of 12D-1 specimen	57
Fig. 3.23. Strain rate for steel specimens with four different lengths.....	57
Fig. 3.24. Engineering stress vs strain at fracture location and a point outside the localization zone of 3D-1 specimen.....	58
Fig. 4.1. Engineering stress vs. strain for cylindrical steel specimens	64
Fig. 4.2. Determination of softening factor based on engineering stress-strain inside the localization zone determined by (a) average strain method and (b) longitudinal strain method.....	65
Fig. 4.3. (a) Description of localization zone in the numerical model, and (b) engineering strain distribution in localization model	67
Fig. 4.4. Constitutive relationship for segment A and B (a) linear post-peak, (b) bilinear post-peak and (c) nonlinear post-peak models.....	71
Fig. 4.5. Load displacement response (a) linear post-peak, (b) bilinear post-peak and (c) nonlinear post-peak models	71
Fig. 4.6. Engineering stress-strain relationship inside and outside the localization zone	72

Fig. 4.7. Strain rate inside and outside the localization zone	75
Fig. 4.8. Displacement between the peak load and the bifurcation vs specimen length ..	75
Fig. 4.9. Linear post-peak model of 12D-1 specimen	77
Fig. 4.10. Bilinear post-peak model of 12D-1 specimen.....	79
Fig. 4.11. Nonlinear post-peak model of 12D-1 specimen.....	81
Fig. 4.12. Comparison the load-displacement of experiments and linear, bilinear and nonlinear post-peak numerical localization models.....	83
Fig. 4.13. Geometry and meshing of one eighth of 3D specimen	87
Fig. 4.14. Experimental and calibrated true Stress-Strain	88
Fig. 4.15. Load displacement of FEA results of different mesh size.....	89
Fig. 4.16. Longitudinal engineering strain profile of 3D specimen with different mesh sizes at rupture load	90
Fig. 4.17. Meshing of one eighth of 6D specimen.....	90
Fig. 4.18. Load displacement of experiments and FEA results	93
Fig. 4.19. Longitudinal engineering strain profile of 12D specimen.....	95
Fig. 4.20. Experimental and FEA longitudinal engineering strain profile of 3D specimen	96
Fig. 4.21. Specimen before rupture, red line represents FEA simulation.....	96
Fig. 5.1. Example rotation in structural system due to unsymmetrical failure (Bondok 2017)	100
Fig. 5.2. V-Truss under tension	105
Fig. 5.3. Load vs. vertical displacement of 24D members	107
Fig. 5.4. Load versus lateral displacement of 1% imperfection and 24D members	107

Fig. 5.5. Influence of initial imperfection on lateral displacement of V truss of 24D members.....	108
Fig. 5.6. Tension members in parallel	109
Fig. 5.7. Load versus vertical displacement of 24D members.....	110
Fig. 5.8. Load versus rotation of 1% imperfection and 24D members.....	110
Fig. 5.9. Effect of initial imperfections on the rotation of 24D members in parallel	111
Fig. 5.10. Dimensions of steel specimen (triple tension test).....	113
Fig. 5.11. Three members in parallel.....	113
Fig. 5.12. Three specimens of one-member test after rupture	115
Fig. 5.13. Three members in parallel test after rupture	115
Fig. 5.14. Engineering stress vs. strain for single tension tests	117
Fig. 5.15. Longitudinal engineering strain along length of single tension tests at rupture load.....	117
Fig. 5.16. Load-displacement of all triple tension tests.....	120
Fig. 5.17. Load-displacement of specimens of Test-1	121
Fig. 5.18. Load-displacement of specimens of Test-2.....	121
Fig. 5.19. Load versus rotation of parallel tension tests	122
Fig. 5.20. Normalized displacement versus rotation of parallel tension tests	122
Fig. 5.21. Longitudinal engineering strain along length of specimens of Test-1 at rupture load.....	123
Fig. 5.22. Longitudinal engineering strain along length of specimens of Test-2 at rupture load.....	123

Fig. 5.23. Comparison the load-displacement of experiments (Test-1 and Test-2) and bilinear post-peak model..... 125

Fig. 5.24. Comparison the load-displacement of experiments (Test-3) and bilinear post-peak model with 0.5% initial imperfection..... 125

LIST OF TABLES

Table 3.1. Test Matrix	35
Table 3.2. Localization length determined by average strain and longitudinal strain methods	46
Table 3.3. Engineering strain and drop in load at the onset of the localization	50
Table 3.4. The slope secant of the softening curve of engineering stress strain curve of the localization zone	53
Table 3.5. Comparisons of average and longitudinal strain methods	55
Table 4.1 Localization length and softening factor determined by average strain and longitudinal strain methods.....	65
Table 4.2. Post-peak models versus determination of localization length methods	67
Table 4.3. Experimental and numerical displacement at rupture load (in)	84
Table 4.4. Experimental and numerical rupture load (kips).....	84
Table 4.5. Material properties used in simulation.....	87
Table 4.6. Convergence Study	89
Table 4.7. Experimental and FEA displacements at peak and rupture loads	91
Table 5.1. Nonlinear curve fitting parameters.....	104
Table 5.2. Single member tests	114
Table 5.3. Three members in parallel.....	114
Table 5.4. Localization length and softening factor determined longitudinal strain method	118
Table 5.5. Difference in diameters along the specimen to the diameter at the middle ..	118

Table 5.6. Maximum longitudinal engineering strain of every specimen of members in parallel at rupture load 124

Experimental and Analytical Investigation of Localization and Post-Peak Behavior of Steel Members in Tension

Saif Altai

Dr. Sarah Orton, Dissertation Advisor

Dr. Zhen Chen, Dissertation Co-advisor

ABSTRACT

Accurate simulation of extreme limit states in structures subjected to abnormal loads, earthquake, or blast requires detailed understanding of their post-peak behavior. In steel structures, these extreme-limit states are associated with local or global instability such as local buckling, tension necking, and fracture. Several methods have been developed to simulate such extreme limit states such as fiber models, hinge models, nonlocal models, and finite element analysis (FEA). However, disadvantages of these methods arise when the structural elements pass the peak response and experience post-peak softening. Furthermore, there is a lack of experimental data to validate the numerical solutions, especially for the nonlocal models. This research first looks at experimentally determining the localization length and its evolution throughout the loading history to study the effect of the length scale on the post-peak response of steel members. Second, linear, bilinear, and nonlinear post-peak localization models are developed and compared to experimental data. Third, a system of three steel members was investigated to evaluate how post-peak behavior in part of the system affects the remaining members.

For the first stage of this research, an experimental program on cylindrical steel specimens with four different lengths (3D, 6D, 12D and 24D where D is the diameter of 0.5 in.) were conducted and results recorded with a digital image correlation system (DIC).

The results show that the post-peak response becomes steeper as the length of the specimen gets longer. A novel method of determination of localization length (longitudinal strain method) shows that onset of the strain localization occurs after the peak load at the bifurcation point and while another method (average strain method) shows that the onset of the strain localization occurs well before the peak load. The evolution of the localization length determined by the longitudinal strain method versus the normalized strain and the engineering stress-strain curve of the instantaneous localization zone are approximately identical for specimens with different lengths. Furthermore, the localization length is not constant, but reduces as the member move through the post-peak region. The localization length for the longitudinal strain method was approximately 5 times the diameter at the bifurcation point and reduced to 0.6 times at rupture.

Based on the experimental results, numerical localization models for one-dimensional steel member subjected to monotonic tension were developed for linear, bilinear and nonlinear post-peak stiffnesses. The nonlinear post-peak model predicts the displacement at rupture load within a difference within 1%. A FEA model was also developed yet only was able to achieve a displacement at rupture load within 12%. This was due to the 50% difference between the maximum experimental and simulated longitudinal engineering strain at the rupture load. The FEA model which uses an isotropic strain hardening law causes the localized necking to occur at the peak load not at the bifurcation point as in the experiments.

The response of a system of steel tension members was investigated analytically and experimentally to evaluate the effect of post-peak response on load redistribution and overall movements of the system. The analytical results showed that the members with

even a slight imperfection (i.e. 0.001%) can cause lateral displacement or rotation when one member fails before the others. The experimental results showed that the system in which only one member softening did so at a load 10% higher and at displacement 21% less than the system with two softening members. Both of these results indicate that even slight variations can cause significant effects in the failure response of a structural system. The numerical localization model was applied to the system analysis and showed the difference in displacement at the failure load between the numerical simulations and the experiments was 4%.

CHAPTER ONE

CHAPTER 1: STATEMENT OF PROBLEM

1.1. Statement of Problem

Simulation of structural collapse has been a challenging topic for decades. Such simulations require detailed understanding of the extreme limit states. These states are associated with the material and geometrical instabilities. In steel structures, for example, necking and buckling are the main factors that cause the structural elements to fail and may lead to a progressive collapse. Several methods have been developed to simulate such extreme limit states such as fiber models, hinge models, non-local models, and finite element analysis (FEA). However, disadvantages of these methods arise when the structural elements pass the peak response and experience post-peak softening. The post-peak behavior is important in understanding the way the load redistributes from one member to others and how that proceeds to structural collapses or even prevents it from happening. Therefore, accurate yet easily implemented models based on experimental data are needed to improve the simulation of structures during collapse.

1.2. Scope and Objectives

The overall goal of this research is to improve understanding of structural response during extreme limit states and collapse through improved simulation capabilities during post-peak response. This research focuses on localized necking caused by tension. Localized necking is triggered by the strain localization which plays a significant role in the post-peak response. The specific objectives of this research are:

- Evaluate localization length and evolution of localization length through experimental testing of cylindrical steel bars at different length scales.
- Develop and evaluate a new method to determine the localization length based on experimental data.
- Develop a simple analytical formulation to predict post-peak behavior of steel member under tension.
- Evaluate the influence of post-peak response on load redistribution of collapsing structures.

1.3. Contributions

This research provides many unique and new contributions to the area of structural engineering and our ability to understand and simulate the collapse of structures. The specific contributions that this research provides are:

- A new method to determine the localization length based on experimental data. This research developed the longitudinal strain method as a way to define the length of the localization zone during each point in the post-peak response.
- Experimental data to evaluate localization length and evolution of localization length. This research provides new experimental data specifically considering the measurement of axial and transverse strain of a specimen while in the post-peak region. This data was used to examine the evolution of the localization length during post-peak response.

- A new analytical formulation to predict post-peak behavior of steel member under tension. This research used the experimental data to develop a new analytical formulation for the post-peak response of steel in tension that can accurately predict the post-peak behavior yet eliminate the drawbacks of mesh dependency.
- Experimental data on the influence of post-peak response on load redistribution. This research conducted new experimental tests designed to investigate the influence of post-peak response on the load distribution of steel members in series.

1.4. Tasks

In order to accomplish the goals and objectives of the research, the following tasks were performed.

- Experiments were conducted to study the influence of length scale on the post-peak response of four different lengths of cylindrical steel bars subjected to tension. By using a digital image correlation measurement system, experimental data of the longitudinal and transverse engineering strain were obtained, and the localization length was evaluated using a newly developed method and compared to a previous method. The results of these tasks are presented in Chapter 3.
- An analytical model was formulated to efficiently capture the post-peak of one-dimensional steel members was developed to capture linear, bilinear, and nonlinear post-peak behavior. The new analytical formulation was compared to existing finite element analysis methods. The results of these tasks are presented in Chapter 4.
- Experiments were conducted to study the load redistribution of three steel bars in series under tension. The experimental results are compared to the predictions of

the new analytical method and existing finite element methods. The results of these tasks are presented in Chapter 5.

CHAPTER TWO

CHAPTER 2: LITERATURE REVIEW

2.1. Background

This chapter focuses on giving a background of post-peak behavior, bifurcation, localization length (L_c) and its evolution, and important models of prediction post-peak response of structures. Furthermore, a comprehensive survey of the strain softening with localization gives background needed to understand the nature of the post-peak behavior of structural elements. A literature review will be presented on the simulations of the post-peak behavior with numerical models.

2.1.1. Post-Peak Behavior

The post-peak region, as depicted in Fig. 2.1, is the descending region of the load displacement curve. In the post-peak region, deformation increases under decreasing load until the rupture load is reached. The post-peak region exists only in cases where the load can be reduced as the structure deforms. Such behavior often occurs in statically indeterminate structures. After the peak load is reached, continued deformation in the member allows for load reduction due to redistribution of load to other members until an ultimate elongation occurs. The post-peak behavior plays a key role in evaluating the collapse progression of a structure, and thus a thorough understanding of the post-peak behavior is needed.

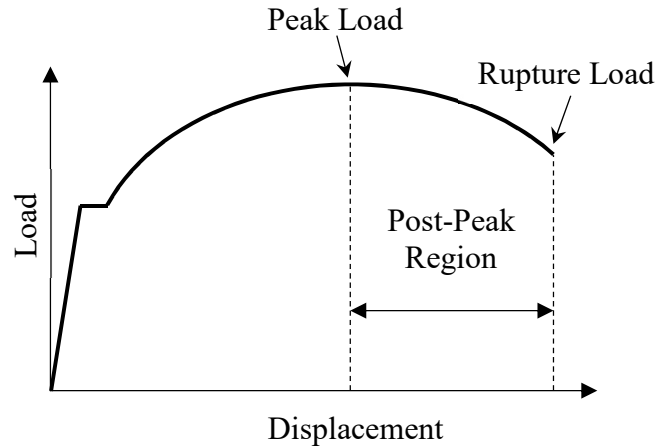


Fig. 2.1. Idealized load-displacement curve highlighting the post-peak region.

The post-peak behavior is characterized by strain localization. Strain localization is the increase in strain within a subsection of a member while outside of that section the strain may decrease. Strain localization often occurs when the material reaches its maximum stress state. Strain localization can occur in both brittle (such as rock and concrete) and ductile (such as steel and copper) materials. For concrete, strain localization occurs in tension (Elices and Planas 1989) and compression (Jansen and Shah 1997; Markeset and Hillerborg 1995), respectively. Strain localization can occur in concrete due to evolution of damage (micro-cracking), and the transition from micro-cracking to macro-cracking might lead to the snapback in the load-displacement space in case of high strength concrete specimens of short length (Jansen and Shah 1997). For steel, strain localization occurs in both compression (buckling) and tension (necking) (Kolwankar et al. 2017). Most of the post-peak behavior is determined by the bifurcation path which is explained in the next section.

2.1.2. Bifurcation

The bifurcation is characterized by a point on the load displacement curve where more than one equilibrium path can be followed (Bigoni, 2012). It represents the point at which strain localization occurs. For a cylindrical steel bar subjected to tension as shown in Fig. 2.2b, where x-axis is the longitudinal axis and y-axis is the transverse axis, two equilibrium paths are considered for demonstration (see Fig. 2.2a). Fig. 2.2e shows the longitudinal strain profile for both possible paths. One path represents the uniform strain across the bar length (primary or homogeneous path) consistent with the uniform specimen deformations shown in Fig. 2.2c. The other shows an inhomogeneous (secondary) deformation path where localized necking occurs as shown in Fig. 2.2e consistent with deformations in Fig. 2.2d. The path where strain localizes into a segment occurs because it provides a larger increase of internally produced entropy, according to thermodynamic stability analysis (Bažant and Cedolin, 2010). At bifurcation, hence, the primary path that maintains the uniform strain field becomes impossible and the bifurcation (secondary) of equilibrium path must happen. The bifurcation point and the point of peak load are not always the same. This research will experimentally determine the bifurcation point in cylindrical steel specimens.

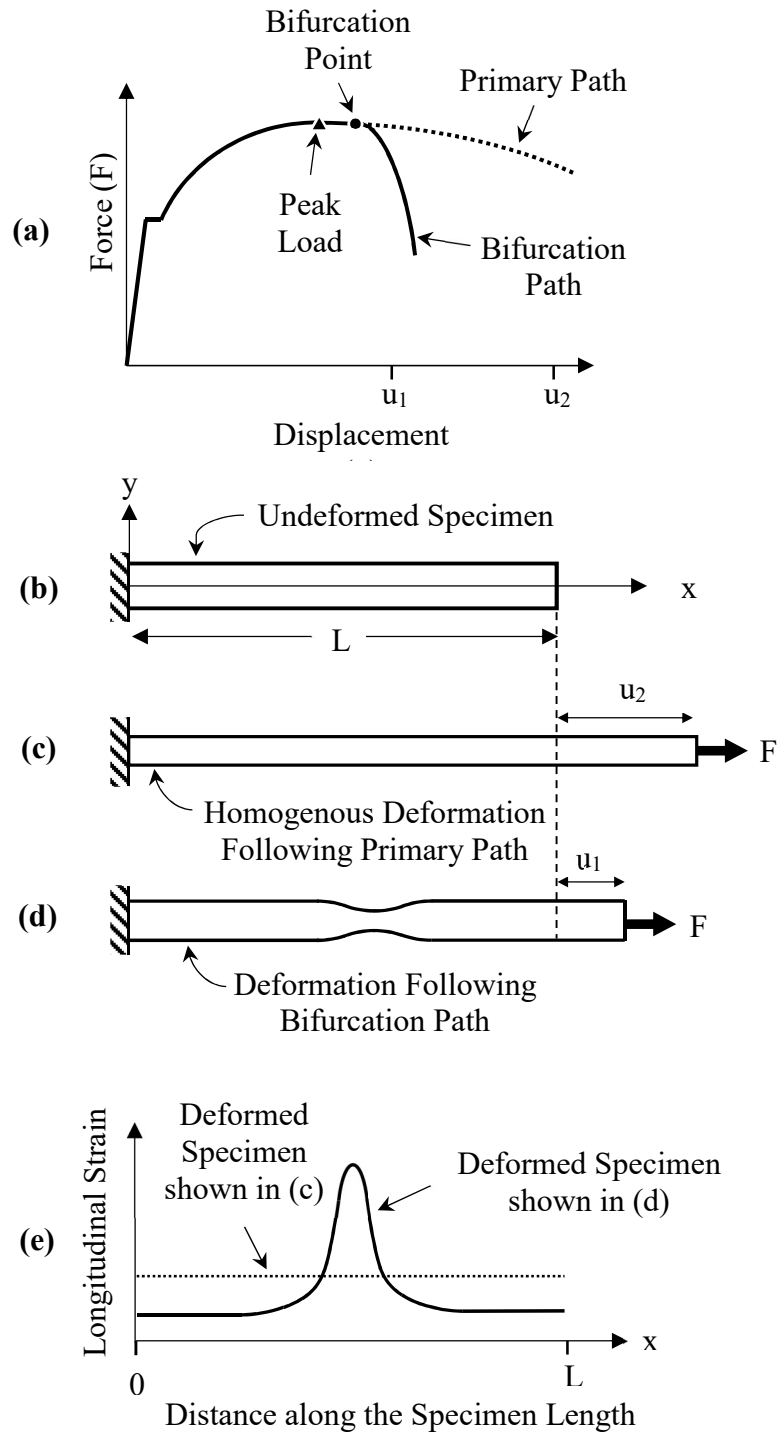


Fig. 2.2. (a) Force-displacement curve, (b) undeformed specimen, (c) deformed specimen following the primary path (d) deformed specimen following the bifurcation path, and (e) longitudinal strain profile of specimen following bifurcation or primary path.

2.1.3. Localization Length

The localization length is the length of a zone within the member length where the strain continues to increase beyond the peak load, while outside of the zone the strain decreases as the member unloads elastically (Bažant and Cedolin 2010; Dai et al. 2011; Jirásek 2004; Kolwankar et al. 2017; Li and Karr 2009; Schreyer and Chen 1986; Yalcinkaya and Lancioni 2014). Assuming the strain localization occurs at the peak load, Fig. 2.3a shows how the longitudinal strain keeps increasing inside the localization zone after the specimen reaches the peak load and decreasing outside the localization zone till the rupture load is reached. The strain localization occurs due to the release of strain energy from the unloading region outside the localization zone (Bažant and Cedolin 2010). The increase in global deformation in the post-peak region is almost entirely due to the deformation occurring within the localization zone. Thus, quantitative determination of localization length is the key to predict the behavior of post-peak response (Bažant and Cedolin 2010). For instance, Fig. 2.3b shows the engineering stress (σ_x) versus the engineering strain (ϵ_x) with respect to x-axis of three different specimen lengths ($L_3 > L_2 > L_1$) with the assumed same longitudinal strain behavior and localization length shown in Fig. 2.3a where σ_0 is the maximum engineering stress. The longest specimen has the steepest post-peak behavior due to the ratio of the deformation inside the localization zone to the specimen length.

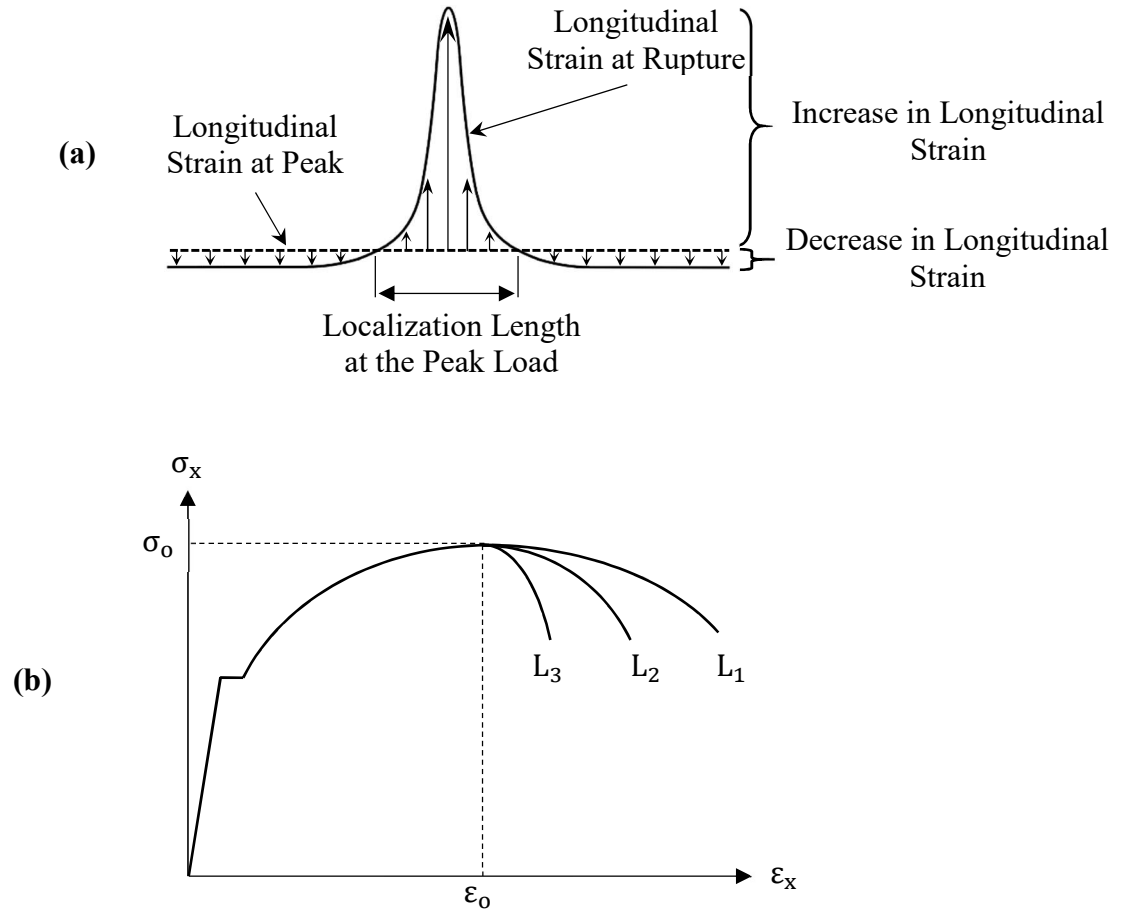


Fig. 2.3. (a) The behavior of longitudinal strain along x-axis after the peak load and (b) post-peak behaviors of three members of different lengths.

The amount of the localization length affects the post-peak behavior of beam column members. Sideris and Salehi (2016) showed that for the smaller localization length, softening initiated at smaller lateral displacements and the curvature distribution was more localized to the bottom end as shown in Fig. 2.4. This is because that the spreading of the inelastic response is controlled by the amount of the localizing length. Therefore, the smaller localization length, the more localized curvature distribution was due to spreading

the inelastic response over a smaller length, whereas, the opposite was true for larger amount of localization length.

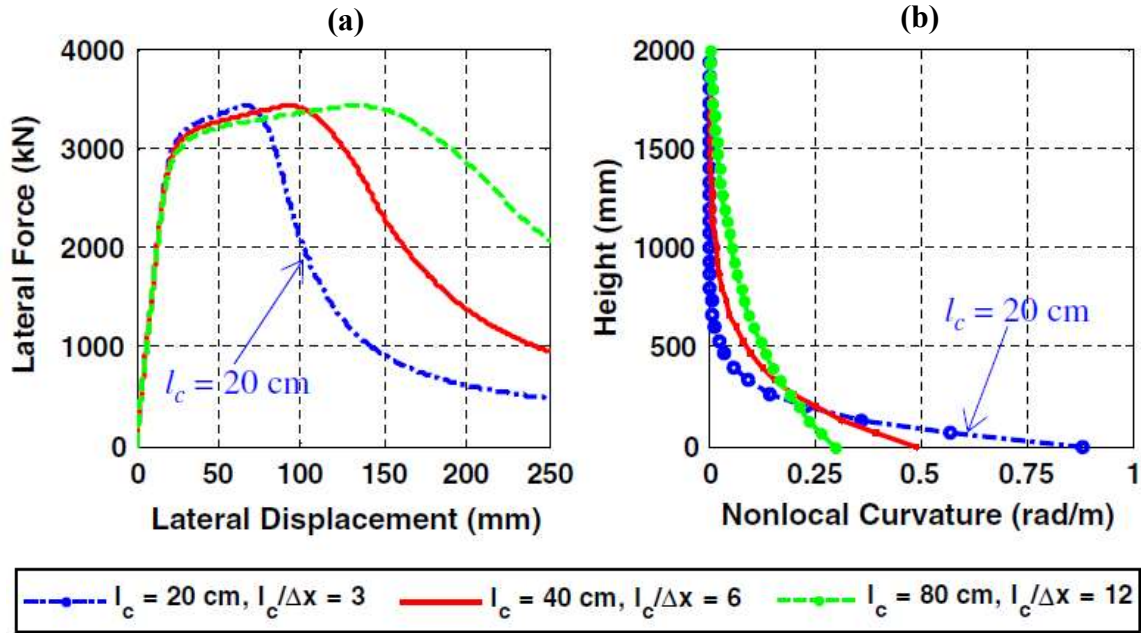


Fig. 2.4. Effect of L_c on (a) lateral force versus displacement; (b) curvature distribution for peak lateral displacement of 250 mm (Sideris and Salehi 2016)

The localization length in steel members evolves during the post-peak regime. Kotronis et. al (2008) showed that by using simplified ductile constitutive law to analytically study a one-dimensional member, the localization zone decreases through the softening process. Kolwankar et. al (2017) found that the localization length of a cylindrical steel bars under tension decreases with increasing deformations after the peak load. To monitor the evolution of the localization length, in Fig. 2.5a, the localization length of three points (point 1 is the peak load, point2 and point3) on the post-peak region are considered. As the load drops and deformations increase, the localization length decreases ($L_{c1} > L_{c2} >$

L_{c3}) as shown in Fig. 2.5b due to unloading the outer region of the previous localization zone. When strain localization occurs, the localization length is at its largest and decreases as the deformations increases till the rupture load is reached. Kolwankar et al. 2017 studied the evolution of localization length and found that the onset of strain localization occurred at the peak load when the localized necking initiated. They found that the localization length at the peak load is five time the diameter of the bar and it decreased gradually till rupture. Fig. 2.6 shows evolution of localized length determined by comparing the average engineering strain and the longitudinal engineering strain based on FEA simulations.

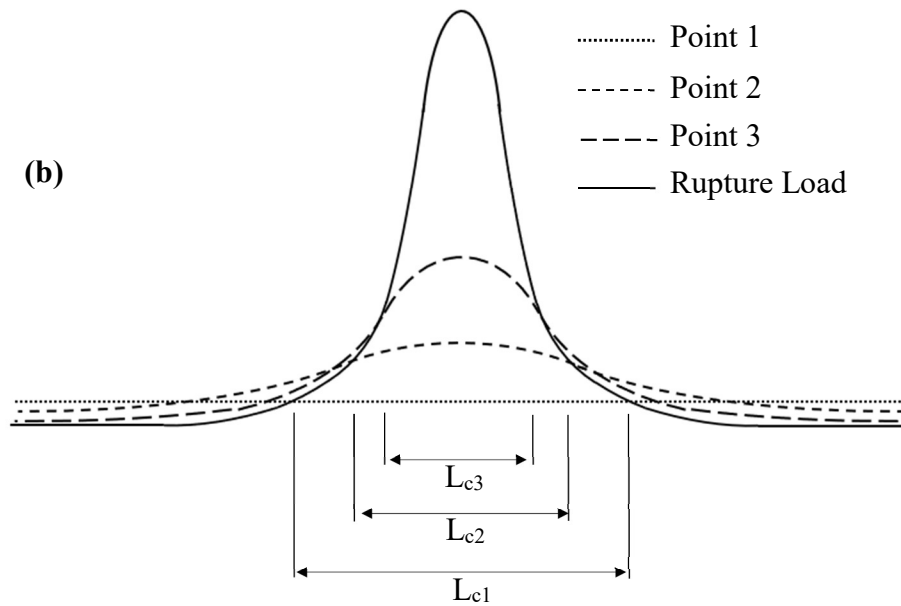
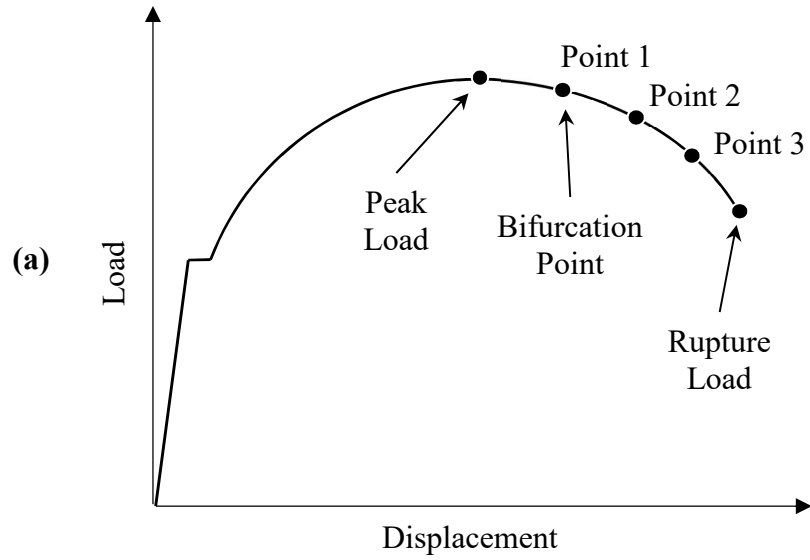


Fig. 2.5. (a) Four loading instants along the post-peak region and (b) longitudinal strain at the four loading instants

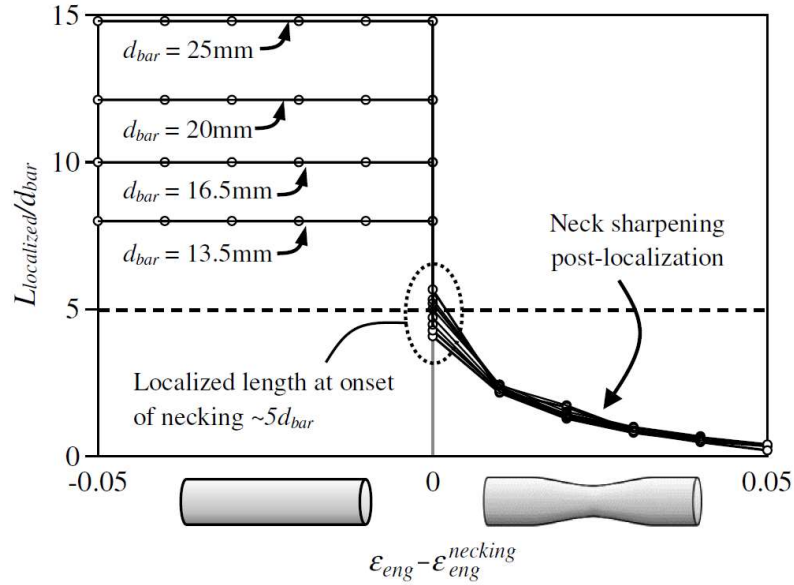


Fig. 2.6. Evolution of localized length for simulations with different diameters and hardening (Kolwankar et al. 2017)

2.1.4. Size Effect

The post-peak response is highly size dependent. The longer the member, the steeper the post-peak curve (Bažant 2003b, 2003a; Jansen and Shah 1997; Needleman 2016). Members with a longer length become more brittle, and exhibit steeper post-peak curves (if member is long enough, a snap back may happen) while shorter ones become ductile and have more shallow post-peak curves (Chen et al. 2008; Dai et al. 2011; Schreyer and Chen 1986). After the strain localization occurs, the global deformation is due primarily to the deformation produced within the localization zone. For a constant localization length, hence, the total displacement of a bar under tension after strain localization occurs is insensitive to the specimen length so that the engineering strain (the total displacement divided by the specimen length) decreases with the increase in the specimen length. Dai et al. (2011) used general nonlinear constitutive relations to

analytically investigate the nonlinearity and the size effect of the post-peak structural response of strain-softening with localization by using a one-dimension model problem. They found that for a fixed localization length, the post-peak becomes steeper and for sufficiently longer member, the member experienced snapback or snap through as shown in Fig. 2.7.

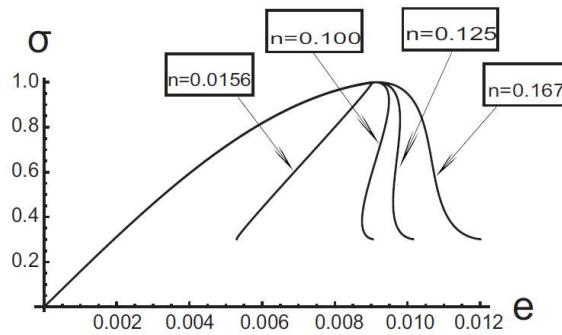


Fig. 2.7. The engineering stress-strain curves for different n ($n=L_c/L$) (Dai et al. 2011)

2.2. Numerical Models

The post-peak behavior of steel under tension has been the subject of many previous studies. However, the majority of the studies are only analytical and do not focus on the evolution of the localization length during the post-peak response. Cabot et. al (1988) compared various strain softening models, and showed the importance of the localization length (L_c) when simulating the post-peak response. Kotronis et. al (2008) used a simplified constitutive equation to numerically study a one-dimensional layer and showed that the width of the localization zone remained constant for quasi-brittle materials and decreased for ductile ones during the softening process. Jirásek and Rolshoven (2009a) compared and

evaluated one-dimensional strain softening plasticity models. They considered that the onset of localization is a bifurcation from a uniformly deformed state. They numerically studied the evolution of the localization zone of finite thickness and the corresponding strain profile. In the second part of their paper, Jirásek and Rolshoven (2009b) also compared and evaluated a number of plasticity models with the gradients of internal state variables, and found that some models were applicable at the initial stages of the softening process but were compromised by the expansion of the localization zone, while the other models suffered from significant mathematical defects. Rolshoven and Jirasek (2002) compared and analyzed one-dimensional softening plasticity models regularized by nonlocal averaging, and found that the evolution of the plastic strain profile depends on the softening law.

2.3. Local models

The simulated post-peak response by softening constitutive models is nonobjective (see Fig. 2.8). The simulated post-peak response becomes highly sensitive to discretization which is the mesh size or number of Gauss points. After the peak load, strain softening causes the strain localizes into one element and the length of that element acts as the localization length (Bazant et al., 1984). Therefore, as the mesh becomes smaller, the descending part of load displacement curve becomes steeper because the deformations in the post-peak is only provided by the localized element.

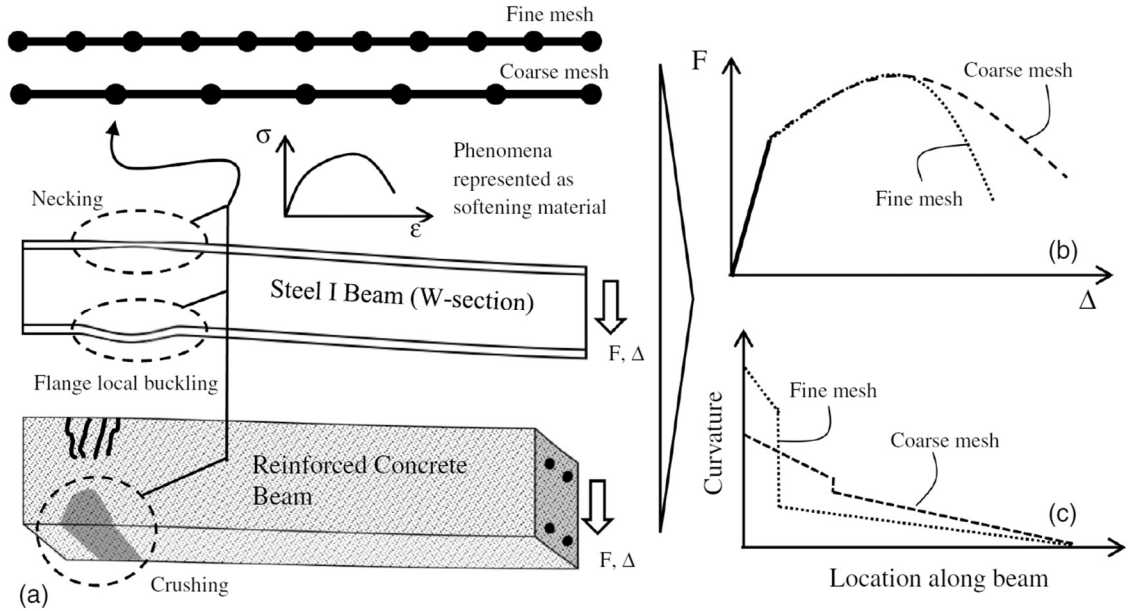


Fig. 2.8. Fiber-based simulation of localization processes through softening constitutive models (Kolwankar et al. 2017)

2.4. Nonlocal Models

Nonlocal models have been developed to overcome the non-objectivity produced by local models. The nonlocal damage model averages the variables responsible for damage over a certain zone (Pijaudier-Cabot & Bazant, 1988). In most cases, nonlocal models average the strain, and are capable of eliminating the mesh dependence. Jirásek and Rolshoven, (2003) and Rolshoven and Jirasek, (2002) analyzed and compared some of softening plasticity models which were regularized by nonlocal averaging.

The nonlocal model implemented through a one-dimensional line-element-based model has a uniaxial stress-strain relationship with softening determined from the FEA, a length scale, and a volume-averaged nonlocal strain measure. The mesh dependence shown by the local models was successfully mitigated the nonlocal model.

2.5. Recent Nonlocal models

Nonlocal models have been developed to overcome the non-objectivity produced by local models. This section presents some of the nonlocal models that were developed.

Sideris and Salehi (2016) proposed a gradient inelastic beam theory and flexibility-based frame element formulation to overcome strain localization and loss of objectivity. The proposed model was derived by enriching Navier's beam theory with nonlocal deformation variables. The model did not impose any restrictions on stress-strain constitutive laws. The proposed model reduced strain localization and loss of objectivity. However, solution uniqueness was not achieved.

Salehi and Sideris (2017) developed a gradient inelastic flexibility-based frame element formulation to capture member responses to non-monotonic loading conditions. The model eliminated discontinuities in strains profile introduced during the localization condition and enhanced convergence with mesh refinements. The fourth order of the model demonstrated faster mesh convergence than the second order model. The localization length used in the two presented examples was assumed to be 40 cm.

Kolwankar et al. (2017) presented a nonlocal model that mitigates mesh dependence in fiber models for steel members. Tension necking and compression buckling are two common modes of localization in cylindrical steel bars that were addressed. To develop, calibrate, and validate the nonlocal model, they conducted finite element analysis (FEA) simulations. The FEA simulations examined length/diameter ratio and strain-hardening parameter. By fixing the length ($L=200$ mm), four different values of the diameter (13.5, 16.5, 20, and 25 mm) were produced. Von Mises material with isotropic hardening represented the material constitutive response that was used in the FEA

simulations. While the power-law relationship (following equation proposed by Kumar et al. 1981) represented the hardening.

$$\begin{aligned}\sigma &= E\varepsilon && \text{for } \sigma \leq \sigma_Y; \\ \sigma &= \left[\sigma_Y - K \left(\frac{\sigma_Y}{E} \right)^n \right] + K\varepsilon^n && \text{for } \sigma > \sigma_Y\end{aligned}\quad (2.1)$$

Where σ , ε and σ_Y are the true stress, the true strain and the yield stress, respectively. K and n are material constants. The mesh size that was used in the FEA simulations was approximately 0.4 mm. For both necking and buckling, a trilinear constitutive relationship was used to characterize uniaxial material response. The first ascending branch of trilinear constitutive relationship is elastic response while the second ascending branch is the strain hardening. The third branch described softening. To mitigate mesh sensitivity, a length scale was introduced. The nonlocal strain was determined by the following equation.

$$\varepsilon_p^* = m \cdot \varepsilon_p^w + (1 - m) \cdot \varepsilon_p \quad (2.2)$$

Where ε_p^* , ε_p^w and ε_p are the nonlocal strain, weighted average of strain and plastic strain, respectively. While m is a factor between 0 and 1. Weighted average of strain can be determined by the following equation.

$$\varepsilon_p^w(x) = \int_{L_c} \alpha(x, \xi) \cdot \varepsilon_p(x, \xi) \cdot d\xi \quad (2.3)$$

$$\alpha(x, \xi) = \frac{\alpha'(x, \xi)}{\int_{L_c} \alpha'(x, \xi) \cdot d\xi} \quad (2.4)$$

$$\alpha'(x, \xi) = \begin{cases} \frac{15}{8 \cdot L_c} \left[1 - \frac{4 \cdot (x - \xi)^2}{L_c^2} \right] & \text{for } |x - \xi| \leq \frac{L_c}{2} \\ 0 & \text{for } |x - \xi| > \frac{L_c}{2} \end{cases} \quad (2.5)$$

Where $\alpha(x, \xi)$ is the weight function defined over the localization length, and ξ is a local variable. The nonlocal model results shown Fig. 2.9 did not exhibit non-objectivity (the post-peak behavior was not influenced by the mesh sizes) and followed the response of the

FEA solution. While Fig. 2.10 shows the ability of nonlocal model of mitigating mesh dependence produced by the local model.

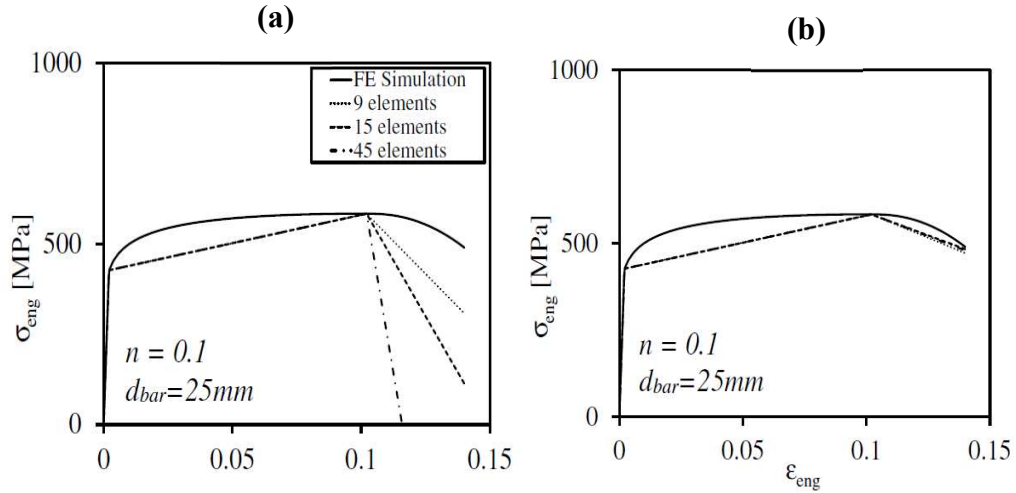


Fig. 2.9. Engineering stress-strain response for cylindrical steel bar under tension from FEA and line model for (a) local formulation and (b) nonlocal formulation

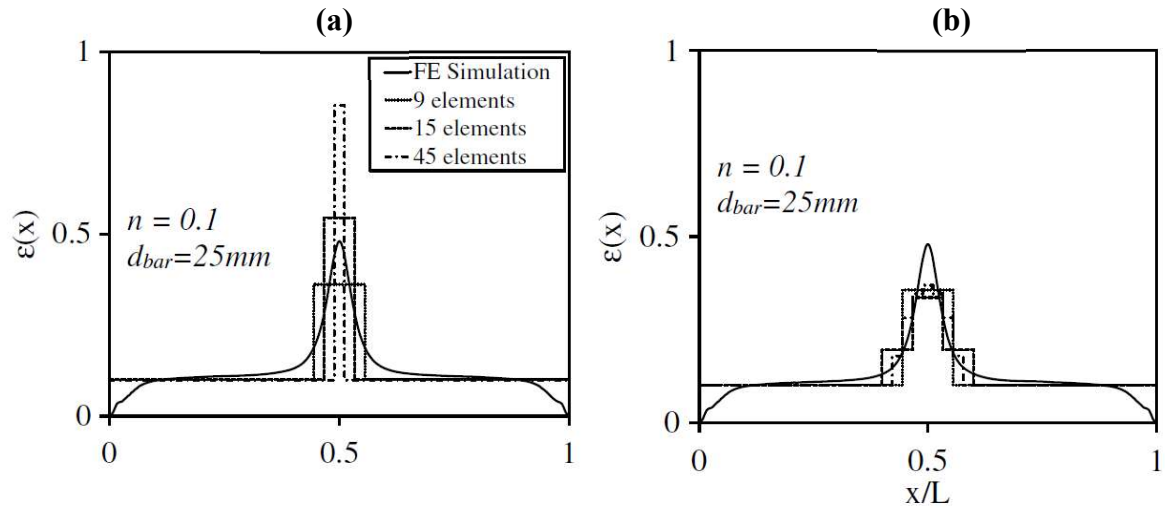


Fig. 2.10. Longitudinal strain distribution for cylindrical steel bar under tension from FEA and line model for (a) local formulation and (b) nonlocal formulation (Kolwankar et al. 2017)

Kolwankar et al. (2018) developed a two-dimensional nonlocal fiber-based beam-column model. The model combined length scale (associated with localization phenomena which was determined based on FEA simulations) associated with local buckling and softening constitutive relationship at the fiber level as shown in Fig. 2.11. The length scale associated with local buckling and constitutive response at the fiber level were estimated. They focused on hot-rolled wide flange sections. The W-sections member when subjected to axial compression and flexure shows local buckling-induced softening. The mesh dependence was overcome. However, the approach addressed one form of localization and softening due to local buckling. It assumed that the plane sections remain plane.

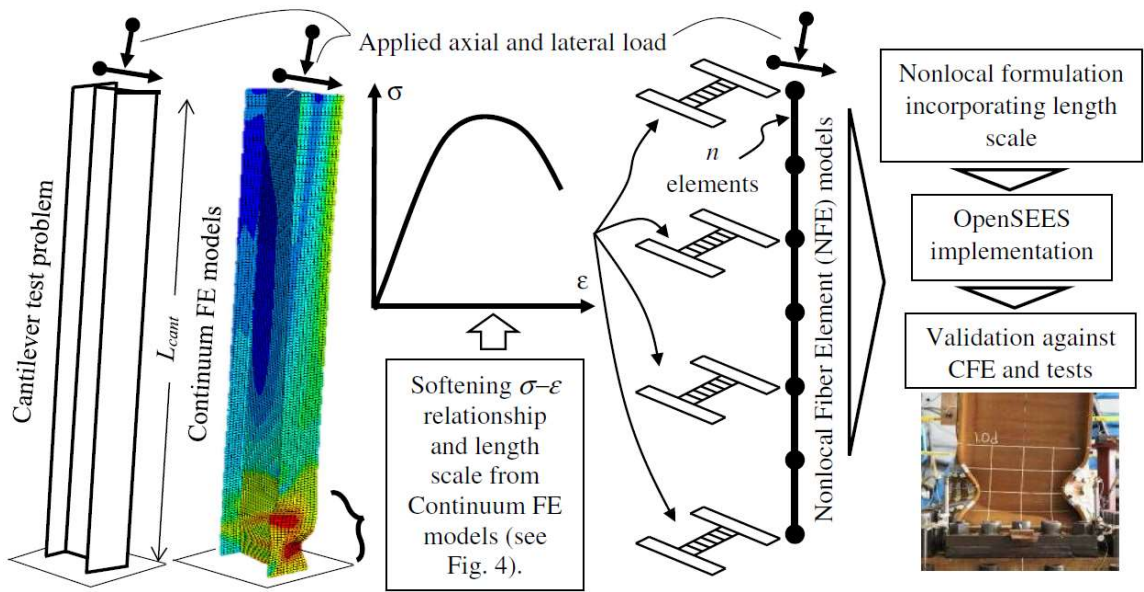


Fig. 2.11. Schematic illustration of research methodology and components (Kolwankar et al. 2018)

2.6. Summary

The following is a summary of the major points from previous research:

- Modelling structures is still challenging since there are many factors that control the post-peak response of the structure. Hinge models failed in simulating the post-peak of a structure because they to be calibrated and not able to spread plasticity. Fiber models failed when the member experienced softening.
- It was shown that the post-peak response of a structure depends on the localization length. Furthermore, the localization length was determined based on numerical models instead experimental data and most of the nonlocal models are validated by other numerical models. Thus, there is a lack of experimental data to validate the numerical solutions which determine the localization length. Hence, a systematic experimental study is needed to investigate the evolution of the localization zone and its influence on the post-peak response of one-dimensional steel members.
- The nonlocal line-element-based models need a constitutive relationship in order to simulate the post-peak response of a structural member. While the nonlocal fiber-based beam-column model depends on estimated constitutive relationship in simulation of the post-peak response of a beam column. The gradient inelastic beam theory also needs an accurate constitutive relationship to simulate the structural response. Thus, there is a need for a generic constitutive relationship that is not restricted by structural size. An alternative method is needed which consists of a one-dimensional single line element that includes the effect of localization.

CHAPTER THREE

CHAPTER 3: EXPERIMENTAL PROCEDURE AND RESULTS

3.1. Introduction

The post-peak response of steel members often shows strain softening, i.e. decrease of stress with increasing strain in a zone of finite size. The size of the localization zone and the deformations occurring inside it are key for objectively predicting the post-peak behavior of steel members. An assumed strain softening segment length in a structural member is needed to determine the softening curve (Bažant 1976). In most publications, the length of the localization zone is either be assumed (Sideris and Salehi 2016) or calculated based on numerical results (Kolwankar et al. 2017). However, there is a lack of experimental data to validate the numerical solutions which determine the localization length. Hence, a systematic experimental study is performed to investigate the evolution of the localization zone and its influence on the post-peak response of one-dimensional steel members.

Experiments were performed to characterize the post-peak behavior of one-dimensional steel members. The testing looked specifically at determining the localization length (L_c) and its evolution throughout the loading history as well as the deformations occurring inside the localization zone. These properties are crucial in analytical determination of the post-peak behavior. Longitudinal engineering strain (ϵ_{xx}) along the specimen length throughout the loading history was measured to determine the localization length and its evolution. Three-dimensional Digital Image Correlation (3D DIC) measurement system was used to capture the deformations along the specimen length in

order to calculate the longitudinal engineering strain, transverse engineering strain (ϵ_{yy}) and longitudinal true strain ($\epsilon_{yy}^{\text{true}}$). By calculating $\epsilon_{yy}^{\text{true}}$ at the point where the fracture occurs, a Finite Element Analysis (FEA) model becomes easy to be developed. The strain rate at two points, inside and outside the localization zone, are studied.

3.2. 3D DIC Setup

The 3D DIC measurement system by Dantec Dynamics consists of two cameras held by tripod stand, data acquisition and a laptop which has Istra 4d 4.4.6 v2 software that controls the two cameras settings and performs the 3D DIC correlation algorithm. To ensure a correct and accurate 3D DIC outcome, a few steps must be done as follows:

1) Specimen surface preparation:

This is the most crucial step of performing the DIC. Before performing the DIC correlation imaging, the surface of the region of interest on which strains want to be measured must have a random speckle pattern which is small random shapes of black color located randomly on a white surface. This can be done by spraying a thin layer of a white color after making sure that the surface is clear. Then after it dries, a black color can be sprayed 1-2 ft away from the specimen surface to create the random speckle pattern. Fig. 3.1 shows an example of the random speckle that was created for all tested specimens. It is recommended that matte white and black spray paints are used to reduce the reflection of light over the specimen surface. After applying a speckle pattern to the specimen, the specimen is ready to be tested.

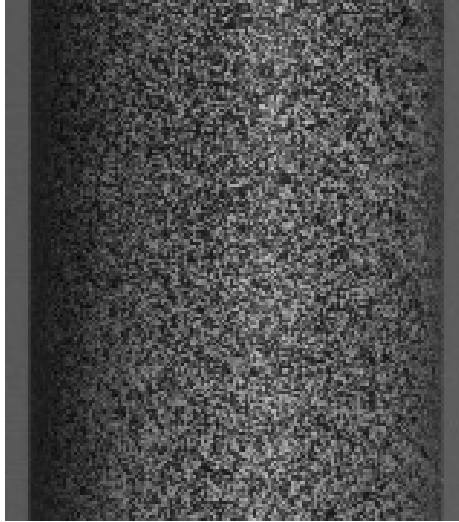


Fig. 3.1. Random Speckle pattern

2) Camera settings:

One of the most important setting is the sharpness or the focus. To avoid inaccurate results the whole region of interest must be sharp and has almost no blur region even after the final deformation. The overall sharpness is determined by how much of the image is in focus. The sharpness can be adjusted by changing the focal length of the camera or moving the camera toward or away from the specimen or both. The amount of overall sharpness can be calculated by Istra 4d 4.4.6 v2 software (higher number represents higher sharpness).

The other parameter is depth of field or depth of focus which determines how deep the sharpness will be. The depth of field is controlled by the aperture setting which controls the size of the lens opening that allows light into the camera. The importance of depth of field arises if the interesting area is large or not perpendicular to the camera axis or some of the deformations occur out-

of-plane (such as buckling). The depth of field can be increased by increasing the aperture and vice versa. But with higher aperture, less light is allowed into the cameras causing noises and reducing the image quality which may affect the DIC correlation results. This can be overcome by either increasing the density light of the lighting source or increasing the period of exposure time (shutter speed) which is the length of time when the sensor inside the camera is exposed to light or both. The exposure time can be adjusted by Istra 4d 4.4.6 v2 software. To make sure that the cameras are taking pictures in a consistent rate, the shutter speed should be less than the frame rate speed.

3) Pre-Processing of 3D DIC software:

a) Imaging parameters

Higher frame rate (the number of frames per a second) may ensure capturing smooth deformation which can help in correlation process. Istra 4d 4.4.6 v2 software provides two grey values, 8-bit grey value images and 16-bit grey value images with 12 significant bits or 16 significant bits but as the grey value increases, the size of images and the time of correlation increase as well. Grey value increases the contrast of speckle patterns which leads to better correlation results (Pan et al. 2008).

b) Calibration

In order to get an accurate correlation result, the images must be calibrated every time a new 3D DIC setup is used. The calibration can

be done by placing a calibration card at approximately the same distance between the region of interest and the cameras. Fig. 3.2 shows the calibration card that was used in the experiments for the calibration. Two sets of images should be taken. Every set has five images in various positions. The first position is where the calibration card is placed perpendicular to central axis the two cameras where the horizontal and the vertical axes are x- and y-axes, respectively. The other four position is where the calibration card is tilted to the right, left, up and down, the sequence of these four positions does not matter. In the second set, calibration card must be rotated 90° to the right, then the same five positions placed earlier can be taken. After saving the calibration parameters and making sure neither the cameras nor the specimen is moved, the experiment can be run.



Fig. 3.2. Calibration card

c) Region of interest (ROI):

It is a region within the specimen surface where the deformations and strains at the surface are measured. It may be difficult to fit the whole ROI to the image frame sides. Besides, it is much faster to process only the ROI instead of the whole image. Istra 4d 4.4.6 v2 software has a tool that can be used to choose the outline of the ORI as shown in Fig. 3.3. The ROI will be divided into subsets before correlation processing starts which is discussed in next point.

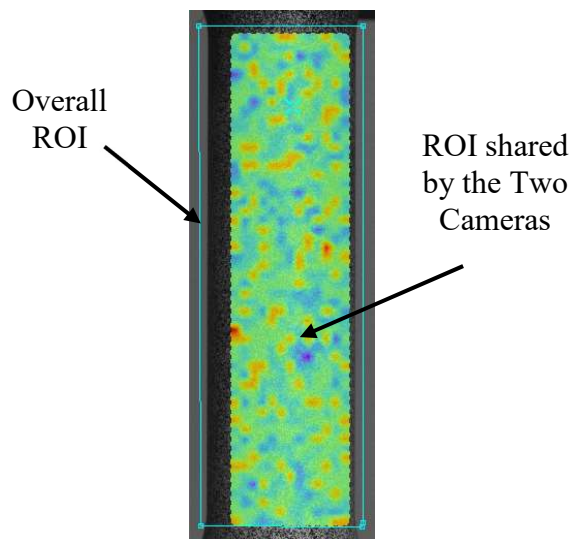


Fig. 3.3. Region of Interest

d) Facet size (subset size) and grid spacing:

The facet (a technical term, subset is the term used by researchers) is a square subregion whose size is in pixels and contains a unique pattern of black a white while grid spacing is the distance between facets centers in pixels. It is recommended that the ratio of facet size to grid spacing

is $4/3$ (Dantec Dynamics 2017). Each grid point represents one single data point (see Fig. 3.4). In order to have independent data points, the facets of neighboring data points should not overlap. It is shown that overlap of $1/3$ of a facet does not influence the spatial resolution. So, the lower grid spacing as well as smaller facet size are, the higher spatial resolution (Dantec Dynamics, 2017). However, when smaller facet size is used, it becomes harder to correlate as well as the uncertainty of displacement, the displacement that cannot be captured by 3D DIC, increases. Thus, increasing facet size leads to smoothing of the results and drops the spatial resolution.

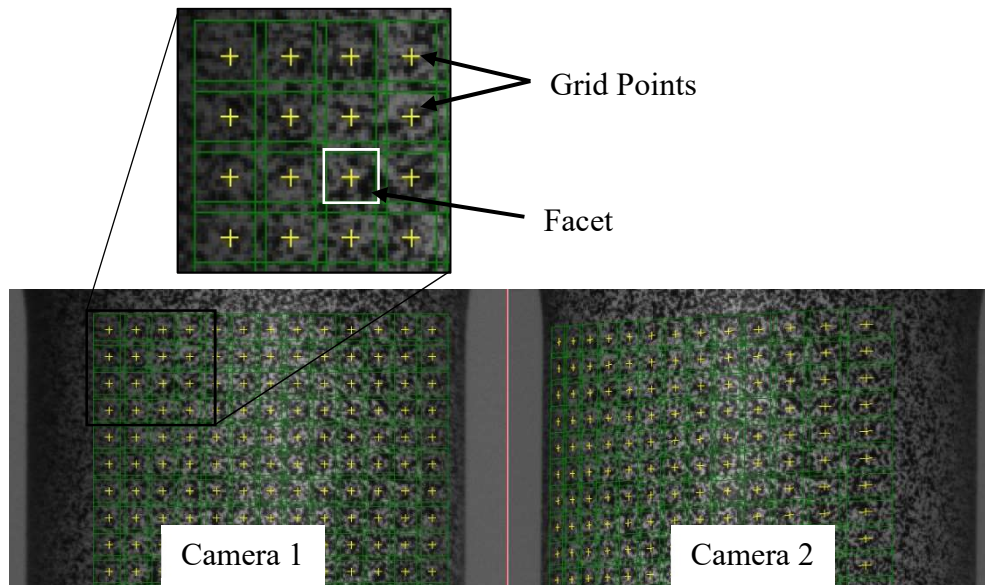


Fig. 3.4. Facets and grid points

4) Post-Processing of 3D DIC software:

Once the correlation processing completes, the displacements in x, y and z direction, and true and Lagrange engineering strains in x or y direction can be determined at a point, or along a line at any loading instant or at the whole loading history. This is useful to plot the strains or calculate the deformations along a strain gage. The 3D DIC data can be smoothed. Istra 4d 4.4.6 v2 software provides two smoothing techniques, local regression and Spline techniques. Local regression technique is used in this work.

In the experiments, the aperture was set to $f/4$ to ensure all of the interesting area is sharp and sufficient light allowed into the two cameras without compromising the image quality due to the noises. The focal length was set to 35 mm and the two cameras were approximately placed at an angle of 30° . 16-bit grey value with 12 significant bits was chosen. The frame rate speed was set to 100 milliseconds (ms) while the exposure time was set to around 50-70 ms. 21 by 21 pixels and 17 pixels were used for facet size and grid spacing respectively. Smoothing technique such as local regression, was used to obtain smoothed results. A local regression filter with a kernel size of 7×7 was used for all tested specimens.

After the two images from each camera were calibrated, the loading machine and image capturing were run as simultaneously as possible. Image capturing was stopped once specimen broke.

3.3. Specimens

Cylindrical low carbon steel (A36) specimens were manufactured according to ASTM E8 (2013) (Fig. 3.5). All specimens were manufactured so that the ends of the reduced parallel section were not more than 1 % larger in diameter than the center of the specimen (i.e. not more than 0.005 in.), as detailed in ASTM E8 (2013). Specimens were 0.5 in. in diameter (D) with various section lengths (L) ($3D = 1.5$ in., $6D = 3$ in., $12D = 6$ in., $24D = 12$ in.). Three specimens with L equal to $3D$ and $6D$, respectively, and two specimens with L equal to $12D$ and $24D$, respectively, were tested. Table 3.1 shows the specimen information and key experimental results. All tested specimens were painted with matte white color base, and then a matte black color was sprayed to create a random speckle pattern for increasing the DIC accuracy.

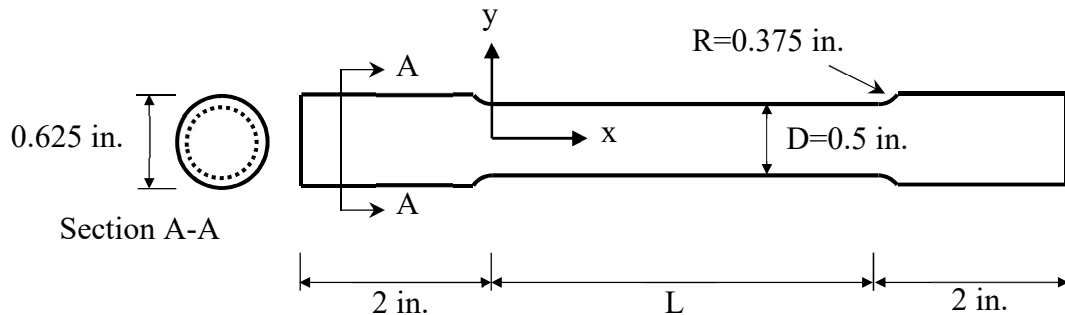


Fig. 3.5. Dimensions of steel specimen.

3.4. Test Setup

A universal MTS machine was used to perform monotonic displacement-controlled tension tests. Fig. 3.6 shows the general setup of the system. The rate of loading met the requirements specified in ASTM A370-17 (2017) (0.0125 strain per minute before yield

and 0.1 strain per minute after yield). A 3D DIC system, shown in Fig. 3.6, was used to capture the deformations along the specimen length. The accuracy of the 3D DIC system was verified with an extensometer placed on a 3 in. specimen (Fig. 3.7a). Fig. 3.7b shows the average engineering strain along the strain gage determined by 3D DIC and extensometer up to the rupture load. The accuracy of the 3D DIC system decreases when measuring higher values of strain. The 3D DIC system can accurately measure strain to 0.000074 strain in the elastic zone, while the spatial resolution in the plastic zone (equivalent plastic strain of 1.35 strain) is approximately 0.0008 strain due to the high amount of stretch that causes deformation in the speckle pattern. The stress versus strain data were obtained by synchronizing the loads from MTS machine with images captured by the 3D DIC data acquisition system. Fig. 3.8 shows all the tested specimens after rupture where the upper ends were attached to the MTS upper fixed part and the lower ends were attached to the MTS lower moving part. Fig. 3.9 shows the unsmoothed 3D DIC results for a 1.5 in. specimen just before rupture.

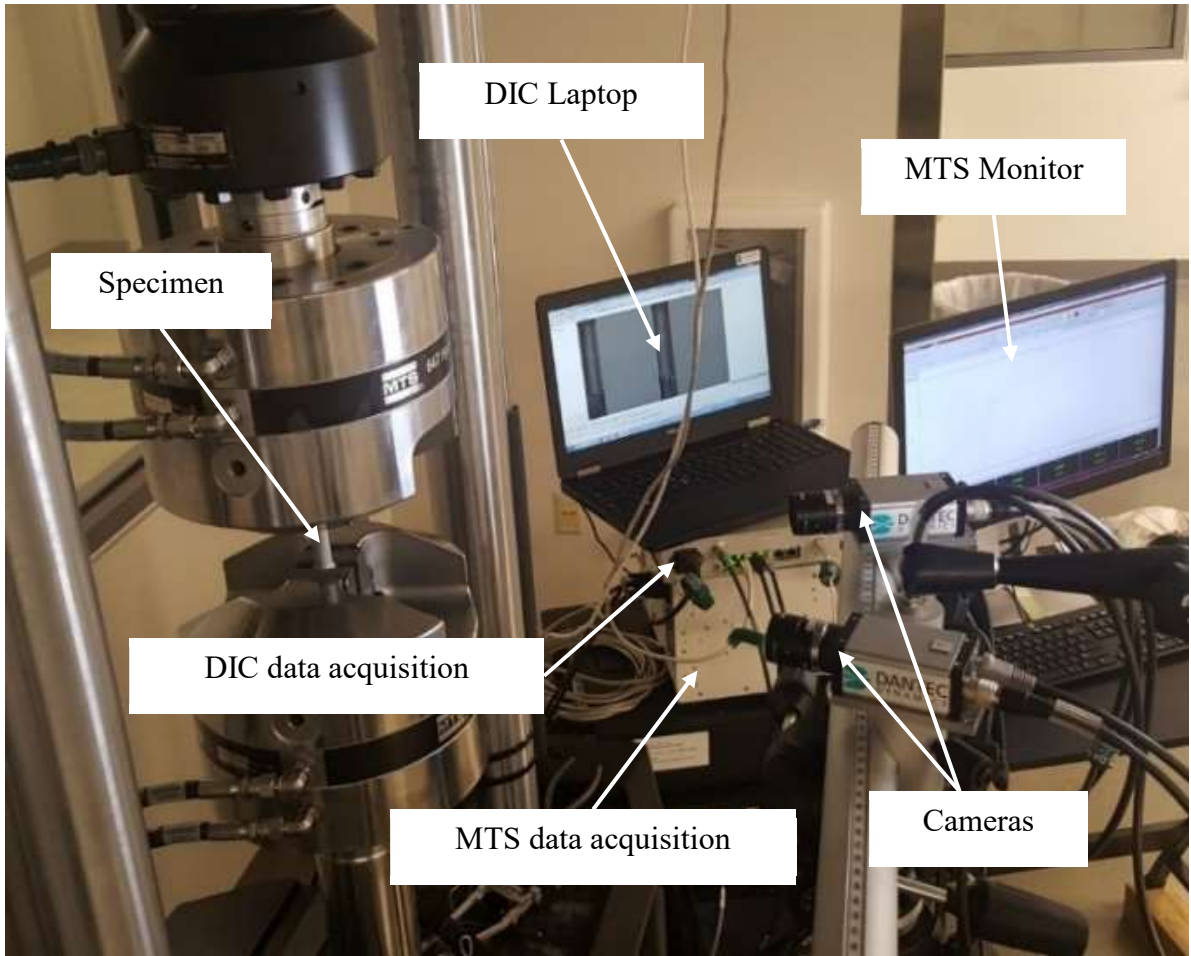


Fig. 3.6. Experimental Setup

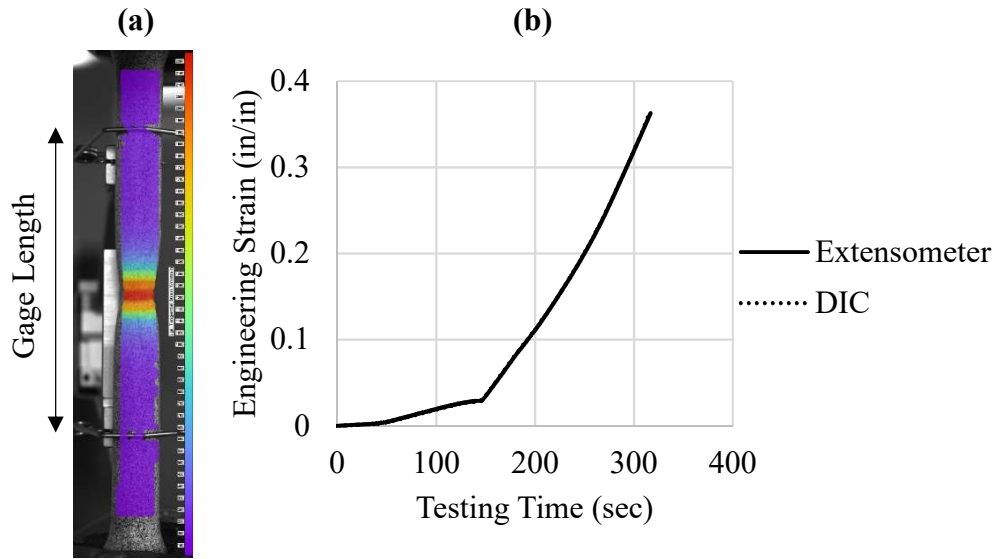


Fig. 3.7. (a) Extensometer placed on 3 in. steel specimen, and (b) 3D DIC versus extensometer

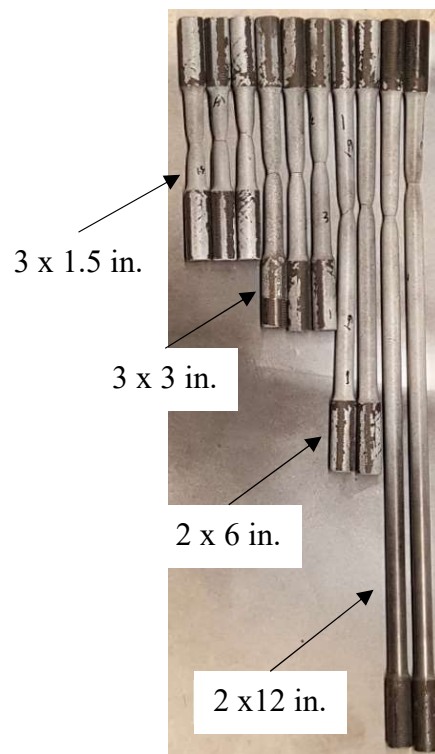


Fig. 3.8. All tested specimens after rupture

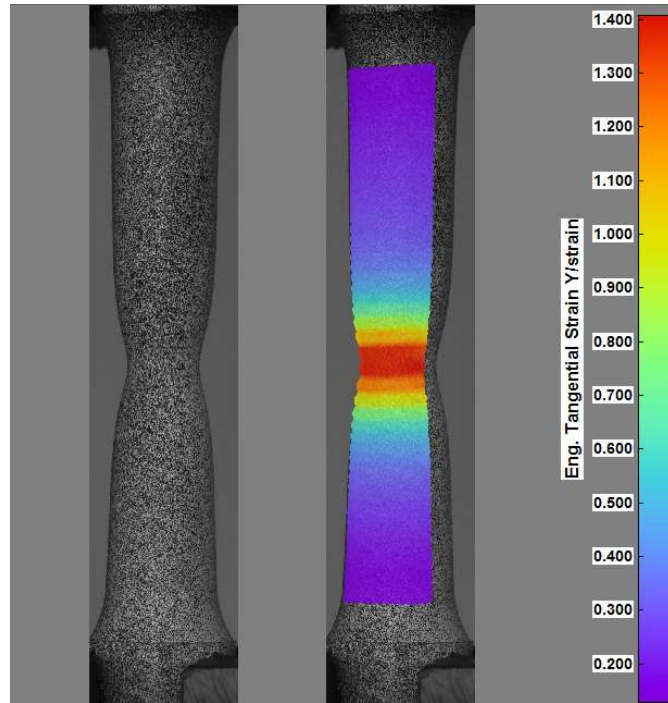


Fig. 3.9. Sample result just before rupture

Table 3.1. Test Matrix

Specimen I.D.	Length (in)	Peak Load (lb)	Rupture Load (lb)	ϵ_x at Peak (in/in)	ϵ_x at Rupture (in/in)
3D-1	1.5	14062.0	9933.4	0.1884	0.3961
3D-2	1.5	14063.7	9953.5	0.1888	0.3975
3D-3	1.5	14025.1	9715.7	0.1822	0.3998
6D-1	3	13998.5	9916.9	0.1899	0.3182
6D-2	3	13889.8	9757.8	0.1851	0.3243
6D-3	3	13936.9	9803.7	0.1902	0.3232
12D-1	6	13885.9	9630.6	0.1753	0.2796
12D-2	6	13745.7	9448.8	0.1761	0.2843
24D-1	12	13680.6	9330.4	0.1706	0.2208
24D-2	12	13937.7	9606.5	0.1729	0.2222

3.5. Experimental Results

The average of engineering stress versus engineering strain curves of specimens with the same length are plotted in Fig. 3.10. The engineering strain is the average of longitudinal engineering strain along the specimen length or the total displacement divided by the specimen length. Fig. 3.11 shows the engineering stress versus engineering strain curves of all tested specimens. The specimens with the same length have almost the same engineering stress-strain relation up to rupture because all specimens were manufactured in a way so that the variation in diameter along the specimen is less than 1% as recommended by ASTM A370-17 (2017). All tested specimens had nearly the same behavior up to peak load. The peak load of the shorter specimens was slightly higher due to reduced imperfections. The fracture occurred at or close to the middle of the length for all tested specimens except for those whose lengths are 12 in. where the fracture occurred close to the upper quarter of the specimen length. The experimental results (Fig. 3.10) showed that the post-peak behavior is influenced by length scale as expected. Longer specimens show a sharp, almost brittle, failure due to the concentration of strain within the localization zone as described in the background.

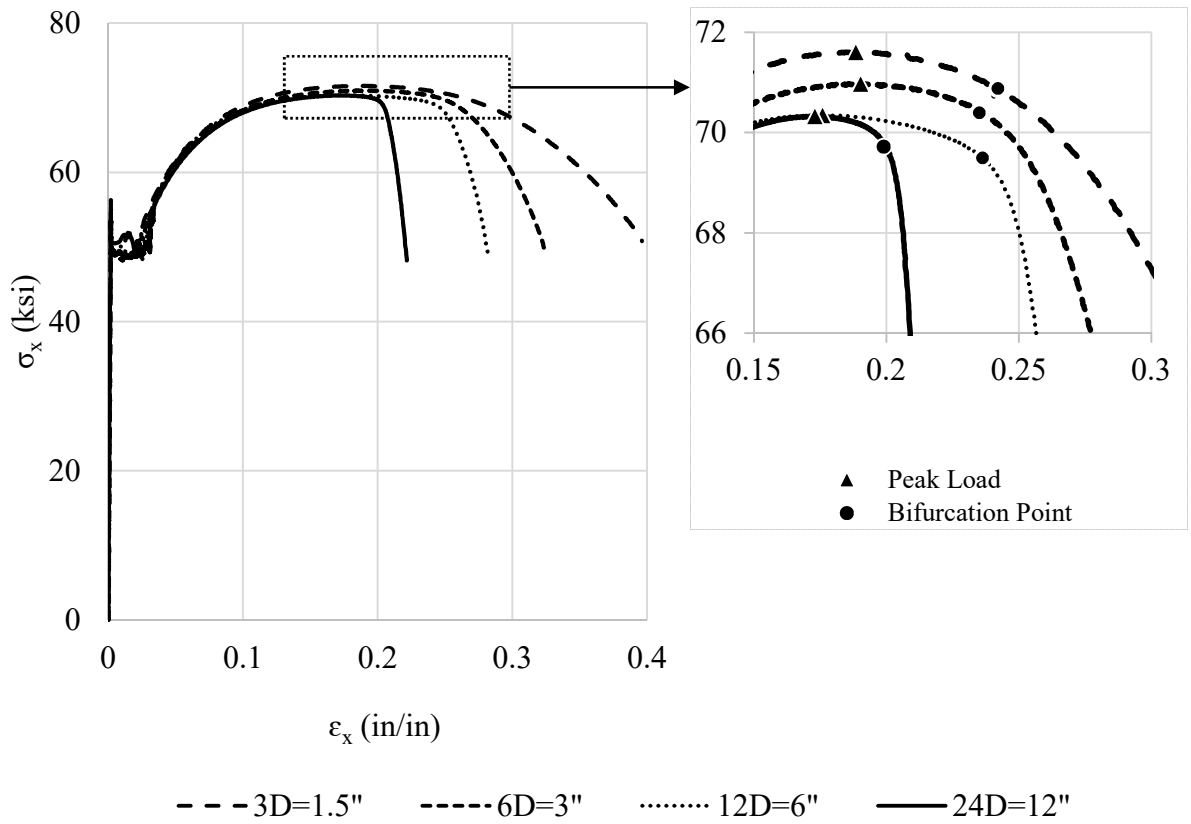


Fig. 3.10. Average of engineering stress vs. strain for specimens with the same length

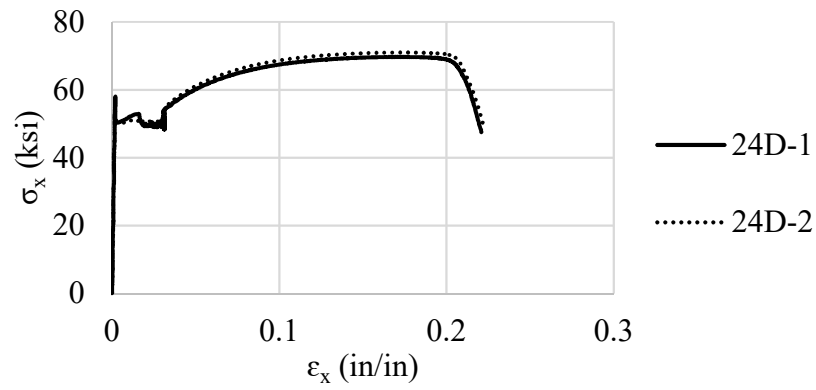
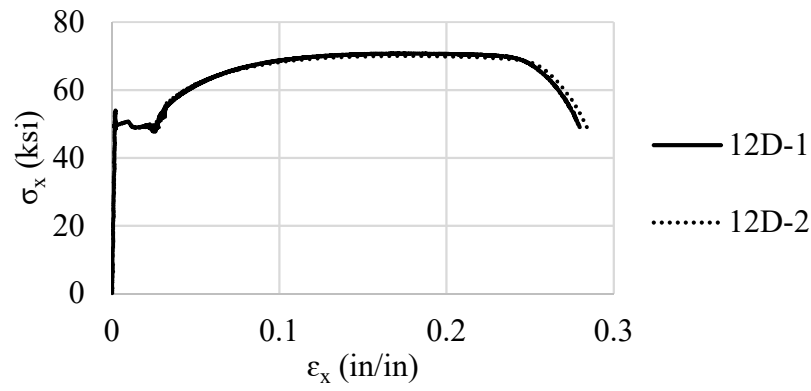
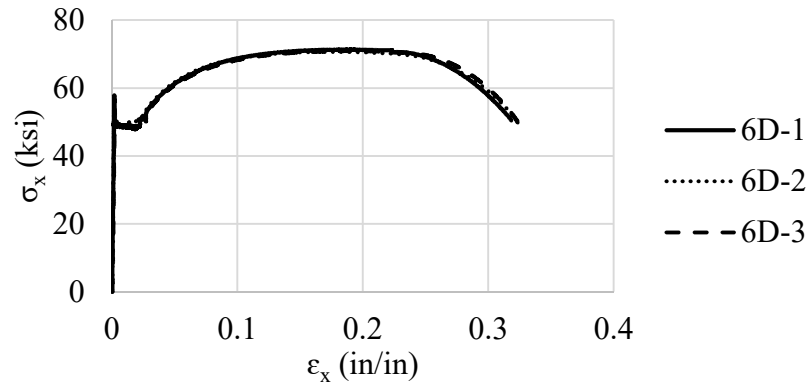
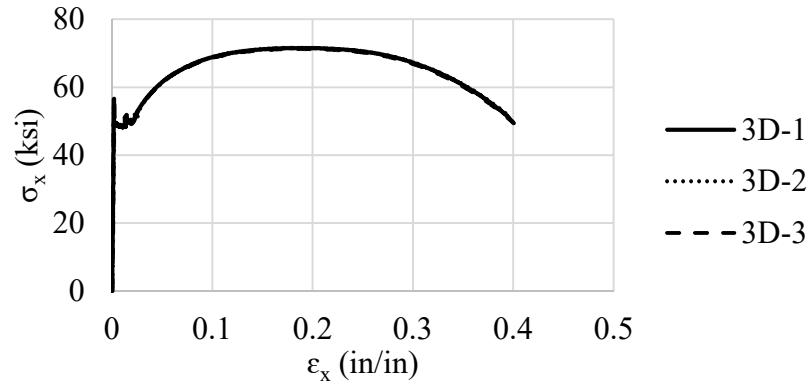


Fig. 3.11. Engineering stress vs. strain for all tested specimens

3.5.1. Engineering Strain Profile

The examination of the longitudinal engineering strain profile is crucial in determining the localization length and post-peak behavior. Longitudinal engineering strains and transverse engineering strains (ϵ_{yy}) for specimens 3D-1, 6D-3, 12D-1 and 24D-2 along the specimen length are plotted at the rupture load in Fig. 3.12 and Fig. 3.13, respectively. The longitudinal and transverse engineering strains are centered on the location of the strain localization (normalized distance = 0). The peak strain is nearly identical in all tests. Furthermore, longitudinal and transverse engineering strains within approximately 0.5 in., (same as the diameter of the specimen), of the center of localization zone are almost identical. This illustrates that the localized necking zone which leads to fracture is closely related to the specimen diameter. However, as the length of the specimen decreases so does the longitudinal engineering strains away from the center of the localization zone. The 3D and 6D specimens show more localized behavior with smaller longitudinal and transverse engineering strains away from the center of the localization zone. Whereas the behavior of the 12D and 24D specimens is nearly identical.

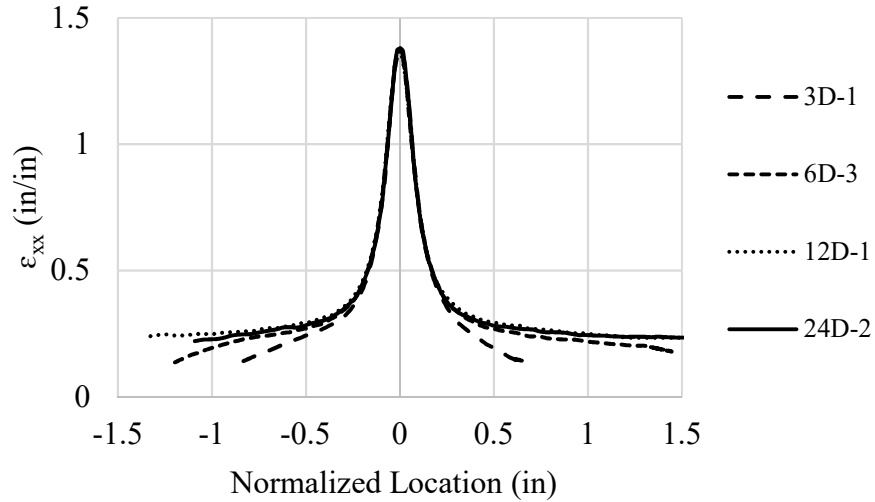


Fig. 3.12. Longitudinal engineering strain along length of specimen at rupture load.

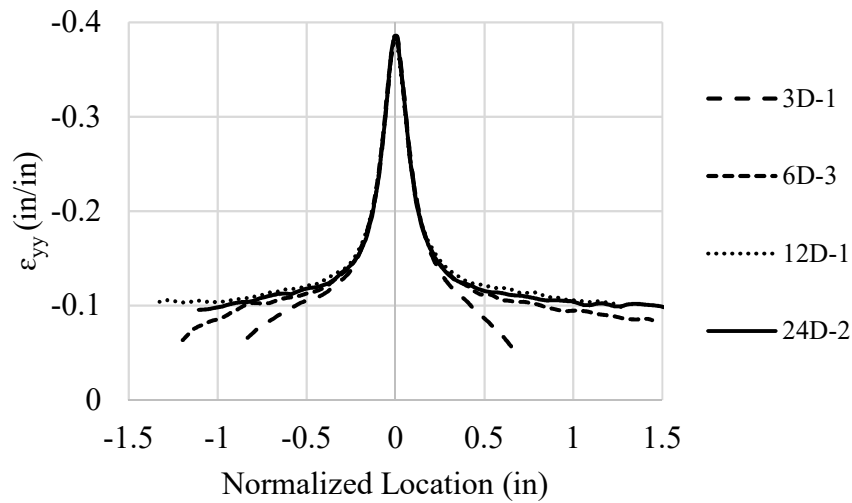


Fig. 3.13. Transverse engineering strain along length of specimen at rupture load.

Furthermore, the experiments showed that the longitudinal engineering strain continues to increase throughout the specimen length until the strain localization occurs. In other words, the load-displacement curve follows the primary path beyond the peak load until the bifurcation point, where localized necking initiates and the load-displacement curve starts to follow the bifurcation path (see Fig. 3.14a). The experimental results showed

that the strains along the specimens are higher at the onset of localization (bifurcation point) than at the peak load. Fig. 3.14b shows that the strains in the 24D-2 specimen are higher at the bifurcation point than at the peak load.

After the peak load, the deformation increases along the entire length following the primary path until the bifurcation point where the strain localizes into a zone and the rest of the member unloads elastically (see Fig. 3.14a). The strain rate increases inside the localization zone and decreases outside it as found in Bao et al. (2016). Thus, the steel specimen follows the primary path after the peak load until the strain localization occurs. After the bifurcation point, however, the longitudinal engineering strain and its rate keeps increasing inside the localization zone while outside the localization zone, longitudinal engineering strain decreases (see Fig. 3.14b). Therefore, strain localization is an instability problem because when it occurs, it switches from the primary path of load-deformation curve to the bifurcation path as shown in Fig. 3.14a.

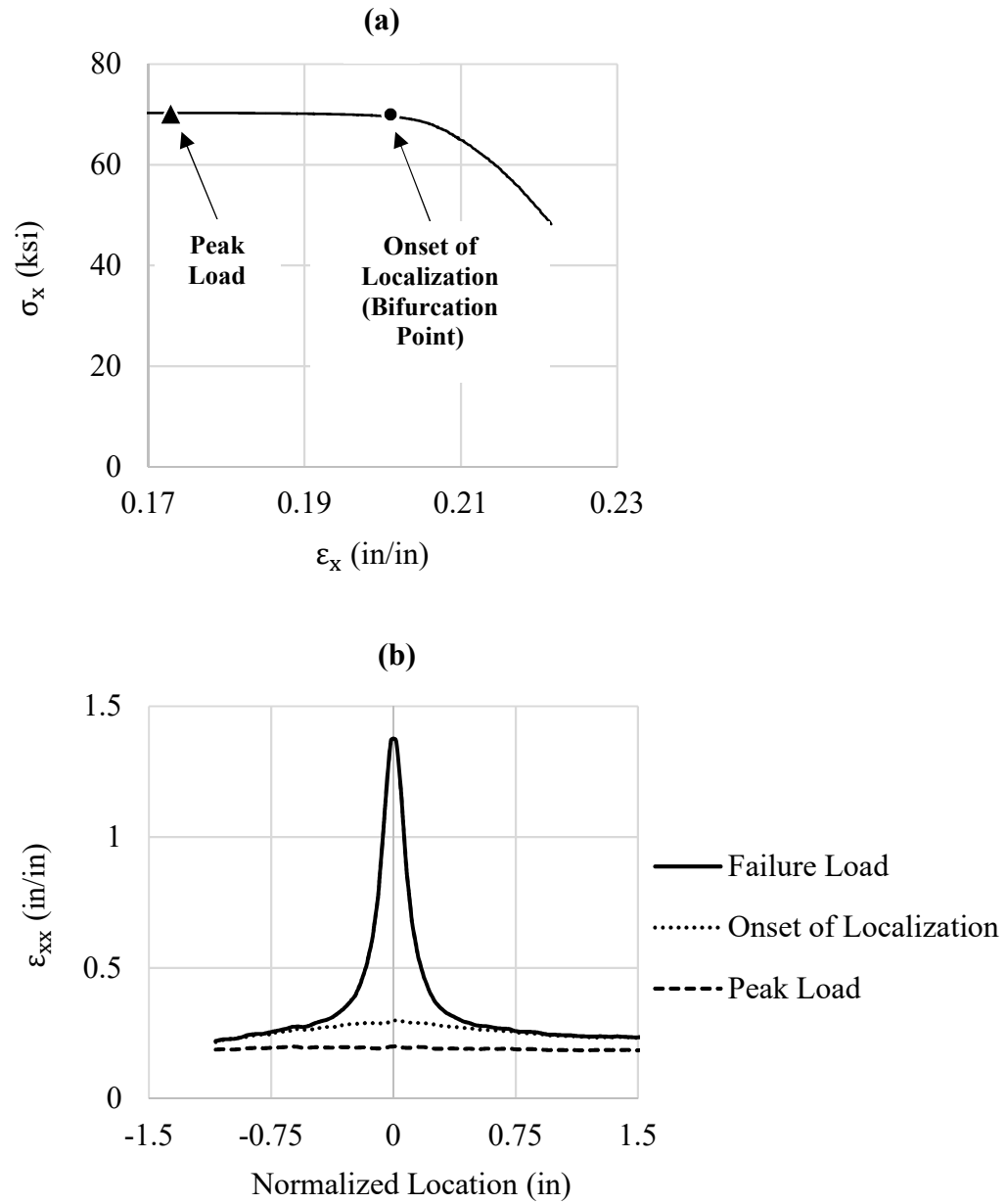


Fig. 3.14. (a) Engineering stress-strain curve of 24D-2 specimen, and (b) longitudinal Engineering strain.

3.6. Determination of Localization Length

Determination of the localization length may be ambiguous because the localization length is extracted from the internal material property of microscopic structure and fitted to the macroscopic experimental load displacement curve. Schreyer and Chen (1986) considered the peak load as a trigger of the strain localization where a part of the member undergoes loading (experienced as softening) and the rest unloads elastically. Recently, Kolwankar et al. (2017) calculated the localization length of cylindrical bars simulated through FEA. They found that the strain localization starts at the peak load. The localization length was calculated by comparing the engineering strain and the longitudinal engineering strain at the same loading instant. These methods of calculating the localization length, however, have drawbacks because these methods are based on numerical models rather than experiments and both methods assumed the strain localization starts at the peak load.

This paper proposes a novel method and a modified method for determination of the localization length of cylindrical steel bars named longitudinal strain method and average strain method, respectively. The proposed methods are described and compared in the next sections.

3.6.1. Average Strain Method

The average strain method of determination of localization length is similar to the method used by Kolwankar et al. (2017). The localization length is the distance between the two distinct points intersected by the longitudinal engineering strain and the engineering strain at the same loading instant. Fig. 3.15 shows the length of localization zone determined at the rupture load of the 12D-1 specimen. The localization length at peak

and rupture loads calculated using the experimental results for specimens 3D-1, 6D-3, 12D-1 and 24D-2 are shown in Table 3.2. Kolwankar et al. (2017) found that the localization length calculated at the peak load is almost five times the diameter of the bar. However, localization lengths shown in Table 3.2 at peak and rupture loads vary with the length of the specimen and are not the same as 5 times the bar diameter. The experimental results show that the strain localization calculated by this method starts well before the peak load which violates the definition of strain localization where part of the member has to unload elastically while the unloading cannot occur before the peak load for the monotonic loading state. This may make the longitudinal strain method is the best method to determine the localization length.

3.6.2. Longitudinal Strain method

In the longitudinal strain method, the localization length is determined based on the longitudinal engineering strain data only. By using only longitudinal engineering strain the true behavior of the evolution of the localization length can be better reflected. The localization length is calculated by the distance between two distinct points intersected by the longitudinal engineering strain profile at the rupture load ($\epsilon_{xx,r}$) and at a given loading instant. Fig. 3.16 shows the localization length determined at 90% of the peak load (10% drop in load). Following this method to calculate the localization length, the results show that the strain localization occurs beyond the peak load, at the bifurcation point, which agrees with strain localization definition. Table 3.2 shows that the localization length is very similar for all specimens (except specimens with length 3D). The average of localization length at the onset of localization of 6D-3, 12D-1 and 24D-2 specimens is 2.66

in. which is almost five times the diameter of tested specimens. The shorter length of the 3D specimen may be due to end effects on the short specimen. While the localization length determined just before the rupture load is 0.3 ± 0.005 in. and is consistent for all specimens.

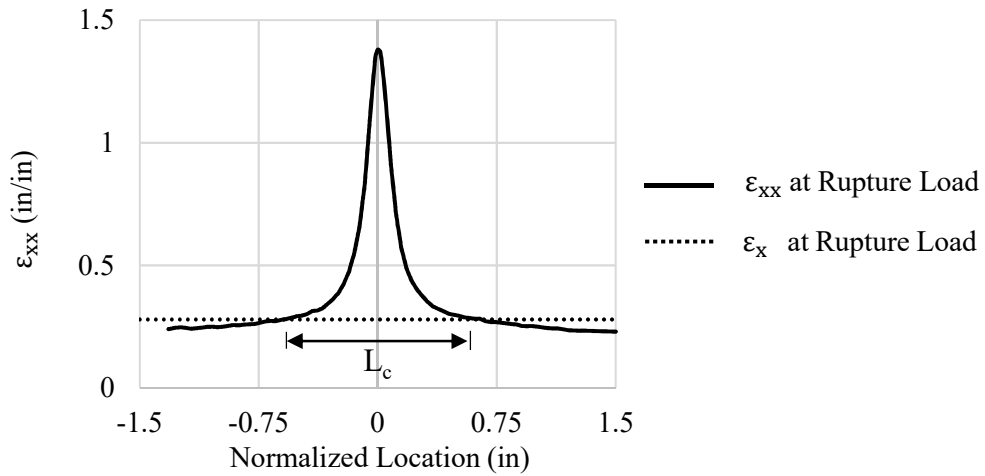


Fig. 3.15. Determination of localization length using average strain method and (data from 12D-1 specimen).

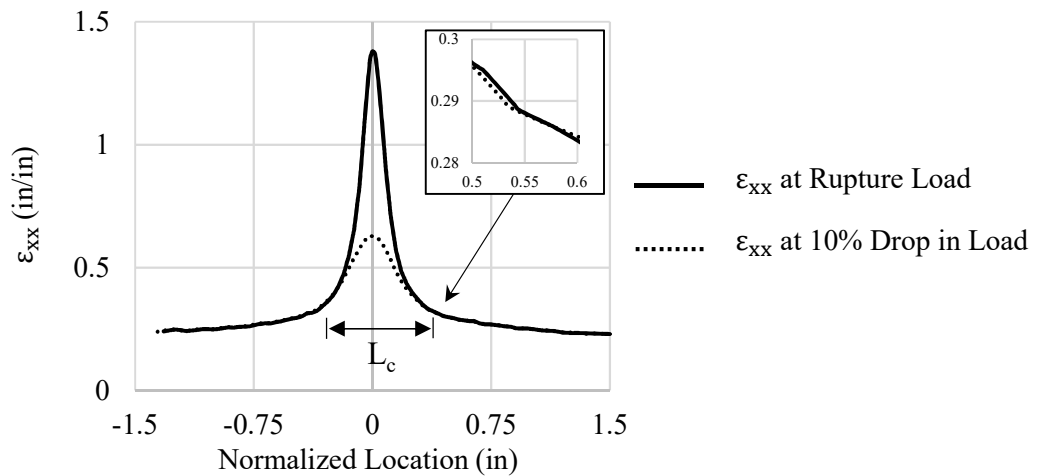


Fig. 3.16. Determination of localization length using longitudinal strain method (data from 12D-1 specimen).

Table 3.2. Localization length determined by average strain and longitudinal strain methods

Specimen	Average Strain Method		Longitudinal Strain
	Lc at Peak Load	Lc at Rupture	Method
I.D.	(in)	Load (in)	Lc at Bifurcation Point (in)
3D-1	0.972	0.452	1.459
6D-3	1.679	0.693	2.612
12D-1	3.534	1.281	2.507
24D-2	7.036*	2.984	2.863

* extrapolated

3.7. Evolution of Localization Length

To further investigate the evolution of localization length during the softening process, the localization length calculated by average strain method was plotted vs. the normalized strain in Fig. 3.17a and Fig. 3.17b. The values of 0 and 1 represent peak and rupture loads, respectively and ϵ_0 and ϵ_f are the engineering strain at the peak and rupture loads, respectively. Data for the 24D specimen was limited due to range of 3D DIC image size. Fig. 3.17a gives the localization length on the vertical axis while Fig. 3.17b gives the localization length divided by the specimen length. Plotting the normalized localization length (L_c/L) shows very similar behavior with specimens of different length. The average value of L_c/L of 3D-1, 6D-3, 12D-1 and 24D-2 specimens calculated at the peak and rupture loads are 0.5863 and 0.2419 respectively. The difference in the Fig. 3.17a and Fig. 3.17b

shows that the specimen length influences the localization length when using the average strain method. Furthermore, both Fig. 3.17a and Fig. 3.17b indicate that the strain localization actually begins well before the peak load (after the yield) and the localization length decreases gradually with increasing strain. While FEA simulations by Kolwankar et al. (2017) show an abrupt change at the peak load when the strain localization occurs. The difference in the experimental and FEA behavior can be explained by the fact that the experimental longitudinal engineering strain profile is not perfectly uniform (non-homogenous strain field) as also described in Li and Karr (2009). While material instability theory and the FEA show a homogenous strain field (uniform deformations along the specimen length) until the peak load (described by Okazawa (2010)).

The evolution of localization length determined by longitudinal strain method was also investigated by plotting the localization length with normalized strain of specimens 3D-1, 6D-3, 12D-1 and 24D-2 as shown in Fig. 3.17c. Unlike the average strain method, the longitudinal strain method shows that the strain localization starts beyond the peak load at the bifurcation point when the localized necking initiates (see Fig. 3.10). The results, plotted in Fig. 3.17c, show that the normalized strain values when the strain localization starts are 0.27, 0.33, 0.56 and 0.62 for 3D-1, 6D-3, 12D-1 and 24D-2 specimens, respectively. When the strain localization occurs, the localization length drops sharply then decreases gradually until the rupture load. The results shown in Fig. 3.17c show that the strain localization of 12D-1 and 24D-2 specimens starts well into the post-peak region. It can be projected that for a very long specimen, the normalized strain may approach 1.0 which means that the engineering strain at the onset of localization (ϵ_{10c}) approaches the engineering strain at the rupture load (ϵ_r). In other words, once the localized necking

initiates, the specimen may experience a sudden drop in load and a brittle failure. Relative similarity in the evolution of localization length with different specimen length was achieved by normalizing the engineering strain at the bifurcation point. The evolution of localization length was replotted in Fig. 3.17d (the values of 0 and 1 represent bifurcation point and the rupture load, respectively). The evolution of localization length shown in Fig. 3.17d is quite similar for all specimens of different lengths, except the 3D-1 specimen where the localization length cannot be longer than the specimen length. Experimental results show that the load associated with ϵ_{loc} is slightly different for all specimens. In other words, the strain localization starts at a different percentage of drop in load which may be due to specimen preparation and initial imperfections. The engineering strain at the onset of localization and percent of drop in load associated with ϵ_{loc} to the peak load are given in Table 3.3.

Empirical equations for the evolution of the localization length for both the average strain and longitudinal strain methods can be determined to predict the localization length of specimens with variable length. Equations 3.1 and 3.2 give the best fit line based on the experimental data.

$$L_c \text{ (average strain method)} = L_o \left[0.6 - 0.35 * \left(\frac{\epsilon_x - \epsilon_0}{\epsilon_r - \epsilon_0} \right) \right] \quad (3.1)$$

$$L_c \text{ (longitudinal strain method)} = 5D e^{-2.8 \left(\frac{\epsilon_x - \epsilon_{loc}}{\epsilon_r - \epsilon_{loc}} \right)} \quad L \geq 6D \quad (3.2)$$

Equation 3.1 depends on the engineering strain at peak and rupture loads which depends on the specimen length. However, Equation 3.2 depends on the engineering strain at bifurcation and at the rupture load for a specific specimen length. Based on the

experiments, it can be assumed that the bifurcation point can occur at around 1% drop in load. The engineering strain at peak and rupture loads are in Table 3.1. Equations 3.1 and 3.2 are only for specimens with a 0.5 in. diameter. As shown in analytical analysis by (Kolwankar et al. 2017) the localization length scales directly with specimen diameter. However, this will need to be confirmed in future experimental studies.

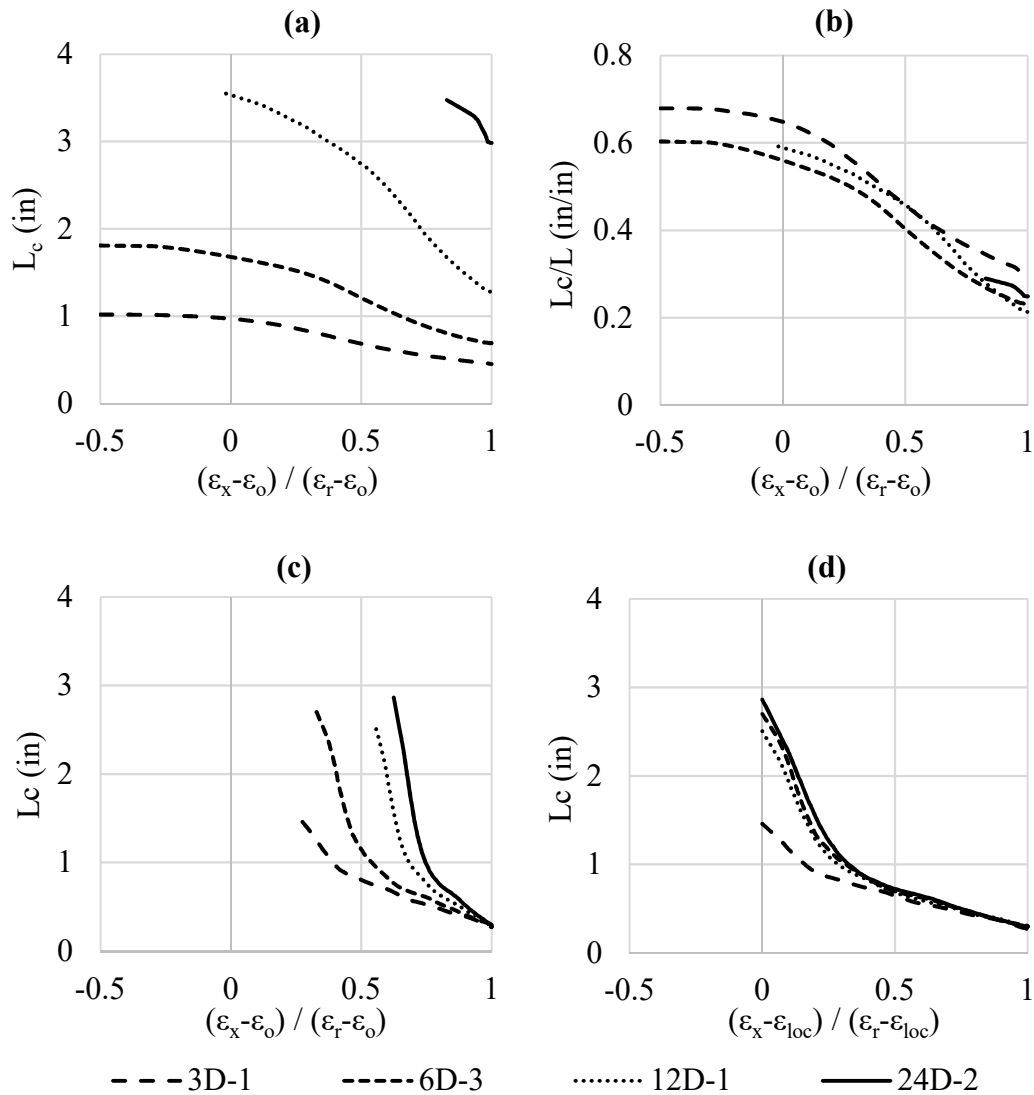


Fig. 3.17. The evolution of the localization length (a) and (b) Average strain method and (c) and (d) Longitudinal strain method.

Table 3.3. Engineering strain and drop in load at the onset of the localization

Specimen I.D.	ϵ_{loc} (in/in)	Drop in Load (%)
3D-1	0.2421	1.0
3D-2	0.2455	1.2
3D-3	0.2381	0.9
6D-1	0.2336	1.1
6D-2	0.2342	1.3
6D-3	0.2355	0.8
12D-1	0.2361	1.3
12D-2	0.2320	1.0
24D-1	0.2004	1.1
24D-2	0.2011	0.9

3.8. Stress Strain Behavior of Localization Length

To examine the influence of the localization length on the post-peak behavior, the engineering stress-strain curves for specimens 3D-1, 6D-3, 12D-1 and 24D-2 for a section inside the localization zone is investigated. In case of the engineering stress-strain curve of localization length determined by average strain method, the softening curve starting from the peak load till rupture load is considered. For simplifying the illustration of the softening curve of the engineering stress-strain, a best fitted line of the softening curve is calculated by considering the peak load in case of the average strain method or the bifurcation point in case of the longitudinal strain method is the interception point. Fig. 3.18 shows the results with the localization length calculated at the rupture load by average strain method

as shown in Table 3.2. The softening curve of the engineering stress-strain is extremely size dependent. The longer specimens, which have longer localization lengths, have steeper slope of the best fitted line of softening curve ($-\beta E$) (see Table 3.4). The difference in softening curve shown in Fig. 3.18 may not be due to the amount of deformations inside the localization zone but because of the differences in the localization length of each specimen (longer specimen has longer localization length). As a result, for the same specimen length with same longitudinal engineering strain behavior (see Fig. 3.14b and Fig. 3.15), the longer the localization length, the steeper $-\beta E$. This variation in the βE may be considered a drawback to the average strain method.

Fig. 3.19 shows influence of the localization length determined by longitudinal strain method for a section inside the localization zone where the localization length was calculated at bifurcation point as shown in Table 3.3. The engineering stress-strain curve for specimens of different lengths is very close. $-\beta E$ of the data shown in Fig. 3.19 is calculated based on the softening curve starting from the bifurcation point till the rupture load. Specimens 6D-3, 12D-1 and 24D-2 have $-\beta E$ within 10% (see Table 3.4). The similarity in softening curve shown in Fig. 3.19 as compared to Fig. 3.18 may be due to the difference in the length of the localization zone calculated by the two methods. The similarity of engineering stress-strain curve calculated in the localization zone is one of main advantages of the longitudinal strain method.

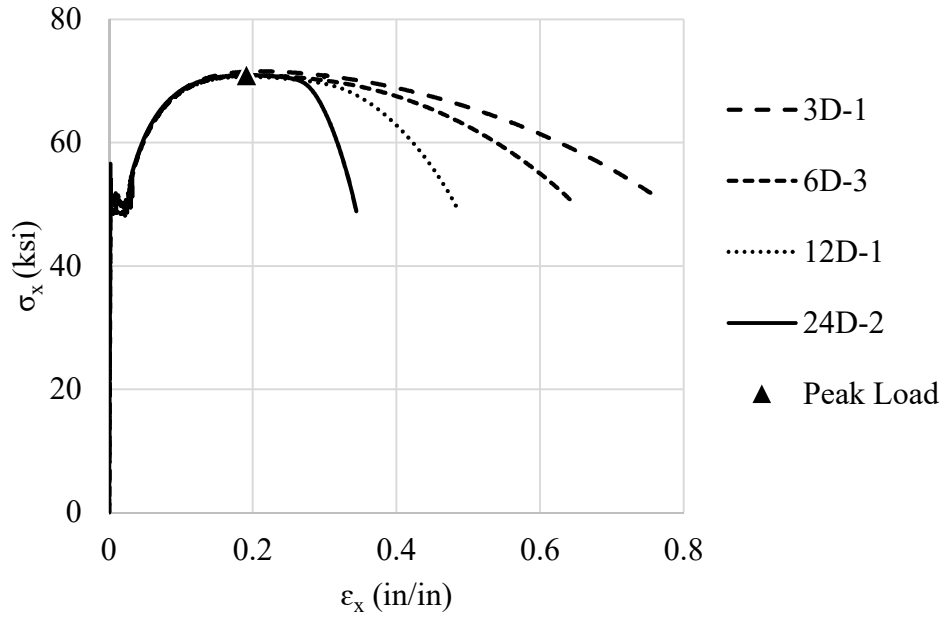


Fig. 3.18. Engineering stress-strain along localization zone calculated by average strain method at rupture load

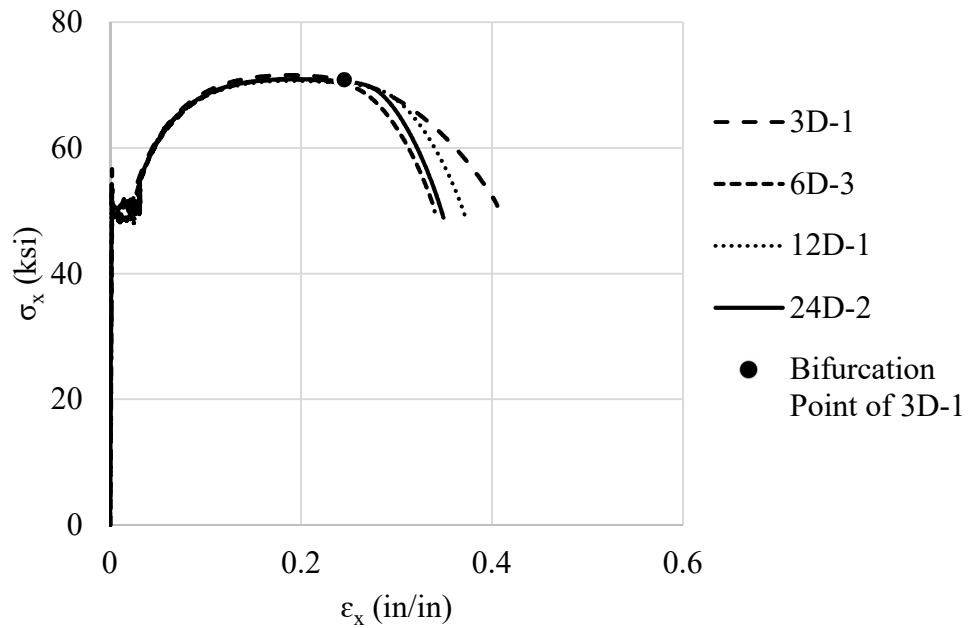


Fig. 3.19. Engineering stress-strain along localization zone calculated by longitudinal strain method at bifurcation point

Table 3.4. The slope secant of the softening curve of engineering stress strain curve of the localization zone

Specimen I.D.	Average strain	Longitudinal strain
	method	method
	$-\beta E$ (psi)	$-\beta E$ (psi)
3D-1	-27353	-96322
6D-3	-32415	- 141300
12D-1	-41429	- 148200
24D-2	-65445*	- 173100

* extrapolated

To investigate the influence of the evolution of the localization length on the post-peak behavior, the engineering stress-strain curve of a localization length corresponding to the instantaneous localization zone are plotted in Fig. 3.20 and Fig. 3.21. The engineering stress-strain shown in Fig. 3.21 is almost the same for all tested specimens due to the similarity of the evolution of localization length calculated by longitudinal strain method. Contrarily, Fig. 3.20 shows the variation of the engineering stress-strain due to the difference in the evolution of localization length calculated by average longitudinal method. The results shown in Fig. 3.21 confirm that the post-peak response (i.e. after the bifurcation point) is due to the ratio of deformations happening in the localization zone. These experimental results can be used to develop a numerical model that can predict the post-peak response of a one-dimensional steel member.

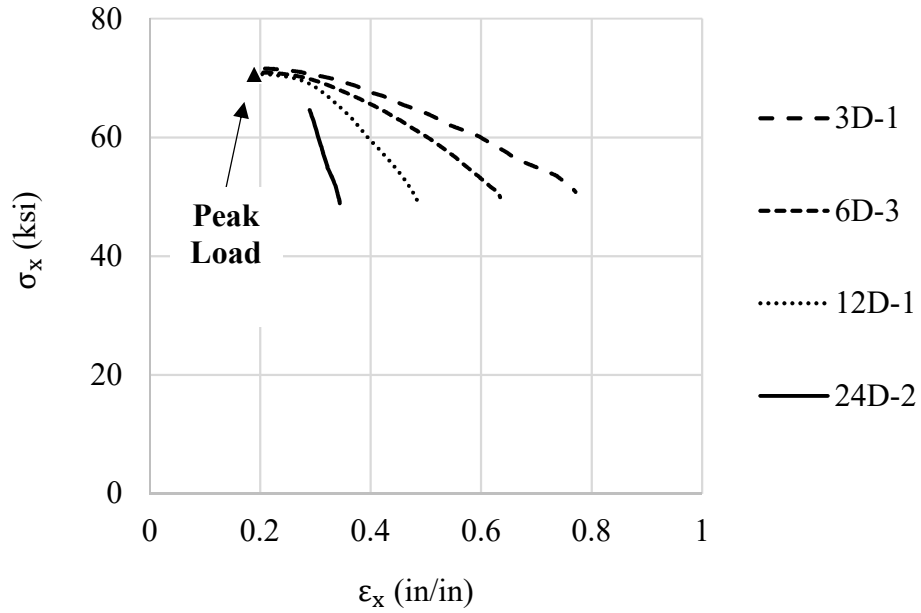


Fig. 3.20. Engineering stress-strain of instantaneous localization zone determined by average strain method

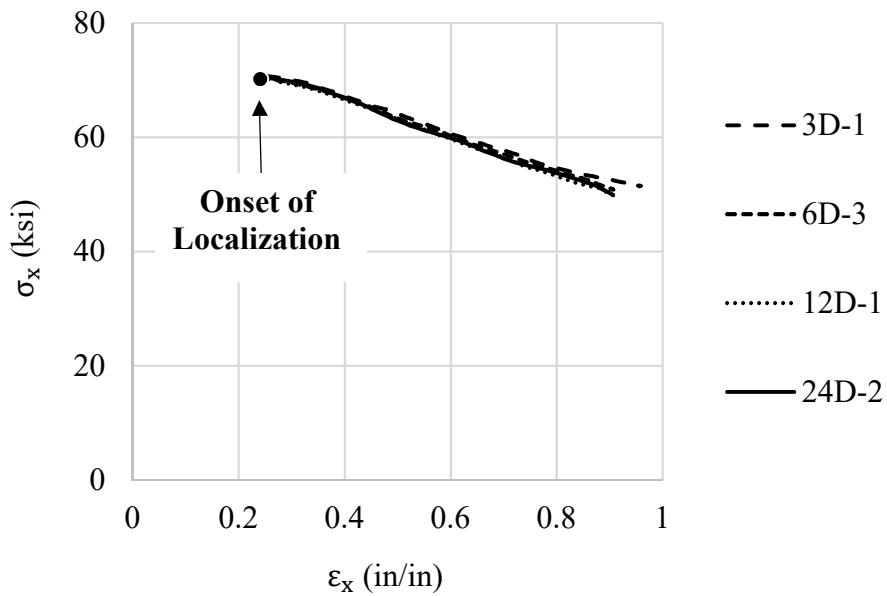


Fig. 3.21. Engineering stress-strain of instantaneous localization zone determined by longitudinal strain method.

3.9. Summary of Localization Length Methods

The localization length plays a major role in determining the post-peak response.

Two methods of determining the localization length were presented in the previous section.

Comparisons of both methods are summarized in Table 3.5.

Table 3.5. Comparisons of average and longitudinal strain methods

Average strain method	Longitudinal strain method
-Localization length can be calculated based on comparing the engineering strain and the longitudinal engineering strain at a loading instant.	-Localization length can be calculated based on comparing the longitudinal engineering strains at the rupture load and a loading instant.
-The results show that the strain localization starts well before the peak load which violates the definition of strain localization where elastic unloading has to occur.	-The strain localization starts at the bifurcation point when the actual localized necking initiates
-The evolution of the localization length is size dependent and relatively proportional to the specimen length.	-The evolution of the localization length is almost identical for specimens 3 in. and longer.
-Engineering stress-strain along the localization zone is highly size dependent because localization length depends on specimen length even though the longitudinal engineering strain is quite similar for all specimens.	-Engineering stress-strain along the localization zone is similar for all specimens and this reflects the similarity of the longitudinal engineering strain.
-Engineering stress-strain calculated within the instantaneous localization zone is size dependent for all tested specimens due to the variety of the evolution of localization zone.	-Engineering stress-strain calculated within the instantaneous localization zone is approximately similar for all tested specimens due to the similarity of the evolution of localization zone.

3.10. Strain Rate

Strain rate is the change in strain over time. It determines the testing speed and how fast the specimen is straining. The change in the strain rate along the specimen may define the bifurcation path. The experiments show that, up to the peak load, the strain rate stays the same across the specimen length except at the yield point as shown in Fig. 3.22. When the peak load is reached, the strain rate gradually increases inside the localization zone, while outside the localization zone, it slowly decreases. When the bifurcation point is reached, the strain rate outside the localization zone becomes zero and the specimen leaves the main path and follows the bifurcation path which eventually leads to strain localization. Fig. 3.22 shows that, after the bifurcation point, the strain rate increases dramatically in the center of the localization zone because the post-peak deformations are due to the deformations occurring inside the localization zone which explains why the post-peak response is steeper for longer specimen. Furthermore, Fig. 3.23 shows that longer specimen has higher testing strain rate even though all tested specimens have the same testing strain rate. The strain rate after the bifurcation point is higher. Fig. 3.23 shows the strain rate of 3D-1, 6D-3, 12D-1 and 24D-2 specimens versus the normalized testing time (where 1 represents the peak load), and the bifurcation points are represented as dots. The change in the strain rate after the peak load till the bifurcation represents the increase in engineering strain outside the localization zone as shown in Fig. 3.24. The engineering strain keeps increasing but in slower pace than the one inside the localization zone till the bifurcation point where outside the localization zone starts to unload elastically. This type of behavior explains why the steel specimens follow the primary path of the load displacement curve after the peak load till the bifurcation point where the steel specimens switch to bifurcation

path which is steeper for longer specimens than shorter ones. Hence, the bifurcation point may numerically be considered the point at which steel specimen starts to unload elastically.

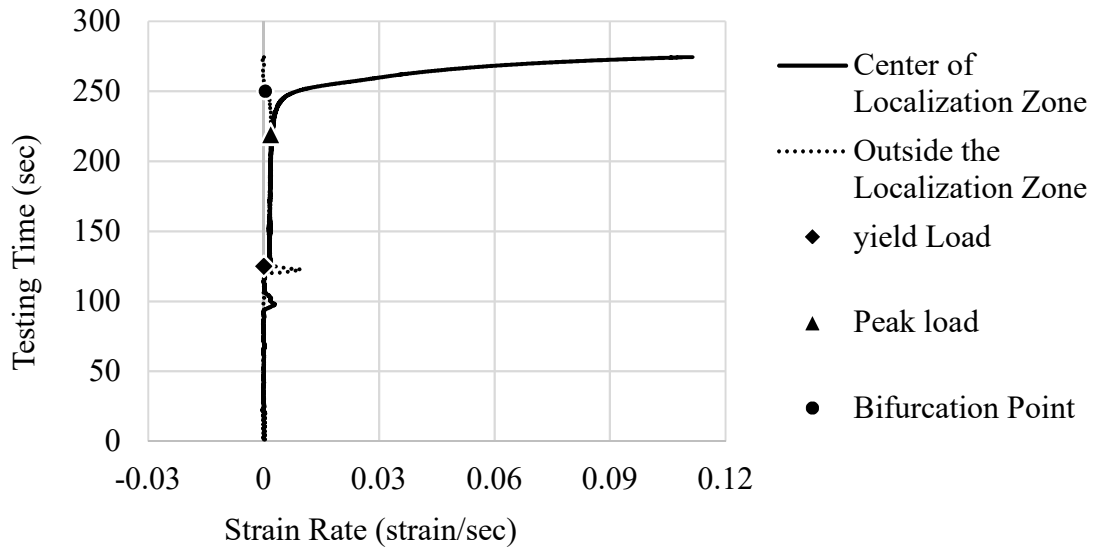


Fig. 3.22. Strain rate at the center and outside the localization zone of 12D-1 specimen

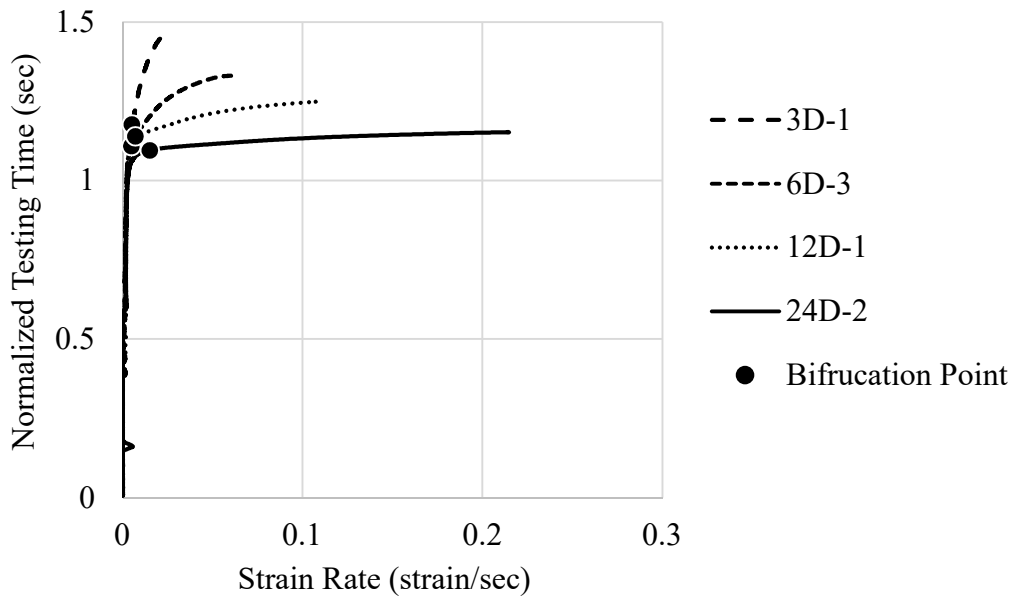


Fig. 3.23. Strain rate for steel specimens with four different lengths

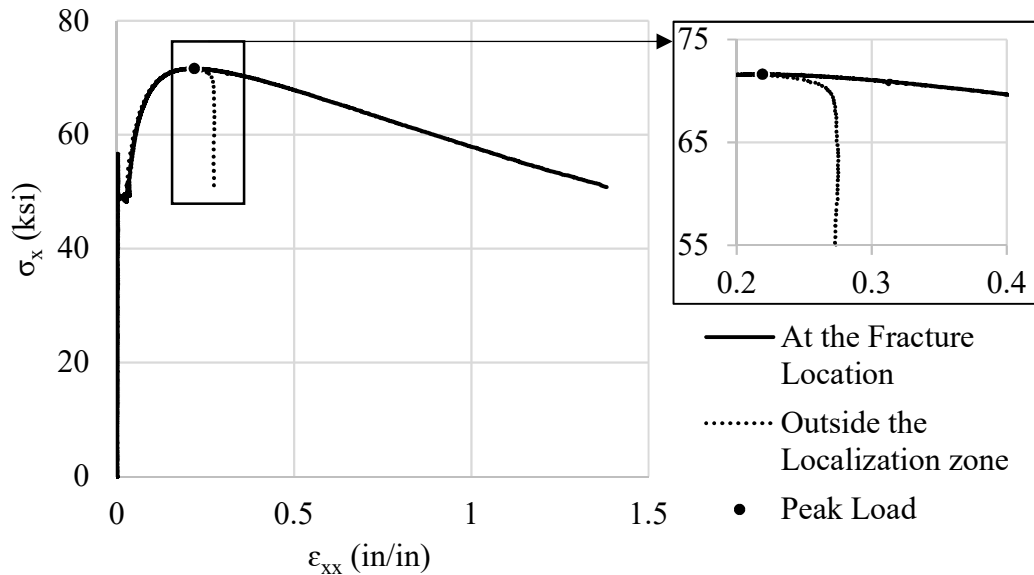


Fig. 3.24. Engineering stress vs strain at fracture location and a point outside the localization zone of 3D-1 specimen

3.11. Summary and Conclusions

The experimental study on cylindrical low-carbon steel specimens demonstrates the evolution of the localization length during the post-peak responses for specimens of different lengths. The results showed that the post-peak behavior was influenced by the specimen length as expected, in which longer specimens have steeper, almost brittle, post-peak curves. The results showed that longitudinal and transverse strain fields as a function of longitudinal axis (x-axis) are similar at failure load near the center of the localization, but as the length of the specimen decreases so does the longitudinal engineering strains away from the center of the localization. The experimental results also showed that the

strains along the specimens are higher at the onset of localization (bifurcation point) than at the peak load. In other words, strain localization does not start at the peak load. Furthermore, the strain rate decreases gradually outside the localization zone after the peak load and becomes zero at the bifurcation point while the strain rate inside the localization zone increases dramatically up to failure. To calculate the localization length of cylindrical low carbon steel specimens, two methods are presented as follows:

1. In the average strain method, the localization length is defined to be the distance between the two points at which the longitudinal engineering strain field at a load and the engineering strain field intersect. The results demonstrate that the strain localization starts significantly before the peak load which does not agree with the definition of the strain localization. The localization length calculated by this method depends on the specimen length, i.e. longer localization lengths for longer specimens. As a result, the engineering stress-strain calculated in the localization zone is also size-dependent due to the inconsistency of the localization length for different specimen lengths. However, normalized localization lengths (L_c/L) are relatively similar, and can be estimated by a linear curve fitting formula.
2. In the longitudinal strain method, the localization length is defined to be the distance between the two points at which the longitudinal engineering strain field curve intersects the curve at rupture load. The results illustrate that the strain localization occurs beyond the peak load at the bifurcation point where the localized necking initiates. This agrees with the definition of the strain localization. The strain localization happens at slightly different loads (e.g. 1.02%, 0.8%, 1.26% and 0.86% drop in load for 1.5 in., 3 in., 6 in. and 12 in. specimen, respectively). The

load point may be influenced by small imperfections in the members. By normalizing the strains at the bifurcation point for all specimens, the evolution of localization length is approximately identical for specimens whose lengths are 3 in. or more. The evolution of localization length can be described by an exponential curve fitting function. With the use of this method, the engineering stress-strain calculated with respect to the instantaneous localization length shows similar behavior for different specimen lengths.

Determining the localization length with the longitudinal strain method could produce better results for modeling and simulation to be reported in the future work. It is also found that the localization length is not constant, but evolves as the specimen moves through the post-peak regime. Further study is required for the specimens of different materials and diameters.

CHAPTER FOUR

CHAPTER 4: ANALYTICAL AND NUMERICAL ANALYSIS

4.1. Introduction

Simulation of extreme limit states, such as post-peak response, is important in understanding the load redistribution and collapse behavior of structures. These extreme limit states are currently simulated through established methods of spring or hinge models, fiber models, continuum finite element analysis (FEA), and nonlocal models. However, each of these methods have definitive drawbacks when attempting to simulate the post-peak behavior. Hinge models rely on component-specific tests and cannot simulate the spread of plasticity. Moreover, hinge models are heavily size dependent when it comes to post-peak softening (Bažant, 2003b). Fiber models attempt to simulate these effects but do not effectively handle softening and associated localization behavior because post-peak behavior is sensitive to the discretization of integration points along the length of the member. Continuum finite element models are capable of modeling post-peak response but are computationally expensive and also extremely sensitive to discretization when modeling post-peak behavior. The discretization or mesh sensitivity has been overcome by developing nonlocal models. However, in order to make nonlocal models fully capable of capturing the post-peak response and surpassing the non-objectivity, a characteristic length (or localization length) over which the strain is averaged has to be determined. For instance, Kolwankar et al., 2017 formulated a uniaxial nonlocal model however, the localization length was based on finite element analysis results. Sideris and Salehi (2016) introduced a novel gradient inelastic beam theory and a corresponding flexibility-based frame element

formulation to treat major weaknesses of existing flexibility-based frame element formulations. However, the localization length (or characteristic length) was assumed not based on experimental data. Another numerical model to simulate the post-peak response was developed by Chen and Schreyer (1990) but their results showed that post-peak response is dependent on both mesh size and initial imperfection.

A numerical localization model that can reasonably simulate the post-peak behavior while eliminating the mesh-dependence for softening material constitutive response is needed. This paper presents new localization models to predict the post-peak behavior of one-dimensional steel members under tension. The localization length is based on experimental results presented in chapter three. The numerical model is capable of mitigating mesh sensitivity and size effect to achieve a generalized numerical model. The numerical localization model is dependent on localization length (L_c) and deformations occurring inside the localization zone. The two methods of determination of localization length, average strain method and longitudinal strain method presented in chapter three are deployed in the numerical model to create linear and bilinear post-peak numerical models. Furthermore, the evolution of the localization length and the deformations inside it are presented as empirical equations throughout the softening process to provide a new nonlinear numerical model that can accurately simulate the nonlinearity of the post-peak region. Comparison of the linear, bilinear and nonlinear post-peak numerical model with the experimental results are presented. Furthermore, a FEA model is developed to simulate the post-peak response of cylindrical steel bar under tension and compared with the experimental data.

4.2. Previous Experimental Results

The experimental results of A36 cylindrical steel specimens with four different lengths explained in chapter three, shown in Fig. 4.1, are used as the basis for the localization length (L_c) and the softening region of the constitutive relation inside the localization length ($-\beta E$). The localization length was determined using two methods: average strain method and longitudinal strain method. The average strain method defines localization length by the distance between the two distinct points intersected by the longitudinal engineering strain along the longitudinal axis of the specimen, ϵ_{xx} , and the engineering strain, ϵ_x , (same as the averaged longitudinal engineering strain along the specimen) at the same loading instant. The longitudinal strain method defines localization length by the distance between the points intersected by the longitudinal engineering strain at a loading instant and the one at the rupture, $\epsilon_{xx,r}$. The average strain method shows that the strain localization occurs before the peak load. Furthermore, the localization length is size dependent. The longitudinal strain method, on the other hand, shows that the strain localization occurs at the bifurcation point which is approximately around a 1% drop in load and the localization length is size independent. In both methods the localization length evolves, or changes, throughout the post-peak region. Table 4.1 gives the localization lengths determined by each method.

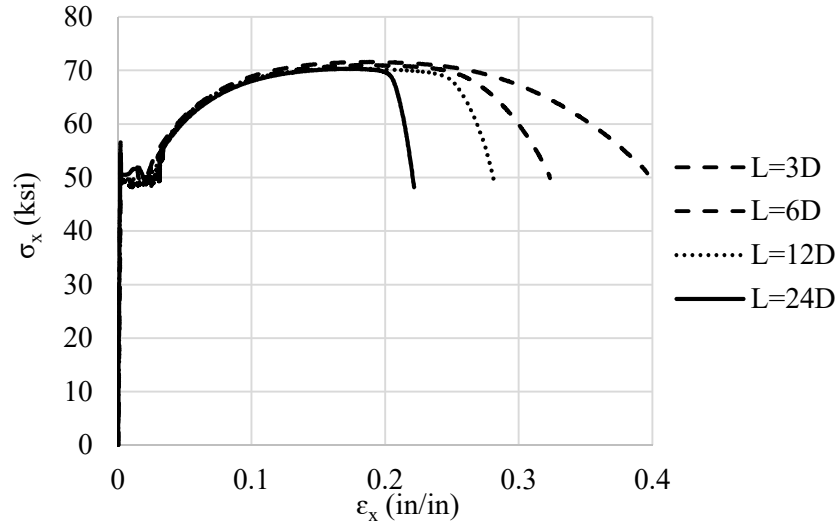


Fig. 4.1. Engineering stress vs. strain for cylindrical steel specimens

The slope of secant line of the softening region ($-\beta E$, β donates the softening factor) of the constitutive relation of the localization zone was determined as shown in Fig. 4.2. This stiffness is determined by the deformations occurring inside the localization zone. These deformations can be measured by looking at the softening region of the engineering stress versus engineering strain inside the localization zone. In the average strain method, the softening region starts from the peak point to the rupture while in the longitudinal strain method, the softening region starts from 1% drop in engineering stress to the rupture. For both methods the localization length must be used. However, the localization zone is evolving or changing during the softening process. Therefore, the localization length determined by average strain method at both the peak load and rupture is used. For the longitudinal strain method, however, only the localization length determined at 1% drop in load is used. The average strain method yielded that the softening factor is size dependent (see Table 4.1). However, the longitudinal strain method showed that the softening factor is approximately 0.005 (see Table 4.1). The experiments presented in chapter three showed

that the constitutive relation of the instantaneous localization zone throughout the softening region (evolution of the localization length) is linear which ultimately leads to constant softening factor of approximately 0.001.

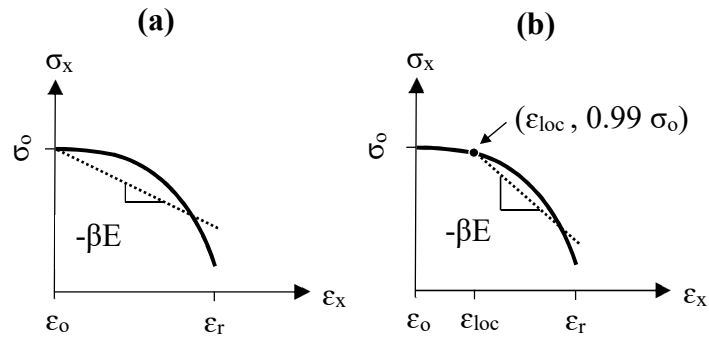


Fig. 4.2. Determination of softening factor based on engineering stress-strain inside the localization zone determined by (a) average strain method and (b) longitudinal strain method

Table 4.1 Localization length and softening factor determined by average strain and longitudinal strain methods

Specimen ID	Average Strain Method		Longitudinal Strain Method			
	Peak Load		Rupture Load		Bifurcation Point	
	L_c	β	L_c	β	L_c	β
3D	0.67 L_0	0.0012	0.33 L_0	0.0009	2.9 D	0.003
6D	0.57 L_0	0.0016	0.23 L_0	0.0011	5.2 D	0.005
12D	0.60 L_0	0.0024	0.22 L_0	0.0014	5 D	0.005
24D	0.58 L_0^*	0.0037*	0.25 L_0	0.0022	5.8 D	0.006

*extrapolated

4.3. Numerical Localization Model

A numerical localization model was modified from Schreyer and Chen (1986) and developed based on experimental data presented in chapter three to simulate the post-peak response of a one-dimensional steel member subjected to monotonic tension. It is assumed that the member consists of two regions, A and B as shown in Fig. 4.3a, and the strain is distributed uniformly along both regions as shown in Fig. 4.3b. Both regions have the same constitutive relationship up to the onset of strain localization. It is assumed that the strain localization numerically occurs either at the peak load or the bifurcation point, as shown in Fig. 4.4, depending on the localization length method; average strain method or longitudinal strain method. Once the strain localization occurs, the strain localizes uniformly into region A whose length is L_A (same as L_c), as shown in Fig. 4.3b, following the softening branch of the constitutive relation of region A, and Region B unloads elastically. Three softening constitutive relationships (linear, bilinear, and nonlinear) shown in Fig. 4.4 are proposed. Hence, three post-peak models (linear, bilinear, and nonlinear) shown in Fig. 4.5 are investigated to examine the post-peak behavior of one-dimensional steel member subjected to monotonic tension. Table 4.2 shows which localization length method was used for each post-peak model. The general pre- and post-peak stiffnesses are derived in the following sections.

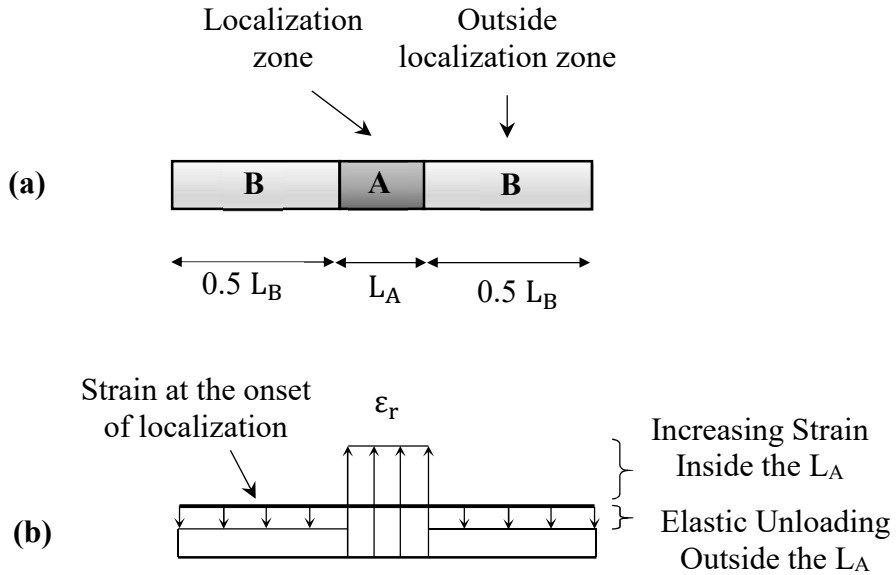


Fig. 4.3. (a) Description of localization zone in the numerical model, and (b) engineering strain distribution in localization model

Table 4.2. Post-peak models versus determination of localization length methods

Post-Peak Models	Determination of Localization Length Methods	
	Average Strain Method	Longitudinal Strain Method
Linear	✓	-
Bilinear	-	✓
Nonlinear	-	✓

4.3.1. Pre-Peak Behavior

In the first stage of loading, the steel member deforms elastically based on the modulus of elasticity. Once the steel member experiences yielding, second stage starts (i.e. hardening stage). Numerically, deformations are assumed to be uniform along the entire

length of the member up to the peak point (u_o, P_o). Therefore, the total incremental change in engineering strain along the entire length equals the incremental change in engineering strain in both region A and region B.

$$\Delta\varepsilon = \Delta\varepsilon_A = \Delta\varepsilon_B \quad P \leq P_o \quad (4.1)$$

The incremental change in engineering strain ($\Delta\varepsilon$) equals the incremental change in engineering stress ($\Delta\sigma$) divided by the modulus of elasticity (E) or the hardening modulus (E_h) of the material based on the stress state.

$$\Delta\varepsilon = \begin{cases} \frac{\Delta\sigma}{E} & (\sigma < \sigma_y) \\ \frac{\Delta\sigma}{E_h} & (\sigma_y \leq \sigma \leq \sigma_o) \end{cases} \quad (4.2)$$

The incremental change in deformation of region A and region B can be calculated by the following expression.

$$\Delta u = \Delta\varepsilon L_o = \Delta\varepsilon_A L_A + \Delta\varepsilon_B L_B \quad (4.3)$$

From structural standpoint, the incremental change in external applied load (ΔP) equals the product of incremental change in total deformation (Δu) of specimen shown in Fig. 4.3a and the stiffness (K) of the member.

$$\Delta P = K \Delta u \quad (4.4)$$

By plugging Equations (4.1-4.4), the pre-peak stiffnesses of one-dimensional steel member under monotonic tension is as below.

$$K = \frac{A_o E}{L_o} \quad P < P_y \quad (4.5)$$

$$K_h = \frac{A_o E_h}{L_o} \quad P_y \leq P \leq P_o \quad (4.6)$$

Therefore, the pre-peak behavior is defined using only the specimen geometry (A_o, L_o) and material properties (E, E_h, σ_y).

4.3.2. Post-Peak Behavior

The peak load can numerically be predicted for a cylindrical steel bar using the famous equation suggested by Considère, 1885:

$$\sigma = \frac{d\sigma}{d\varepsilon} \quad (4.7)$$

in which σ and ε denote the true (Cauchy) stress and longitudinal true strain, respectively. The peak load occurs when the increase in stress due to strain hardening cannot compensate for the decrease in cross-sectional area due to straining. However, equation indicates that the peak load will occur at the initiation of the localized necking. For the purpose of the numerical model the peak load will be based on the given ultimate stress (f_u) times the current cross-sectional area (A).

During the post-peak region, the numerical localization model assumes that when the strain localization occurs, the strain localizes into a segment whose length is L_c following the softening branch of the constitutive relation (i.e. $-\beta E$) while the rest of the member unloads elastically. Average strain method shows that the onset of the strain localization occurs well before the peak load while longitudinal strain method shows that the strain localization happens at the bifurcation point (after the peak load). In order to employ the localization length calculated by the two methods into the numerical model, it is numerically assumed that the onset of the strain localization occurs either at the peak load if the average strain method data is used or at bifurcation point if the longitudinal strain method data is used.

Numerically, when the strain localization occurs, the localization zone (i.e. region A) follows the softening branch of the constitutive relation shown in Fig. 4.4 and the rest

of the member (i.e. region B) unloads elastically. The incremental change in engineering strain of both regions is as follows.

$$\Delta\varepsilon_A = \frac{\Delta\sigma}{-\beta E} \quad (4.8)$$

$$\Delta\varepsilon_B = \frac{\Delta\sigma}{E} \quad (4.9)$$

In which β denotes the softening factor (β_1 , β_2 and β_3 for linear, bilinear and nonlinear post-peak model, respectively). The total deformations after the strain localization equals the sum of deformations in region A and B. Plugging equations 4.8 and 4.9 into 4.3 yields:

$$\Delta u = -\frac{\Delta\sigma}{\beta E} L_A + \frac{\Delta\sigma}{E} (L_o - L_A) \quad (4.10)$$

The post-peak stiffness can be derived by plugging Equation 4.10 into Equation 4.4.

$$K_p = \frac{A_o \beta E}{\beta L_o - L_A (\beta + 1)} = f(A_o, L_o, E, L_A, \beta) \quad (4.11)$$

The derived softening stiffness K_p is a linear function of the geometry, material properties, softening factor, and the localization length. K_p depends on the localization length and softening factor which are influenced by the method of determination of localization length. For instance, Schreyer and Chen (1986), Chen et al. (2008) and Dai et al. (2011) numerically showed that for a fixed L_c , the longer the specimen, the steeper softening region. The steeper softening region leads to larger softening factor. But the experiments presented in chapter three showed that, during softening process, the localization length is evolving, and the softening factor is approximately constant. In the following sections, the three proposed post-peak models are discussed.

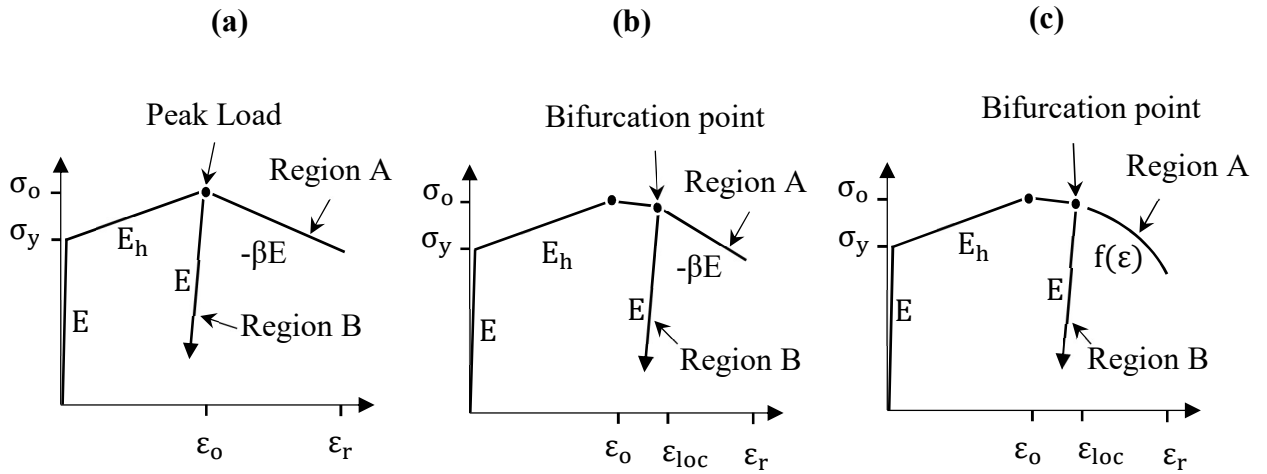


Fig. 4.4. Constitutive relationship for segment A and B (a) linear post-peak, (b) bilinear post-peak and (c) nonlinear post-peak models

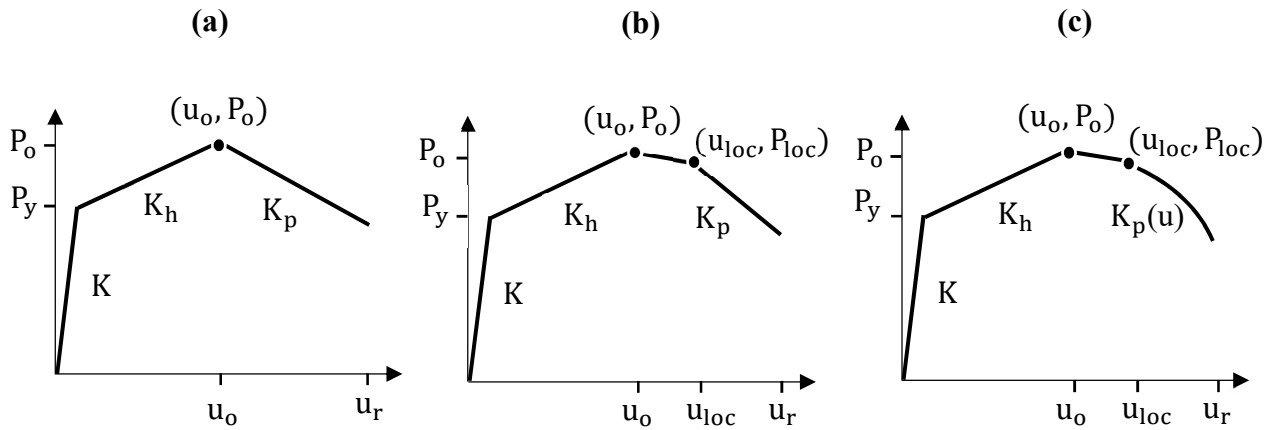


Fig. 4.5. Load displacement response (a) linear post-peak, (b) bilinear post-peak and (c) nonlinear post-peak models

4.3.3. Bifurcation point

The numerical localization model based on the longitudinal strain method need to predict the bifurcation point which occurs after peak load and is needed to account for the

deformations occurring between the peak load and the bifurcation point. According to experimental observation and Bao et al. (2016), after the peak and as the member deforms, the engineering strain inside the localization zone increases in a faster pace and the increase of engineering strain outside the localization zone slows down till the bifurcation point as shown in Fig. 4.6. At bifurcation point, the change in the engineering strain outside the localization zone becomes zero and the region outside the localization zone starts to unload elastically. In other words, once the peak load is reached, the strain rate (the change in strain over time) inside the localization zone starts to increase while the strain rate outside the localization zone starts to decrease till the bifurcation point where the strain rate outside the localization zone becomes zero as shown in Fig. 4.7.

The experiments showed that the bifurcation point occurs approximately at a 1% drop in load ($P_{loc}=0.99*P_o$). Hence, the only missing parameter is displacement at the bifurcation point, u_{loc} , which is dependent on the length of the specimen.

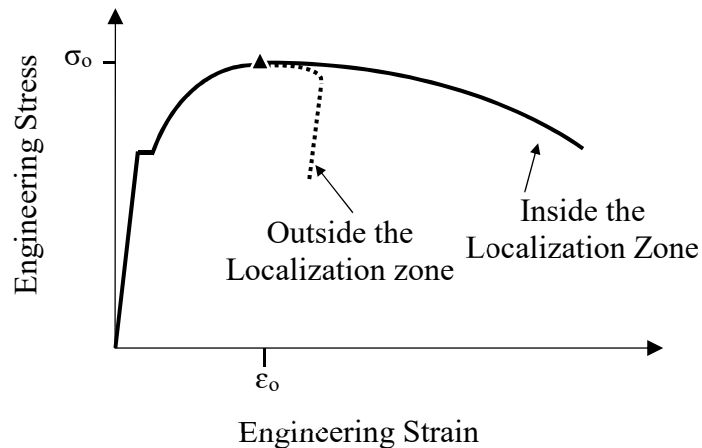


Fig. 4.6. Engineering stress-strain relationship inside and outside the localization zone

A mathematical expression to determine u_{loc} can be developed as follows. It is assumed that the material is isotropic, and the structural member consists of two regions A (inside the localization zone) and B (outside the localization zone) as shown in Fig. 4.3a. The change in total displacement of the member equals the summation of the change in displacements in both regions.

$$du = du_A + du_B \quad (4.12)$$

By dividing Equation 4.12 by (L_o*dt) in which L_o denotes the original specimen length and dt is change in time, Equation 4.12 becomes:

$$\dot{\epsilon} = \dot{\epsilon}_A \frac{L_A}{L} + \dot{\epsilon}_B \frac{L_B}{L} \quad (4.13)$$

In which $\dot{\epsilon}$ denotes the strain rate of the member which is assumed to be constant along the entire loading (monotonic loading). $\dot{\epsilon}_A$, $\dot{\epsilon}_B$ donate the strain rate inside and outside the localization zone, respectively. Because the strain rates inside both regions are assumed to be the same ($\dot{\epsilon}_A^0 = \dot{\epsilon}_B^0$) before reaching the peak load, they are equal to the strain rate of the member up to the peak load (see Fig. 4.7), as shown in Equation 4.13. After the peak load, the strain rate inside the localization zone increases dramatically following $\dot{\epsilon}_A(t)$ while it decreases outside the localization zone following $\dot{\epsilon}_B(t)$ until the bifurcation point ($t=t_{loc}$) at which the strain rate inside the localization zone becomes zero as shown in Fig. 4.7. At the bifurcation point, $\dot{\epsilon}_B(t = t_{loc}) = \dot{\epsilon}_B^{loc} = 0$ and $\dot{\epsilon}_A(t = t_{loc}) = \dot{\epsilon}_A^{loc}$ and Equation 4.13 becomes:

$$\dot{\epsilon}_A^{loc} = \dot{\epsilon} \frac{L}{L_A} \quad (4.14)$$

In Fig. 4.7, the area under strain rate curve equals the engineering strain. Therefore, the engineering strain inside the localization zone (i.e. region A) at the bifurcation point is as follows.

$$\varepsilon_A^{\text{loc}} = \varepsilon_o + \int_{t_o}^{t_{\text{loc}}} \dot{\varepsilon}_A(t) dt \quad (4.15)$$

For the sake of simplicity, it is assumed that the strain rate inside and outside the localization length is a linear function. So, Equation 4.15 becomes:

$$\varepsilon_A^{\text{loc}} = \varepsilon_o + \frac{1}{2} * (\dot{\varepsilon}_A^{\text{loc}} + \dot{\varepsilon}_A^o) * (t_{\text{loc}} - t_o) \quad (4.16)$$

The same for region B, hence

$$\varepsilon_B^{\text{loc}} = \varepsilon_o + \frac{1}{2} * \dot{\varepsilon}_B^o * (t_{\text{loc}} - t_o) \quad (4.17)$$

Substituting Equations 4.14 and 4.16 into 4.17 and $\dot{\varepsilon}_A^o = \dot{\varepsilon}_B^o = \dot{\varepsilon}$ yields:

$$\varepsilon_B^{\text{loc}} - \varepsilon_o = \frac{(\varepsilon_A^{\text{loc}} - \varepsilon_o)}{\left(\frac{L}{L_A} + 1\right)} \quad (4.18)$$

Recall, the displacement at the bifurcation point is:

$$u_{\text{loc}} = \varepsilon_A^{\text{loc}} * L_A + \varepsilon_B^{\text{loc}} * L_B \quad (4.19)$$

In other words, the displacement at the bifurcation point can also be presented in a different way.

$$u_{\text{loc}} = u_o + (\varepsilon_A^{\text{loc}} - \varepsilon_o) * L_A + (\varepsilon_B^{\text{loc}} - \varepsilon_o) * L_B \quad (4.20)$$

In which $\varepsilon_A^{\text{loc}}$ and $\varepsilon_B^{\text{loc}}$ denotes the engineering strain at the bifurcation point in region A and B, respectively.

After substituting Equations 4.18 into 4.20, it yields

$$u_{\text{loc}} = u_o + (\varepsilon_A^{\text{loc}} - \varepsilon_o) \left(1 + \frac{L_o - L_A}{L_o + L_A}\right) L_A \quad (4.21)$$

The experiments showed that $(\varepsilon_A^{\text{loc}} - \varepsilon_o)$ is constant for different length specimens and approximately equals 0.07 mm/mm. L_A is the localization length at the bifurcation point.

The displacement at the bifurcation point for four specimen lengths (3D, 6D, 12D and 24D) were determined using Equation 4.21 and compared with the experiments as

shown in Fig. 4.8. The results show that the displacement predicted using Equation 4.21 and 4.214.21 are consistent with the displacements measured in the experiments.

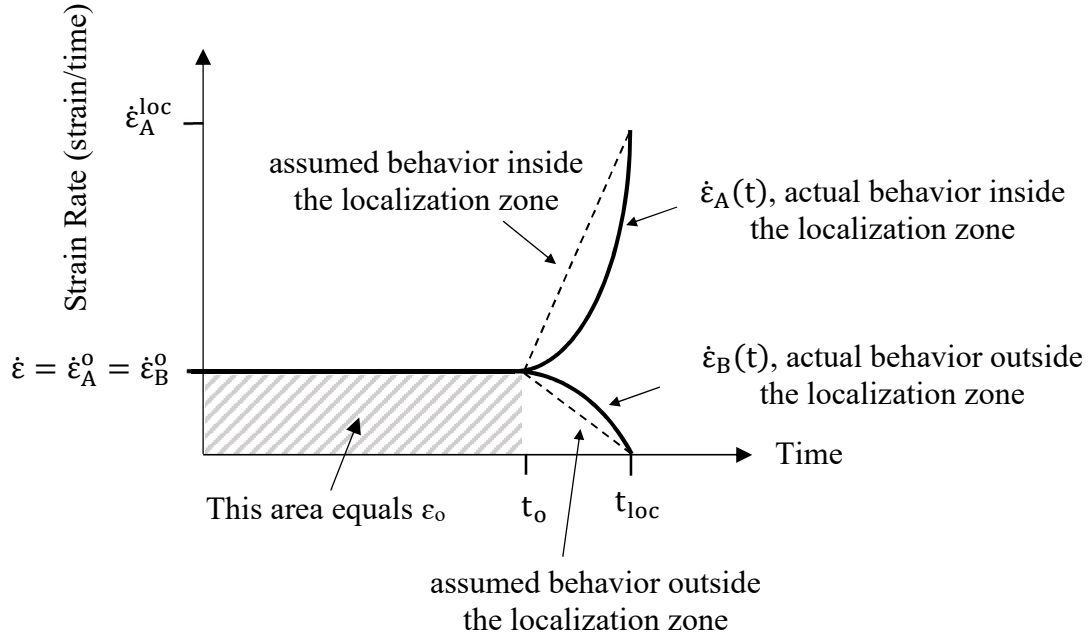


Fig. 4.7. Strain rate inside and outside the localization zone

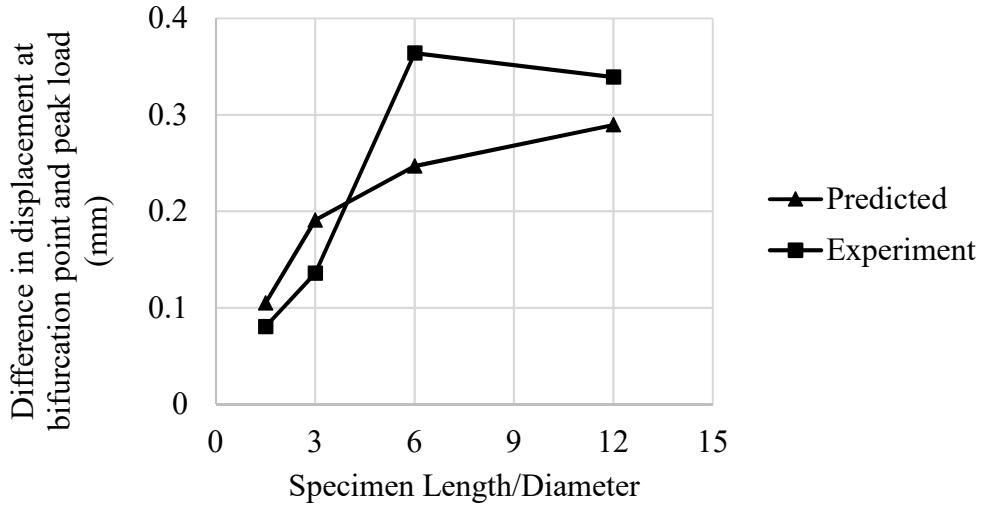


Fig. 4.8. Displacement between the peak load and the bifurcation vs specimen length

4.3.4. Linear Post-Peak Model

The linear post-peak model is based on the localization length from the average strain method because it starts at the peak load. A single post-peak stiffness (K_p) is used and applied immediately following the peak load (see Fig. 4.5a). The variables that control the linear post-peak stiffness are the localization length and softening factor determined by the average strain method listed in Table 4.1.

The localization length determined by the average strain method is proportional to the specimen length and evolves during the softening regime. The localization length calculated at the peak load and the rupture is 0.6 and 0.25 times the specimen length. When the specimen length becomes larger so does the localization length. A larger portion of the localization zone unloads which may not reflect the true behavior of the softening zone. Therefore, the localization length calculated at the rupture ($0.25 L_o$) is used.

The softening factor highly depends on the deformations occurring inside the localization length and its length. The softening factor for the localization length determined at the rupture is also size dependent and can be represented by the following empirical equation.

$$\beta = 0.00005 L_o/D + 0.0007 \quad (4.22)$$

By inserting the values for L_c and β into Equation 4.11, the following is obtained for the post-peak stiffness:

$$K_p = \frac{A_o E}{L_o} \left(\frac{L_o + 7}{L_o - 2500} \right) = f(L_o, A_o, E) \quad (4.23)$$

The numerical localization model developed in the previous section cannot predict the load at which the steel member fails even though it may efficiently predict the post-peak response. A failure criterion is developed to predict the rupture load through finding

the engineering strain inside the localization zone corresponding to the rupture load. For the average strain method, the engineering strain inside the localization zone at rupture load can be determined based on the following curve based on experimental data.

$$\epsilon_r = 0.8 e^{-0.04L_o/D} \quad (4.24)$$

The linear post-peak response of specimen 12D-1 was compared with the experiment as shown in the Fig. 4.9. It is shown that the linear post-peak response is missing most of the nonlinearity of the post-peak response. Furthermore, the displacement and load at the rupture are 10% less and 19% more than the experiment, respectively. The rupture load may not be predicted perfectly due to using constant values of both the localization length and softening factor throughout the post-peak response. Furthermore, once the engineering strain inside the localization zone at rupture presented in Equation 4.24 is reached, the member fails at a higher load (see Fig. 4.2a).

The main advantage of the linear post-peak model is that the linear post-peak model needs only one value of both the localization length and softening factor to determine the post-peak response of one-dimensional steel member under monotonic tension.

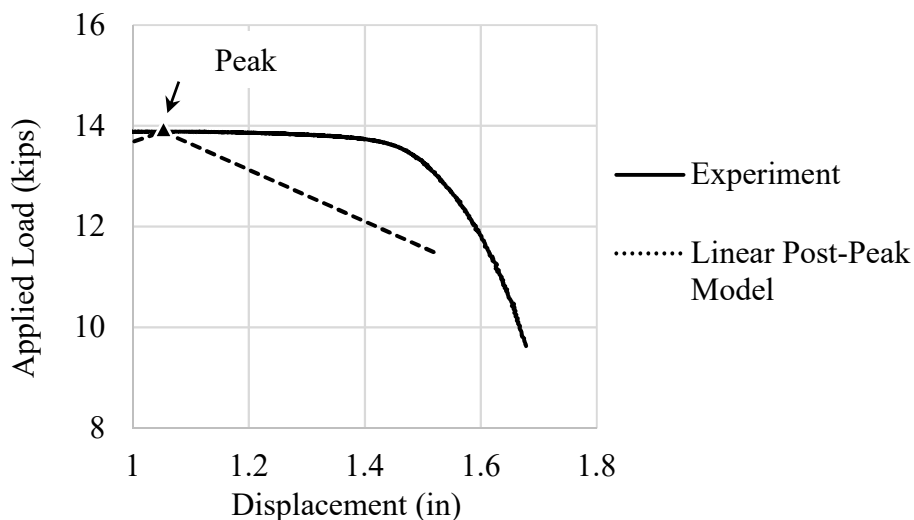


Fig. 4.9. Linear post-peak model of 12D-1 specimen

4.3.1. Bilinear Post-Peak Model

The bilinear post-peak model is a refined localization model and based on longitudinal strain method. Bilinear post-peak stiffness is applied as a two post-peak softening linear relationships (see Fig. 4.5b). The displacement at the bifurcation point (assumed to be at 1% drop in load) can be determined by Equation 4.21. While, the second post-peak stiffness, K_p , is applied immediately after the bifurcation point and can be calculated by the localization length and softening factor determined by the longitudinal strain method at the bifurcation point listed in Table 4.1.

The localization length is approximately five times the diameter at the bifurcation point and evolves during the softening regime till rupture, at which the localization length becomes 0.6 times the diameter. The softening factor is approximately 0.005 for the localization zone determined at the bifurcation point. Inserting these values of L_c and β into Equation 4.11 yields a post-peak stiffness:

$$K_p = \frac{A_o E}{L_o} \frac{1}{1-500/L_o} = f(L_o, D, A_o, E) \quad (4.25)$$

A failure criterion is based on the average of the engineering strain inside the localization zone defined at bifurcation. In the experiments, this strain was nearly constant for the four different specimen lengths, 0.354 mm/mm.

The bilinear post-peak response of specimen 12D-1 was compared with the experiment as shown in the Fig. 4.10. The results shown in Fig. 4.10 show that the bilinear post-peak model is better than the linear post-peak model of capturing the post-peak response of one-dimensional steel member under tension. The displacement and load determined by the bilinear post-peak model at the rupture compared to the experiment result are -2% and 1%, respectively. The main advantage of the bilinear post-peak model

over the linear post-peak model is that the second line relationship of the bilinear post-peak model is size independent and can be determined by one value of the localization length and softening factor. The bifurcation point still depends on the specimen length, but can be calculated using Equation 4.21.

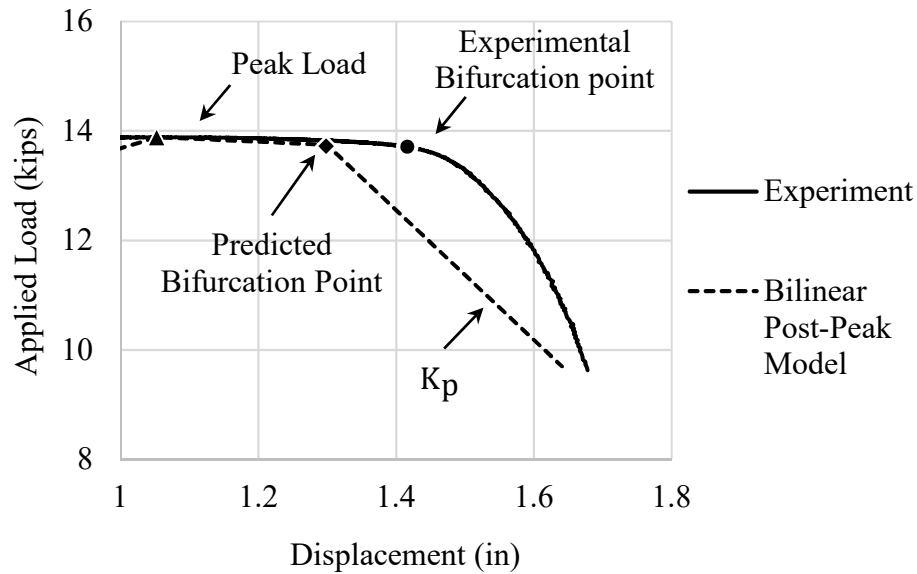


Fig. 4.10. Bilinear post-peak model of 12D-1 specimen

4.3.1. Nonlinear Post-Peak Model

The nonlinear post-peak stiffness $K_p(u)$ shown in Fig. 4.5c has one advantage over the bilinear post-peak stiffnesses because most of the nonlinearity of the post-peak response can be captured. The average strain method and the longitudinal strain method can both be modified to serve as a nonlinear post-peak stiffness. However, as the longitudinal strain method showed better correlation with experimental results it is the only one presented. The nonlinear post-peak model consists of a linear relationship up until

bifurcation and then a nonlinear stiffness, $K_p(u)$. The relationship before bifurcation is the same as in the bilinear model. After bifurcation, the nonlinear post-peak stiffness $K_p(u)$ can be determined by the length of the member, instantaneous localization length, $L_{c,i}$, where i refers to a loading instant ($i=1$ when $u=u_{loc}$ and $P=P_{loc}=0.99P_o$, while $i=n$ at the rupture) and the softening factor, β . The equation for the non-linear relationship between the instantaneous localization length ($L_{c,i}$) and the instantaneous engineering strain ($\epsilon_{x,i}$) is based on the experimental results as presented in Equation 3.2.

$$L_{c,i} = 5D e^{-2.8 \left(\frac{\epsilon_{x,i} - \epsilon_{loc}}{\epsilon_r - \epsilon_{loc}} \right)} \quad L_o \geq 6D \quad (3.2)$$

The nonlinear branch of the nonlinear post-peak model can be calculated by determining the $K_{p,i}$ at one displacement (u_i) and $K_{p,i+1}$ at the next displacement (u_{i+1}) where $u_{i+1} = u_i + \Delta u$. $K_{p,i}$ can be determined by using the Equation 4.11 and applying the values of $L_{c,i}$ from Equation 3.2 at strain i (i.e. $\epsilon_{x,i}$) and the softening factor. The softening factor is approximately 0.001.

The average of the engineering strain of four tested specimens inside the localization zone at rupture was approximately 0.91 mm/mm. This is larger than the strain used in the bilinear method because the localization zone length is smaller.

The nonlinear post-peak response of specimen 12D-1 shown in Fig. 4.11 was calculated using $\Delta u = 0.5$ mm. The nonlinear post-peak model showed better results than the other models and can capture most of the softening nonlinearity. The nonlinear post-peak model fails at load 3% lower than the experiment at a displacement 2% less.

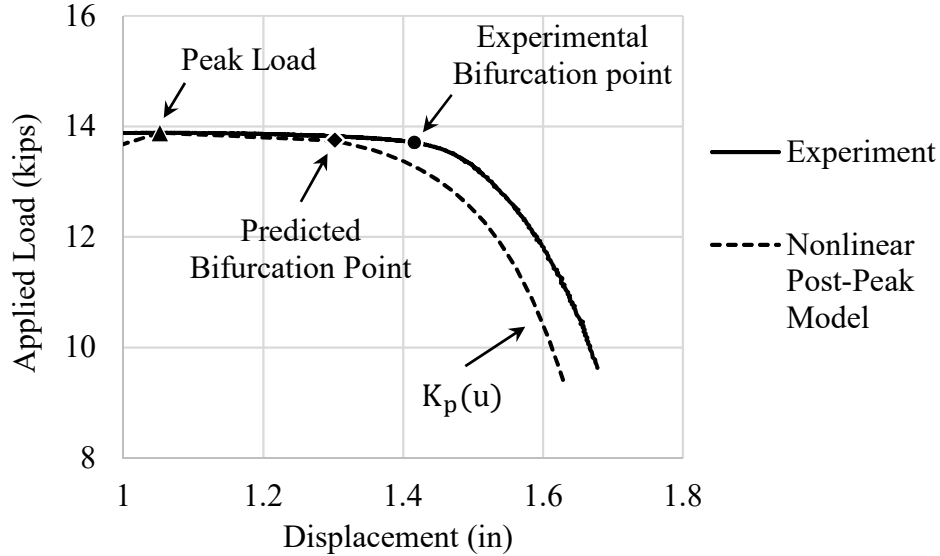


Fig. 4.11. Nonlinear post-peak model of 12D-1 specimen

4.3.1. Comparison of Numerical Post-Peak Models with Experiments

The localization models were used to predict the response of four steel specimens of different lengths (3D, 6D, 12D and 24D) and compared to the experiments as shown in Fig. 4.12. All three models are capable of simulating the softening behavior of steel bars under tension. The linear post-peak numerical localization model is much simpler than the other two methods because it needs only one stiffness. However, it depends on the scale length for determining the localization length and the softening factor. It also showed greater error for longer specimens (see Fig. 4.12). Furthermore, the displacement at rupture load is underestimated by an absolute average of all specimens of approximately 10% (see Table 4.3) while the absolute average rupture load is around 16% greater than the experimental rupture load (see Table 4.4).

The bilinear post-peak numerical localization model results shown in Fig. 4.12 show a better agreement than the linear post-peak model because two post-peak stiffnesses

are used to simulate the softening response. The bifurcation point displacement (u_{loc}) depends on the specimen length but the localization length and the softening factor that determine the second post-peak stiffness are length independent parameters. It predicts the displacement at rupture load within an absolute average of 6% greater than the experiments. Furthermore, the absolute average of predicted rupture load of all specimens is around 7% (see Table 4.4).

The nonlinear post-peak numerical localization model represents a modification of the bilinear post-peak model. It can accurately simulate the softening response better than the earlier two models as shown in Fig. 4.12. However, it depends on the engineering strain at the bifurcation point and the engineering strain at the rupture load to accurately determine the instantaneous localization length used to determine the $K_{p,i}$. It predicts the displacement at rupture load within an absolute average of 9% greater than the experiments. Furthermore, the absolute average of predicted rupture load of all specimens is around 3%.

In general, the numerical localization models can efficiently predict the overall softening response of one-dimensional steel member under tension with a maximum error less than 15% comparing to the experiments.

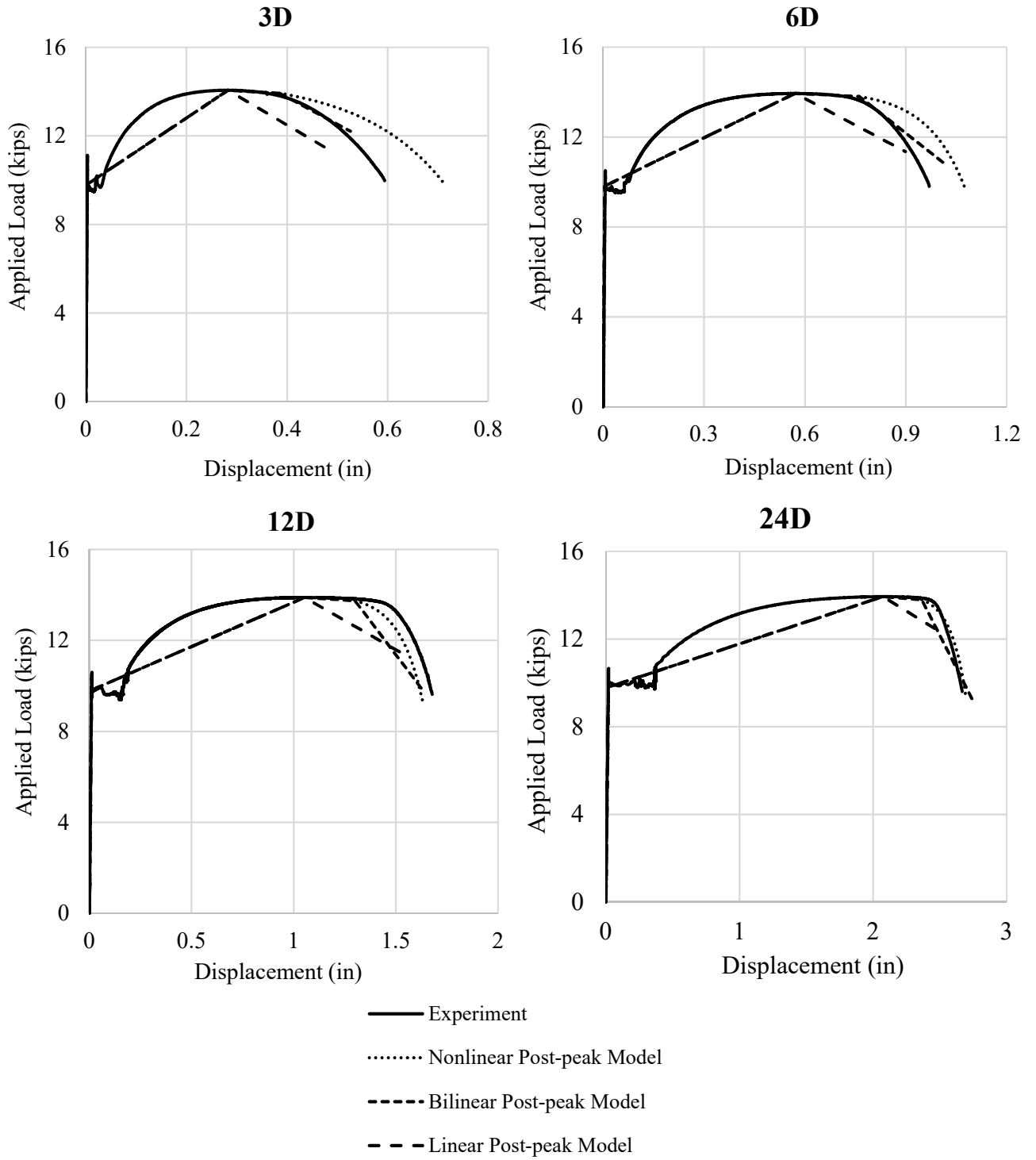


Fig. 4.12. Comparison the load-displacement of experiments and linear, bilinear and nonlinear post-peak numerical localization models

Table 4.3. Experimental and numerical displacement at rupture load (in)

Specimen ID	Experiment	Numerical Model			Difference %		
		Linear	Bilinear	Nonlinear	Linear	Bilinear	Nonlinear
3D-1	0.594	0.478	0.526	0.715	-20%	-11%	20%
6D-3	0.969	0.900	1.012	1.079	-7%	4%	11%
12D-1	1.677	1.530	1.641	1.630	-9%	-2%	-3%
24D-2	2.665	2.473	2.749	2.697	-7%	3%	1%

Table 4.4. Experimental and numerical rupture load (kips)

Specimen ID	Experiment	Numerical Model			Difference %		
		Linear	Bilinear	Nonlinear	Linear	Bilinear	Nonlinear
3D-1	9.982	11.450	12.210	9.767	15%	22%	-2%
6D-3	9.802	11.352	10.849	9.623	16%	11%	-2%
12D-1	9.622	11.437	9.698	9.330	19%	1%	-3%
24D-2	9.599	12.444	9.175	9.262	30%	-4%	-4%

4.4. Finite Element Analysis (FEA)

Finite element analysis is a powerful tool used in the simulation of structural materials. It can be used to simulate the post-peak response of cylindrical steel bars in tension but suffers from mesh sensitivity and accurate material properties (such as strain rate hardening). FEA was used to simulate the specimens described in the previous tests. The results of the FEA analysis are compared to the experimental results to highlight the difficulty and possible inaccuracies of FEA in post-peak response simulation.

4.4.1. Modeling

In all FEA simulations, rate-independent plasticity is used. A Von Mises yield criterion with calibrated multilinear isotropic hardening and associative flow rule is chosen. The true stress strain curve derived from the experimental data is used in the simulation. The true strain is directly determined from the 3D DIC, or it can be calculated from the longitudinal engineering strain using the Equation 4.26. While the true stress is determined by dividing the applied force by the current cross-sectional area, A , which can be calculated by Equation 4.27.

$$\epsilon_{xx}^{\text{true}} = \ln(1 + \epsilon_{xx}^{\text{eng}}) \quad (4.26)$$

$$A = A_0(1 - |\epsilon_{yy}^{\text{eng}}|)^2 \quad (4.27)$$

During the first stage of loading, the simulated specimen experiences elastic deformations along the entire length. Once the yield stress is reached, the simulated specimen undergoes plastic deformations according to the true stress-strain data. In order to simulate the necking which is a reduction in the cross-sectional area of the simulated specimen, large deflection option is activated. This option takes into account the change in geometry due to straining. The four specimens 3D, 6D, 12D and 24D are simulated. All simulated specimens are subjected to monotonic displacement. Because a failure criterion is not defined in the developed FEA model, the maximum longitudinal engineering strain at the fracture location is set to be 1.4 in/in which is the same value from the experiments. The displacement at x-axis along the reduced section and the applied load are determined. In following sections, material properties and meshing are explained.

4.4.2. Geometrical and Material Properties

Due to loading, material and geometrical symmetry, one eighth of the steel specimens was simulated. Fig. 4.13 shows the geometry of specimen 3D. The three faces of the simulated specimen are symmetric to the normal axis that is perpendicular to face plane. The simulated support is fixed in y and z directions but deformed in negative x to produce tension force. All the simulated specimens have the dimensions shown in the Fig. 4.13 except the length. However, the diameter of 24D specimen is reduced by 0.001 in. because the 24D specimen reaches greater displacement at peak load than the experiment when the diameter is 0.5 in. while the diameter at the end of reduced section remains 0.5 in. Pivot Edge which is an ANSYS option was used to create this diameter reduction.

Accurate material properties are crucial accurate FEA simulations. Table 4.5 shows the material properties used for all FEA simulations. A true plastic stress-strain (Cauchy stress and true plastic strain) data was provided. The curve is determined from the experimental data starting at the yield point. The experimental true plastic stress-strain data may lead to inaccurate results because it is determined at the surface of the specimen while FEA is a 3D simulation. However, these data can be calibrated. Calibrating the true plastic stress-strain data is the only factor that may lead to matching the experimental load-displacement curve to the one obtained from FEA. Fig. 4.14 shows the experimental and calibrated true plastic stress-strain data.

Calibration is needed because FEA model is an isotropic modelling while the experiments is not. Calibrated (modified) multilinear isotropic hardening of true plastic stress-strain can be obtained through matching the experimental load-displacement curve to the one obtained from FEA as proposed by (Joun et al. 2007; Joun et al. 2008). After the

experimental load-displacement curve of 3D specimen is matched with FEA results, the calibrated true plastic stress-strain from 3D specimen simulation shown in Fig. 4.14 is used in all other simulations. The calibrated true plastic stress-strain is calculated at the center of the simulated specimen not at the surface.

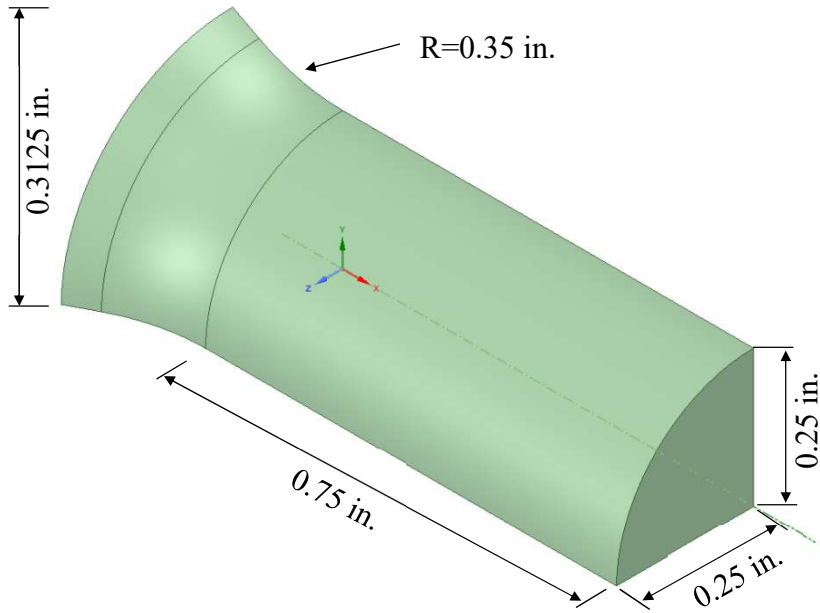


Fig. 4.13. Geometry and meshing of one eighth of 3D specimen

Table 4.5. Material properties used in simulation

Young's modulus (ksi)	Poisson's ratio	Tensile Yield strength (ksi)
30,000	0.3	50

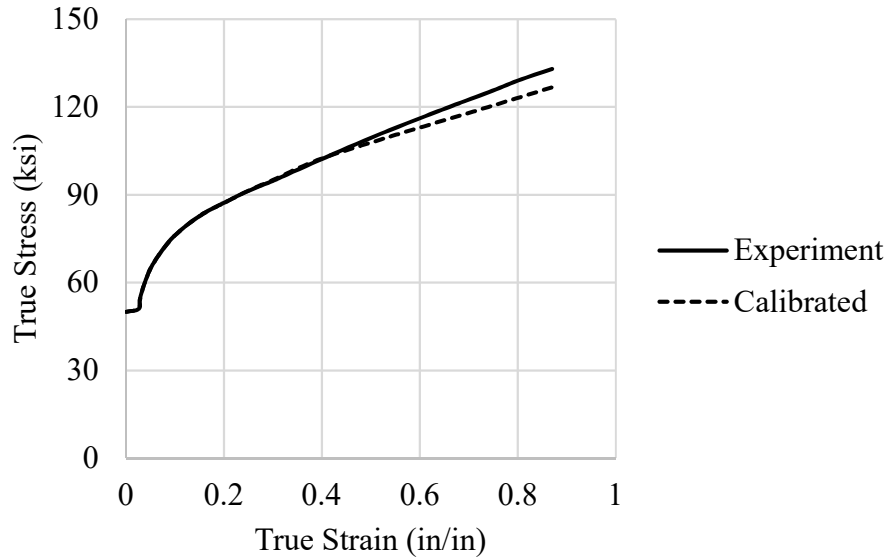


Fig. 4.14. Experimental and calibrated true Stress-Strain

4.4.3. Meshing

A mesh sensitivity study of three different mesh sizes was performed. Table 4.6 shows the mesh sizes and the displacement at rupture load for every solution number. The load versus displacement of every mesh size is plotted in Fig. 4.15. The pre-peak behavior is approximately identical for all mesh sizes. However, Fig. 4.15 shows that with larger mesh size, the post-peak response is quite different because the mesh sensitivity. To study this kind of behavior, the longitudinal engineering strain along the member is plotted in Fig. 4.16. With larger mesh size, the longitudinal engineering strain tends to distribute along larger region causing shallow post-peak response. While with small mesh size, the longitudinal engineering strain localizes into relatively small region which makes the post-peak steep.

A growing meshing technique is used to reduce the processing time with accurate results. The Hex Dominant method is used to create solid elements. The mesh size of the

center of the specimen is 0.015 in. to ensure most of the geometrical nonlinearity of the necking can be captured and make the localized necking to occur at the center of the specimen (see Fig. 4.17). The growth rate of mesh size is set to 1.05. All elements are quadratic and has twenty points of integration. Fig. 4.17 shows the mesh of simulated 6D specimen.

Table 4.6. Convergence Study

Solution Number	Mesh Size (in.)	Displacement at Rupture Load (in.)	Difference with Experiment (%)
1	0.25	0.690	16%
2	0.125	0.575	-3%
3	0.05	0.539	-9%

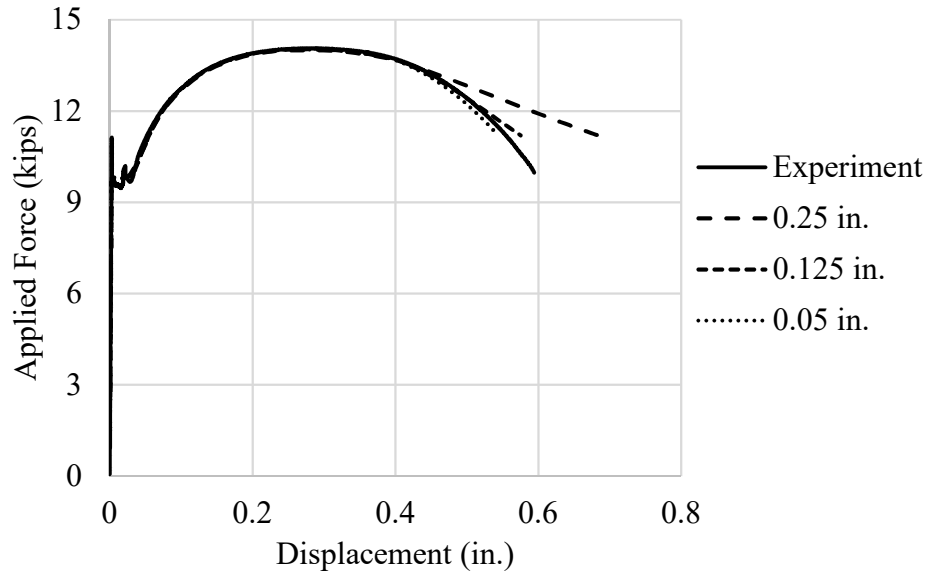


Fig. 4.15. Load displacement of FEA results of different mesh size

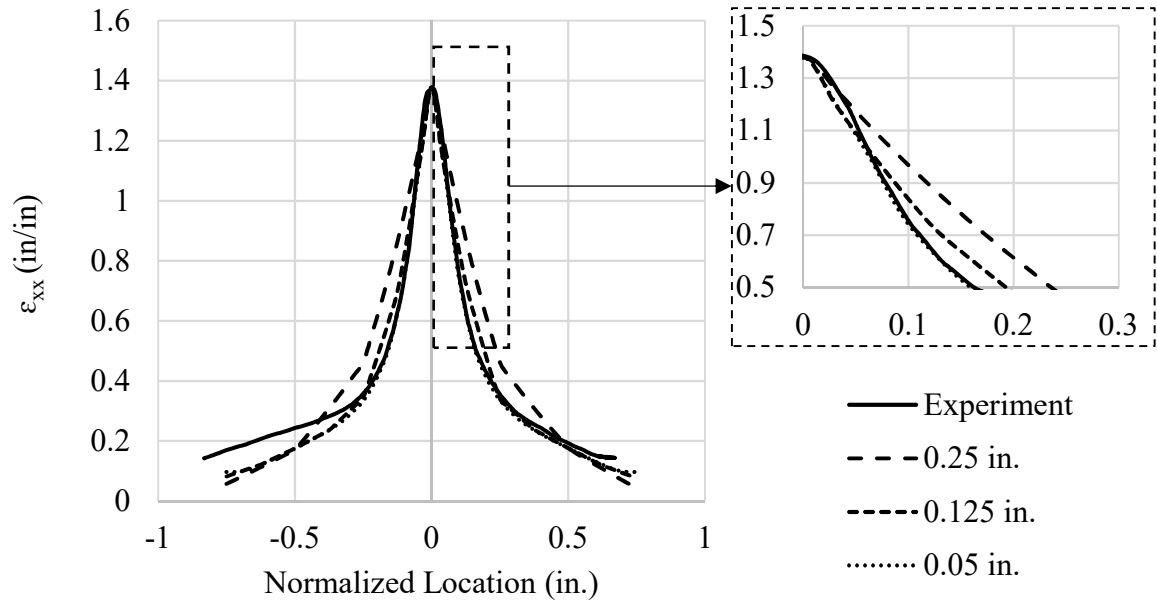


Fig. 4.16. Longitudinal engineering strain profile of 3D specimen with different mesh sizes at rupture load

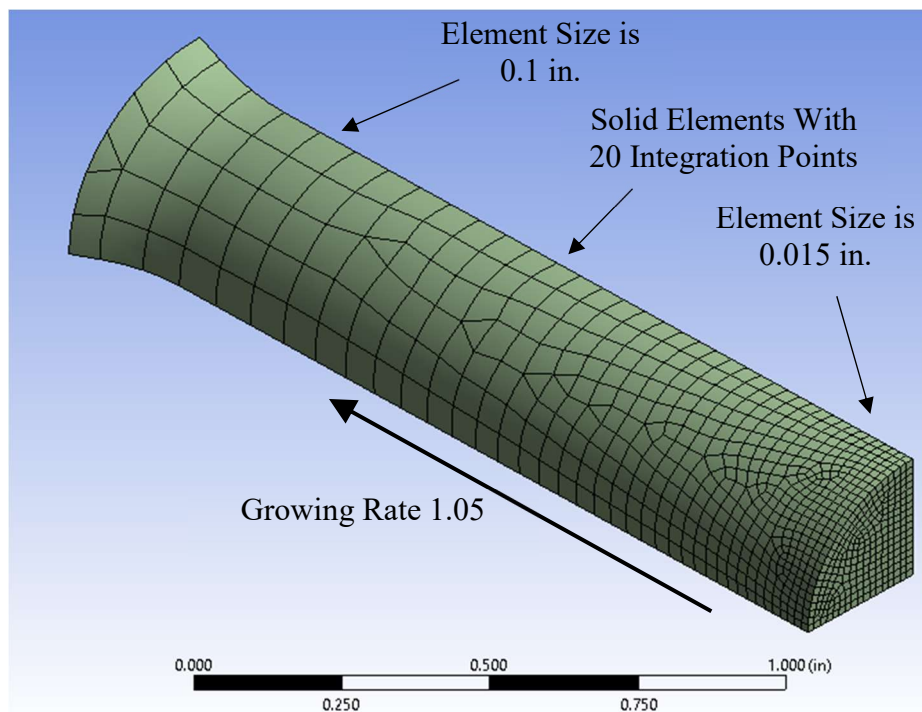


Fig. 4.17. Meshing of one eighth of 6D specimen

4.4.4. Results

The difference in applied load at the peak load between the experiments and the FEA simulations is less than 1%. However, the rupture load FEA simulations is around 15% more than the experimental rupture load because the FEA simulated localized necking occurs at the peak load not at the bifurcation point which is what the experiments showed. The displacement at peak and rupture loads from simulations does not perfectly match the experimental data. Table 4.7 shows the experimental and simulated displacements at the peak and rupture loads for all specimens. It is shown that the maximum percent of difference in displacement at the peak load is approximately around 7% while the maximum percent of difference in displacement at the rupture load is around 15%.

The explanation of mismatching between the FEA simulations and experiments are presented in the following sections.

Table 4.7. Experimental and FEA displacements at peak and rupture loads

Specimen ID	Displacement at Peak Load (in)			Displacement at Rupture Load (in)		
	Experiment	FEA	Difference %	Experiment	FEA	Difference %
3D	0.283	0.260	-5%	0.594	0.549	-8%
6D	0.571	0.531	-7%	0.970	0.8626	-11%
12D	1.052	1.091	4%	1.678	1.426	-15%
24D	2.075	2.123	2%	2.667	2.422	-9%

4.4.5. Comparison the FEA Model with The Experiments

The displacement at x-axis along the reduced section versus the applied load for all FEA simulations is compared with experimental data as shown in Fig. 4.18. It is shown that the experimental load-displacement of 3D specimen is approximately identical to the simulated one except the rupture load which is 13% more than the experiment. This is done to determine the true plastic stress-strain data. However, for the other specimens, it is difficult for the FEA to capture the increase in strain along the specimen length after the peak load. Because, in FEA, the necking occurs at the peak load while the experiments showed that the necking occurs after the peak load at the bifurcation point (approximately after a 1% drop in load).

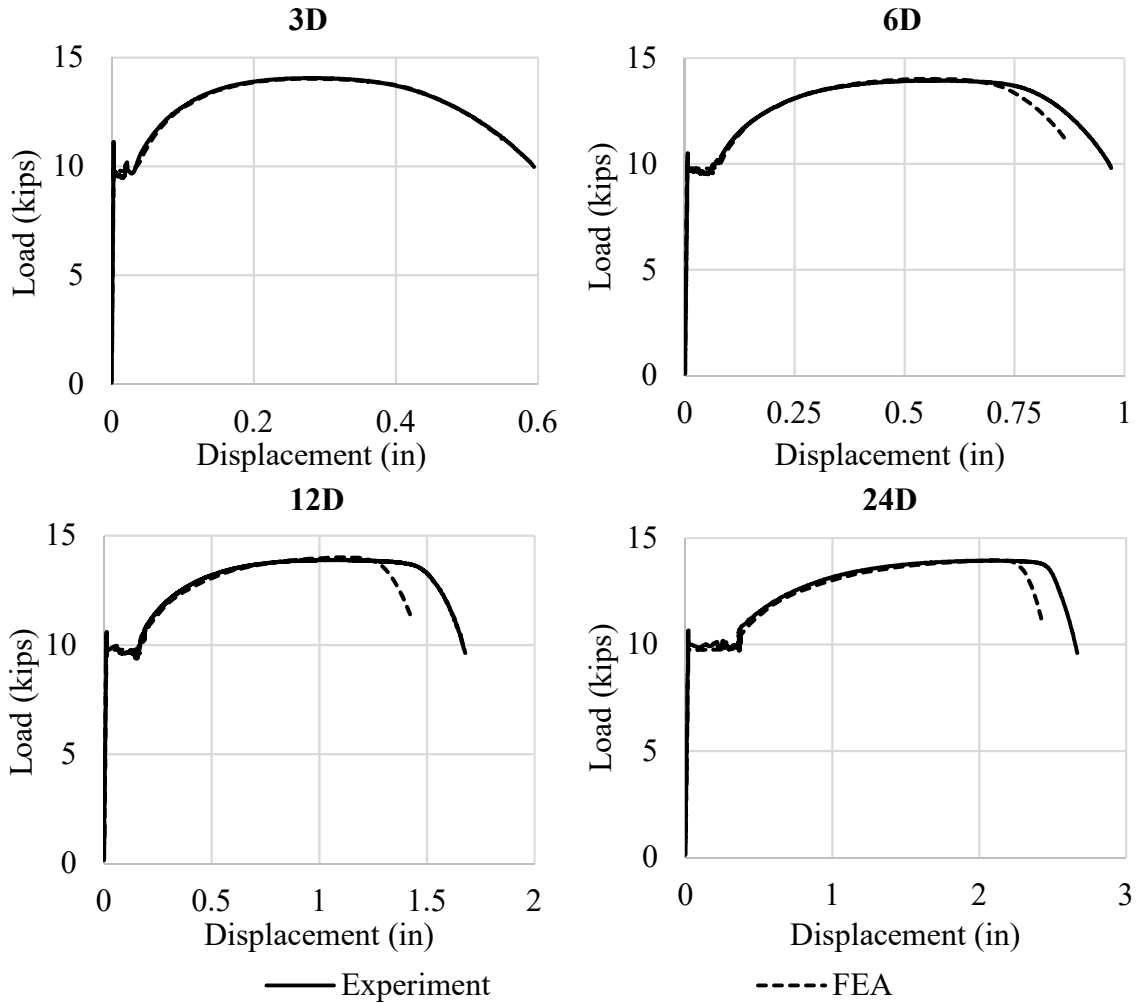


Fig. 4.18. Load displacement of experiments and FEA results

Modifying the material constitutive modeling through matching the experimental load-displacement curve to the one obtained from FEA leads to differences in internal plastic strain (i.e. longitudinal engineering strain profile) because load-displacement curves are a result of material constitutive modeling as well as the interaction of the material constitutive with the geometric nonlinearity due to necking (Cooke and Kanvinde 2015). At the peak load, experimental longitudinal engineering strain profile and the simulated one shown in Fig. 4.19 are almost the same. At the bifurcation point, however,

experimental and simulated longitudinal engineering strain profiles are different. The simulated specimen unloads elastically at the peak load and the plastic strain increases only inside the localization zone while the experiments showed that the plastic strain continues to increase throughout the specimen length until the onset of the localization at the bifurcation point. The average percentage of difference between the maximum experimental and simulated longitudinal engineering strain at the bifurcation point is around 33%. This error percentage increases to be around 50% at the rupture load (see Fig. 4.20).

Cooke and Kanvinde (2015) showed that simulating extreme limit states in steel, such as localization, requires calibration of numerous parameters. Calibration is often achieved by matching experimental load–displacement curves to those calculated by FEA simulations. Cooke and Kanvinde (2015) also showed that this method of matching is extremely susceptible to nonunique fitting. The prediction of peak force is not considerably affected by this non-uniqueness. However, the prediction of internal plastic strains is highly influenced by non-uniqueness, with errors as large as 50% with respect to the true material as found in the FEA simulations in their study.

One of the difficulties in FEA analysis is that the necking in FEA occurs due to the reduction in cross sectional area under large deformation only because of material softening. In other words, the necking behavior is a structural bifurcation instability rather than a material instability (Okazawa, 2010). Okazawa (2010) showed that the peak load can happen with a uniformly deformed state which is not a material softening and this instability comes from cross-sectional transformation. Even though the peak point can be evaluated by calculating the determinant of the tangent stiffness of the material level before

assembly, Okazawa (2010) showed that the material instability theory never explains the occurrence of necking immediately after the peak load.

The difference in experimental and simulated total internal plastic strain after the peak load shown in Fig. 4.19 shows that even though total displacement may be matched, a completely different longitudinal engineering strain profile may be present. The difference in the FEA longitudinal engineering strain profile as shown in Fig. 4.20 makes it difficult to use FEA simulations as a basis for determining localization behavior and as such presents the need for the experimental results in this study. Fig. 4.21 shows the experimental and simulated specimen before rupture.

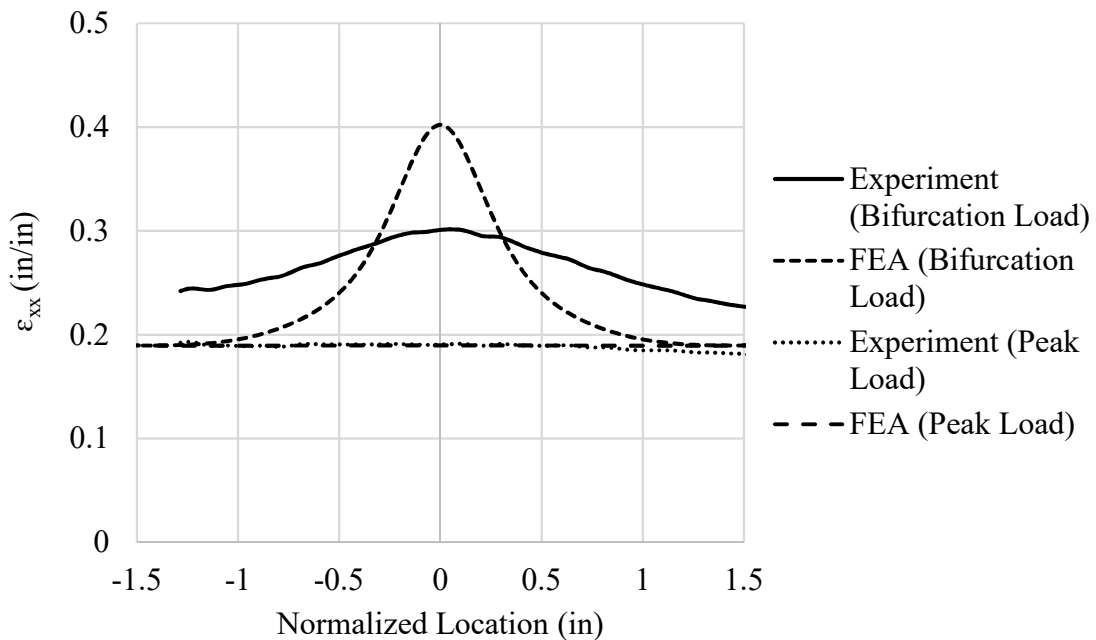


Fig. 4.19. Longitudinal engineering strain profile of 12D specimen.

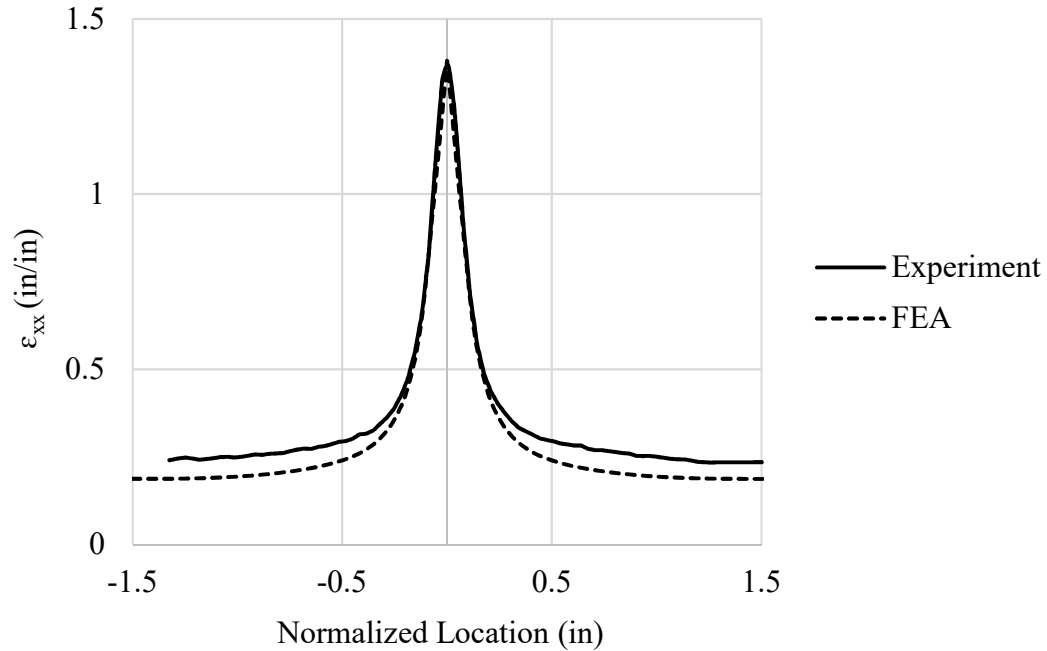


Fig. 4.20. Experimental and FEA longitudinal engineering strain profile of 3D specimen

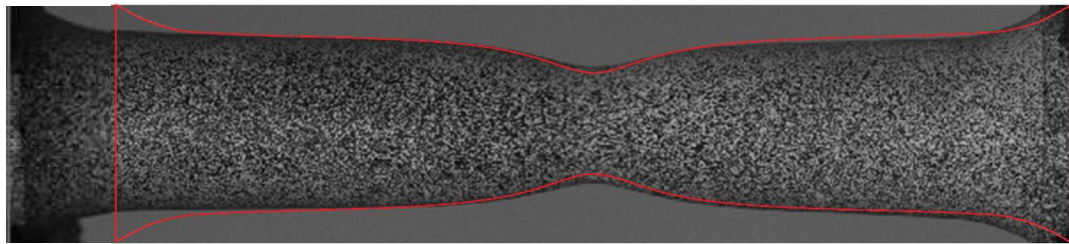


Fig. 4.21. Specimen before rupture, red line represents FEA simulation

4.5. Summary and Conclusions

A numerical localization model, based on the experimental data, is developed to simulate the post-peak response of a one-dimensional steel member subjected to monotonic tension. The numerical localization model defines the pre- and post-peak stiffnesses of the line element. The post-peak stiffness is derived by assuming that the member consists of two regions, localization zone and outside the localization zone. At the onset of strain localization, the deformations inside the localization zone increase and follow the softening region of the constitutive relationship while outside the localization zone unloads

elastically. Linear, bilinear, and nonlinear softening regions of the constitutive relationship are assumed. As a result, three post-peak models (linear, bilinear and nonlinear) are developed. The linear localization model consists of one linear post-peak stiffness. The results show reasonable agreement with the experimental data. The linear post-peak model is simpler than the other two post-peak models. However, it depends on the length scale for determining the localization length and the softening factor. The bilinear localization model has two post-peak stiffnesses and show a better agreement than the linear post-peak model because two post-peak stiffnesses are used to simulate the softening response. The bifurcation point displacement (u_{loc}) depends on the specimen length but the localization length and the softening factor that determine the second post-peak stiffness are length independent parameters. The nonlinear post-peak model represents a modification of the bilinear post-peak model. The nonlinear post-peak model is capable of simulating the post-peak nonlinearity response through determining the evolution of the localization length during the softening process.

The load-displacement curves of the three models are compared with the experimental data. The absolute average of differences in displacement at the rupture load between linear, bilinear and nonlinear post-peak models and experiments were 11%, 5% and 9%, respectively, but the nonlinear post-peak model can predict the rupture load within 1% for the 24D specimen. While the differences in rupture load between linear post-peak model and bilinear and nonlinear post-peak models and experiments were 17%, 9% and -3%, respectively.

All the tested specimens are simulated by FEA and compared to experimental results. The difference in applied load at the peak and rupture load between FEA

simulations and experiments is less than 1%. However, displacement at peak and rupture loads is as much as 12%. This is because the FEA simulates localization at the peak load however in the experiments the localization occurs beyond the peak load. Even though the FEA is a powerful tool to simulate the extreme limit state such as localized necking, it has disadvantages. Some of these disadvantages are: (1) Differences in internal plastic strain than experiment. The percentage of difference between the maximum experimental and simulated longitudinal engineering strain at the bifurcation is around 33%. This error percentage increases to be around 50% at the rupture load. (2) Localized necking occurs at the peak load not at the bifurcation. The FEA model which uses an isotropic strain hardening law causes the localized necking to occur at the peak load not at the bifurcation point as in the experiments.

CHAPTER FIVE

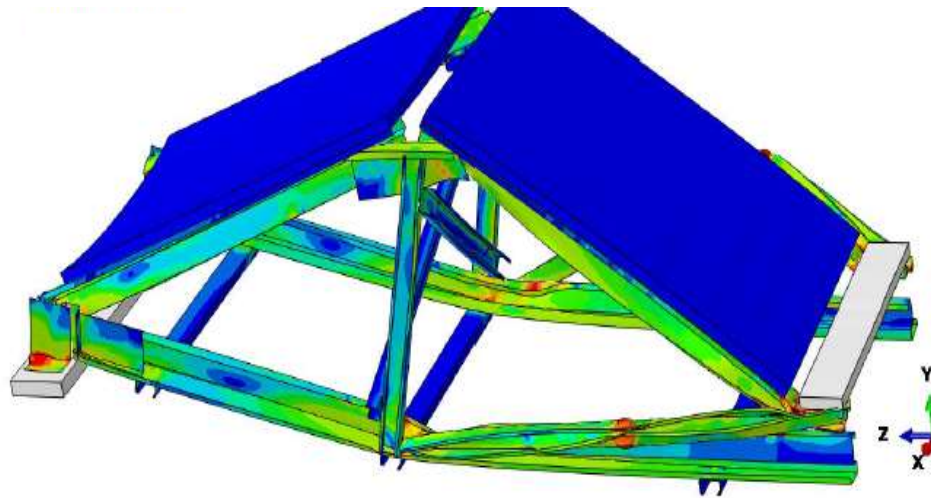
CHAPTER 5: INFLUENCE OF THE POST-PEAK BEHAVIOR ON COLLAPSE OF STRUCTURAL SYSTEMS

5.1. Introduction

Consideration of the post-peak behavior is especially important in understanding the redistribution of load from one member to another and how that proceeds to possible structural collapse. For example, consider the truss analysis and testing shown in Fig. 5.1. The FEA analysis shows symmetric failure and almost purely vertical displacement, while in testing, one member buckled before the other causing significant rotation and lateral displacement (Bondok 2017). Although, this research only considers tension behavior, the example illustrates that non-uniform failure can lead to significant rotations and lateral movements.

In order to investigate this behavior, two simple structural systems were analyzed analytically, and one system tested experimentally. Analytically, two different trusses (3 bars in parallel and a V shaped truss) were studied by applying the numerical model of the post-peak stiffness developed in the previous chapter. The effect of different initial imperfections on the overall structural response were considered. Experimentally, three test sets of three cylindrical steel bars in were loaded in parallel to study the effect of load redistribution. A 3D DIC measurement system was used to determine the deformations and strains along each bar. The influence of localization behavior in one bar on the load redistribution in the other bars is analyzed.

Finite Element Analysis Simulation



Experimental Test



Fig. 5.1. Example rotation in structural system due to unsymmetrical failure (Bondok 2017)

5.2. Analytical Study

To efficiently simulate the structural collapse and how the load redistributes, a one-dimensional localization model that is capable of simulating the post-peak behavior of one-dimensional steel members subjected to monotonic loading is needed. The numerical

model developed the previous chapter is a forward step toward understanding structural collapse through studying the load redistribution (Altai et al. 2019).

As a simple example, V-truss and tension members in parallel are studied using three numerical models (bilinear post-peak, modified Ramberg Osgood pre-peak with bilinear post-peak and nonlinear curve fitting) for numerical simulation of a one-dimensional member. Furthermore, the effect of 0.001%, 0.01%, 0.1%, 1% and 2.5% initial imperfections on the post-peak response are studied. Eighteen simulations are studied in total.

5.2.1. Analytical Models

Three analytical models (bilinear post-peak, modified Ramberg Osgood pre-peak with bilinear post-peak and nonlinear curve fitting) are used to perform numerical simulations of two-dimensional truss through studying the influence of initial imperfection on the post-peak response (Altai et al. 2019). For the sake of simplicity, only two cases are considered. Perfect case is when all members undergo softening till failure occurs. While imperfect case is when only one member has initial imperfection that causes the member to yield before other members and experiences softening while the rest of the system unload elastically.

To accurately predict the overall post-peak behavior of steel system, both pre- and post-peak response should be simulated accurately. For example, in case of imperfect system and when the peak load is reached, the imperfect member experiences softening while the other members start to unload elastically but the displacement at which they start to unload should be predicted accurately.

5.2.1.1. Bilinear Post-peak Model

Bilinear pre-peak and bilinear post-peak relationship represents four stages of loading during which the steel member experiences different behaviors. Four linear stiffnesses that are used to calculate the load displacement relationship of a steel member then can be used to predict the post-peak of a truss system. Linear elastic stiffness derived in Equation 4.5 simulates the elastic deformations of a steel member based on the modulus of elasticity. While based on the modulus of hardening, hardening stiffness derived in Equation 4.6 can be used to simulate the hardening response. The elastic and hardening stiffnesses are used to calculate the pre-peak response of a steel member. After the peak load, where the third stage starts, the longitudinal engineering strain along the steel member keeps increasing until the onset of localization when the final stage starts. Bilinear post-peak model explained in the section 4.3.1 is used to simulate the post-peak response. Equation 4.21 can predict the deformation at the bifurcation point. K_p can be determined based on the localization length and the softening factor which are $5D$ (i.e. 2.5 in.) and 0.005, respectively. The Equations mentioned in this section are listed below.

$$K = \frac{A_o E}{L} \quad P < P_y \quad \Delta P > 0 \quad (4.5)$$

$$K_h = \frac{A_o E_h}{L} \quad P_y \leq P \leq P_o \quad \Delta P > 0 \quad (4.6)$$

$$u_{loc} = u_o + (\epsilon_A^{loc} - \epsilon_o) \left(1 + \frac{L_o - L_A}{L_o + L_A} \right) L_A \quad P = 0.99P_o \quad \Delta P < 0 \quad (4.21)$$

$$K_p = \frac{A_o E}{L_o} \frac{1}{1 - 500D/L_o} \quad P < 0.99P_o \quad \Delta P < 0 \quad (4.25)$$

5.2.1.2. Modified Ramberg and Osgood Relationship

This relationship is similar to the bilinear post-peak model, except the pre-peak response is simulated by a nonlinear engineering stress strain curve that fits the Ramberg and Osgood (1943) expression.

$$\varepsilon = \frac{\sigma}{E} + 0.002\left(\frac{\sigma}{\sigma_y}\right)^n \quad (5.1)$$

Where ε and σ are the engineering strain and engineering stress respectively. n , E and σ_y are material constants which are $n=12.662$, $E=3*10^7$ psi and $\sigma_y=50000$ psi. The same bilinear post-peak stiffness explained in the section 4.2.5 (listed in the previous section) are used to simulate the post-peak behavior.

5.2.1.3. Nonlinear Curve Fitting

In this model, a four-parameter regression Equation shown below was used to fit the experimental load displacement curve of 6D and 24D specimens. For the best fitting results, the data from the yield to peak load (hardening) and the data from the peak load to failure (softening) were fitted separately. All the fitting parameters are shown in Table 5.1.

$$\sigma = a\sigma_1 + \frac{\sigma_2 - a\sigma_1}{1 + \left(\frac{\varepsilon}{b}\right)^n} \quad (5.2)$$

Table 5.1. Nonlinear curve fitting parameters

Parameter	Hardening	Softening	
Specimen length	6D and 24D	6D	24D
a	1.0175	0.306	0.785
b	0.05	0.3374	0.2184
n	2.3	11.795	46
σ_1	σ_{peak}	σ_{yield}	σ_{yield}
σ_2	σ_{yield}	σ_{peak}	σ_{peak}

5.2.2. System Analysis

Two structural systems (a V-truss, and 3 bars in parallel) were studied to examine the effect of post-peak behavior and load redistribution on the overall deformations and failure of the system.

5.2.2.1.V-Truss

A simple truss with two members angled at 45 degrees (V-truss) was studied. The cylindrical members of length (L) of (24D and 6D) and 0.5 in. diameter, shown in the Fig. 5.2, is subjected to downward monotonic load in a positive direction. The truss consists of two one dimensional members at a 45° away from the vertical line. The two members have the same length, but one member is perfect and the other has imperfection. The amounts of imperfection of 0.001%, 0.01%, 0.1%, 1% and 2.5% were studied to evaluate how they affect the post-peak response. Once the peak load is reached, the imperfect member

undergoes softening following the bilinear post-peak in case of the bilinear post-peak model, Modified Ramberg and Osgood model or nonlinear post-peak in case of the nonlinear curve fitting. While the other member unloads elastically.

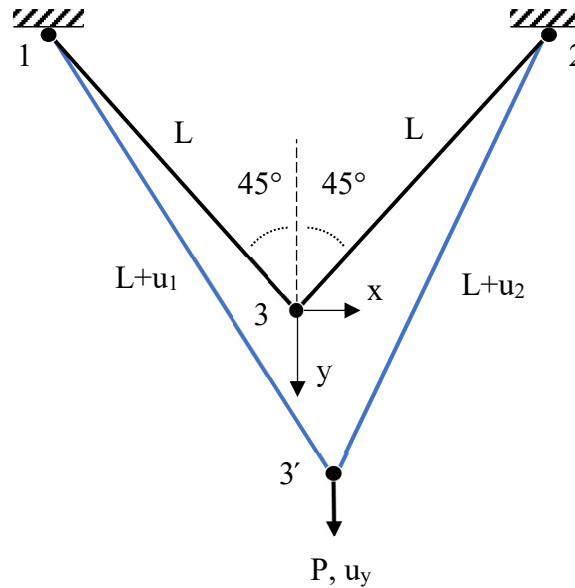


Fig. 5.2. V-Truss under tension

Fig. 5.3 shows that all models were efficiently able to simulate the response of the V truss, and the overall behavior was very close for all models. The simulation results show that for the perfect case, both members will yield and fail simultaneously. By applying as little as 0.001% imperfection to one of the members, the behavior becomes completely different. For the vertical displacement, the behavior is similar to the perfect case, except in the post-peak region which becomes a little steeper with imperfection (see Fig. 5.3) and the total vertical displacement is less.

There is no lateral displacement occurs when both members are perfect. However, 0.001% initial imperfection was enough to cause lateral displacement (see Fig. 5.5). For the imperfect case, the imperfect member yielded before the perfect member causing

unsymmetrical behavior of the system. This behavior can be noticed with the little jump at load of 14 kips shown in Fig. 5.4. The lateral displacement increases due to the yield of the imperfect member. Once the other member starts to yield, both members experience hardening which reduces the lateral displacement until the peak load is reached.

When the imperfect member undergoes softening the perfect member unloads elastically and the lateral displacement increases dramatically. The lateral displacement in the system (which is 0 in the perfect case) increases to almost 1 in. (or 8% of the member length) when considering the imperfect case. The results shown in Fig. 5.5 also shows that the more imperfection, the more lateral displacement occurs.

The bilinear post-peak model was able to capture most of the response of the structure. The amount of the vertical displacement at rupture for bilinear post-peak model is 10% more than the other models and the lateral displacement is 20% less. This is due to the difference in the point on the load displacement curve at which the perfect member starts to unload elastically. For the bilinear post-peak model, the unloading of the perfect member occurs later. The displacement at which the unloading occurs is 17% more for bilinear post-peak curve than for nonlinear curve fitting.

These results show that the inevitable imperfection can have a significant effect on how the structures collapse. This amount of lateral displacement in a collapsing system can change how the members impact each other and how the structure collapses.

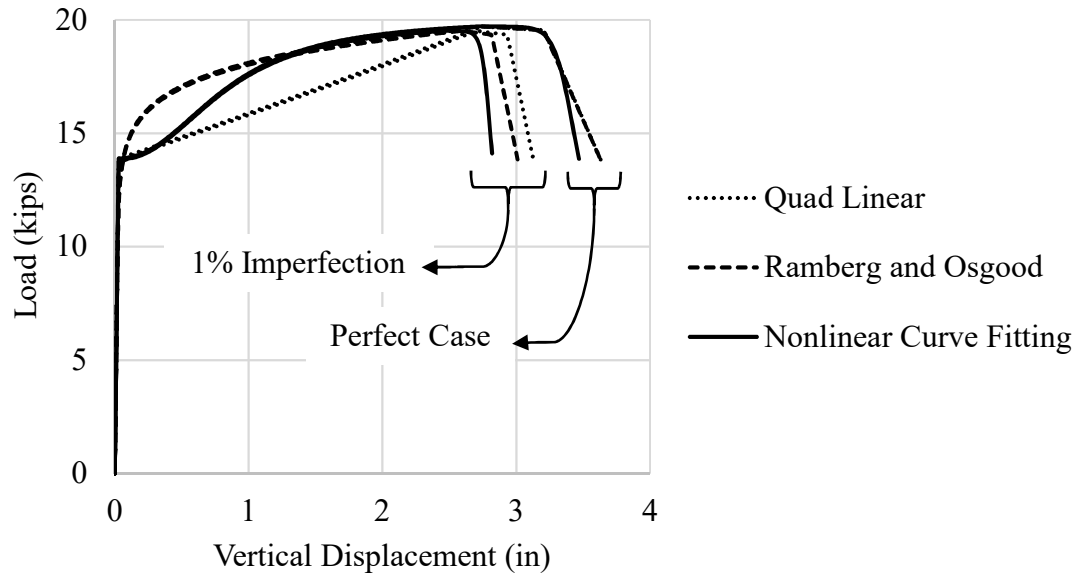


Fig. 5.3. Load vs. vertical displacement of 24D members

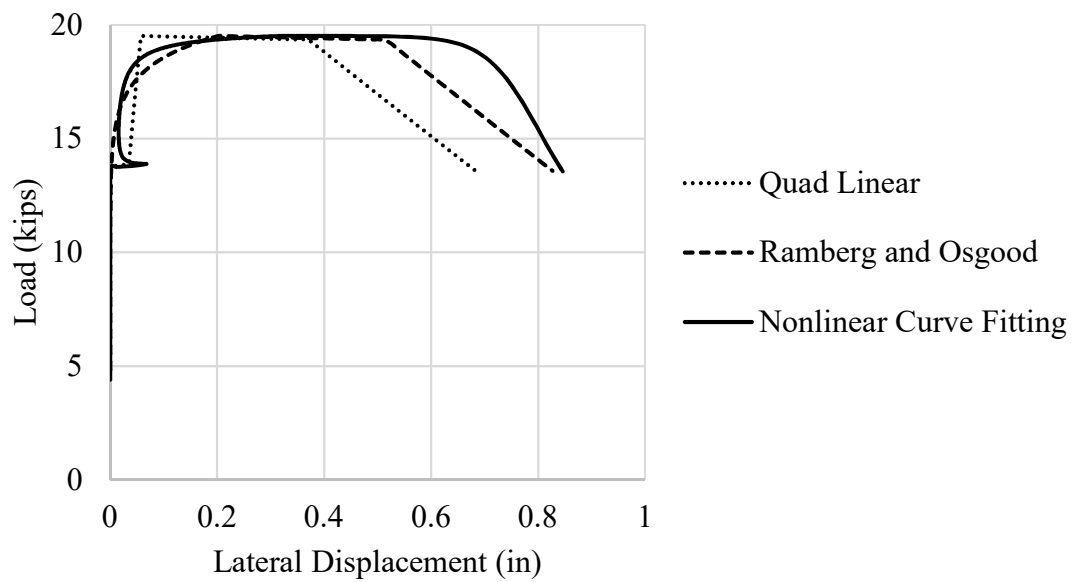


Fig. 5.4. Load versus lateral displacement of 1% imperfection and 24D members

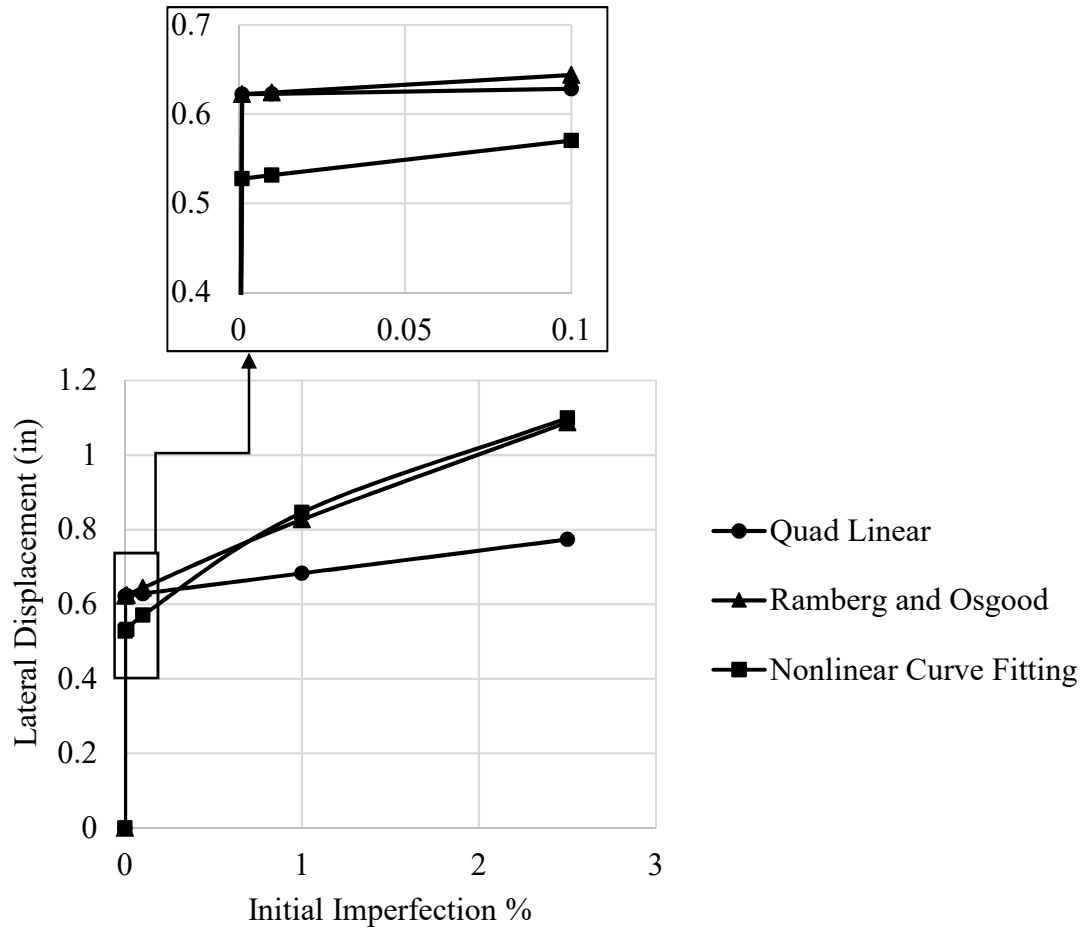


Fig. 5.5. Influence of initial imperfection on lateral displacement of V truss of 24D members

5.2.2.2. Tension Members in Parallel

In this example analysis, three members in parallel are subjected to monotonic tension load as shown in Fig. 5.6. All members have the same length (L). For the simplicity, it is assumed that all members experience no lateral displacement during the loading, and they connected with a rigid bar that can rotate around point (2) as shown in Fig. 5.6. The same parameters studied earlier for the V truss, will be considered for this system. For

unsymmetrical behavior, only one of the outer members will be considered an imperfect member while the two other members are perfect.

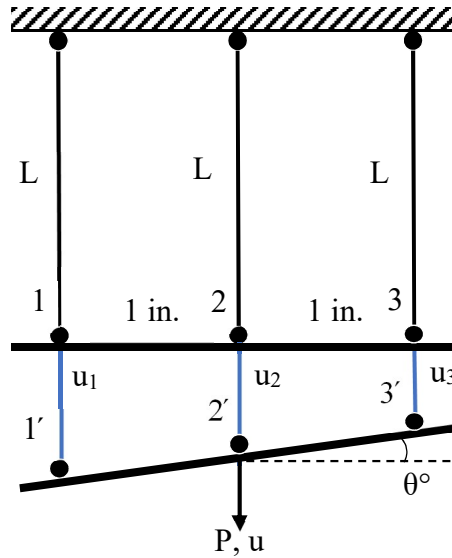


Fig. 5.6. Tension members in parallel

As with the V-truss model, Fig. 5.7 shows that all analysis models were efficiently able to simulate the response of the tension members in parallel, and the overall behavior was very close for all models. Imperfection in one of the members drastically changes the response. A 0.001% initial imperfection on the left member was enough to cause rotation in the system (see Fig. 5.9). Once the imperfect member yields, the rigid bar will rotate about the middle member due to unbalanced forces causing the member on the other side (the right member) to get shorter. As the imperfect member passes its maximum capacity, the rigid bar rotates even further causing the imperfect member to soften and the right member unload elastically while the middle member experiences softening. With a 1% imperfection the rotation reached almost 30 degrees (see Fig. 5.8).

These results show that the inevitable imperfection can have a significant effect on how the structures collapse. The rotation in the system (which is 0 in the perfect case) increases to almost 30 degrees when considering the imperfect case. This amount of rotation in a collapsing system can change how the members impact each other and how the structure collapses.

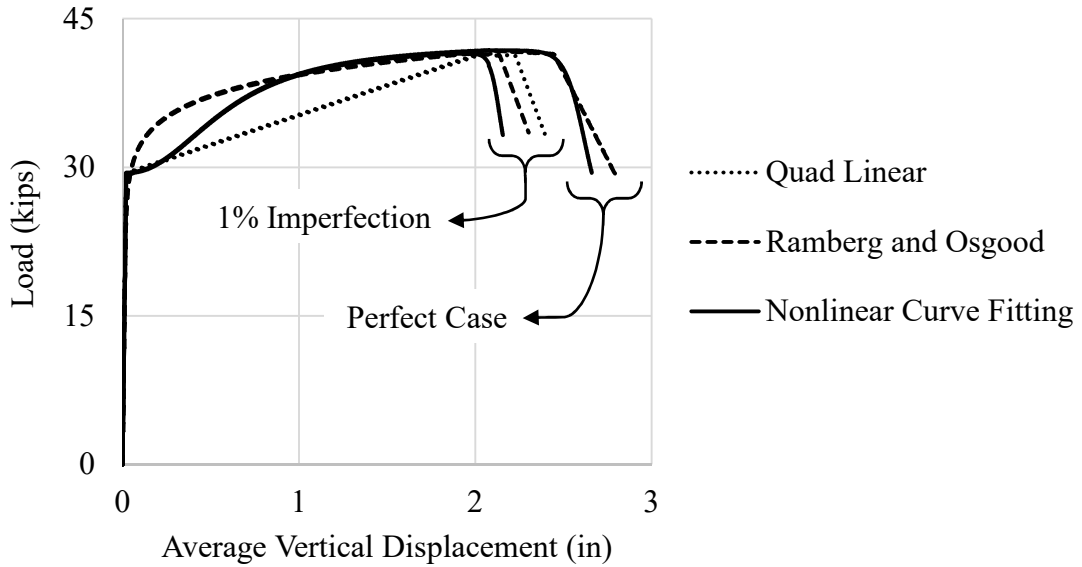


Fig. 5.7. Load versus vertical displacement of 24D members

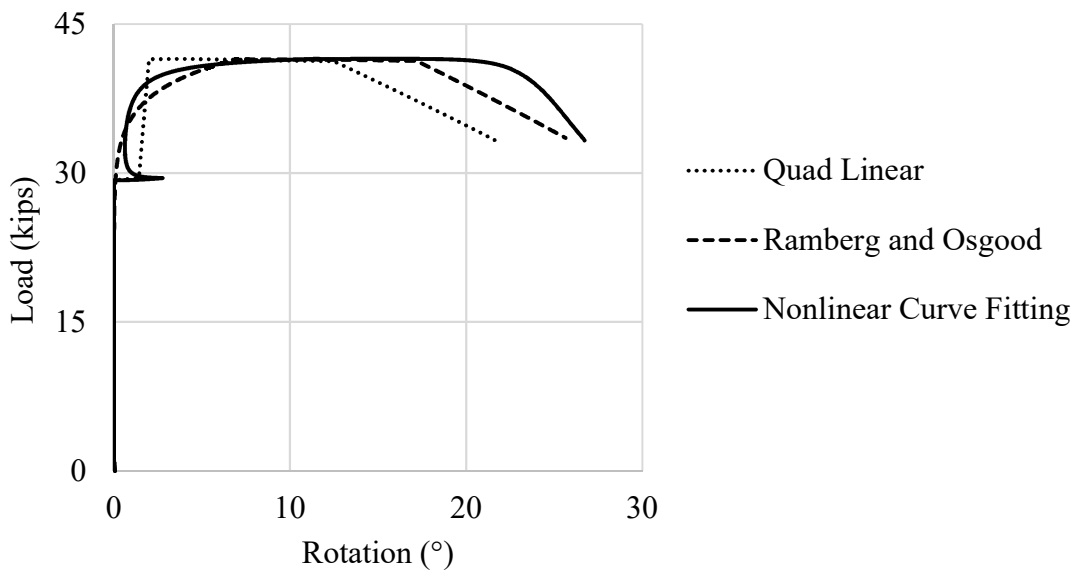


Fig. 5.8. Load versus rotation of 1% imperfection and 24D members

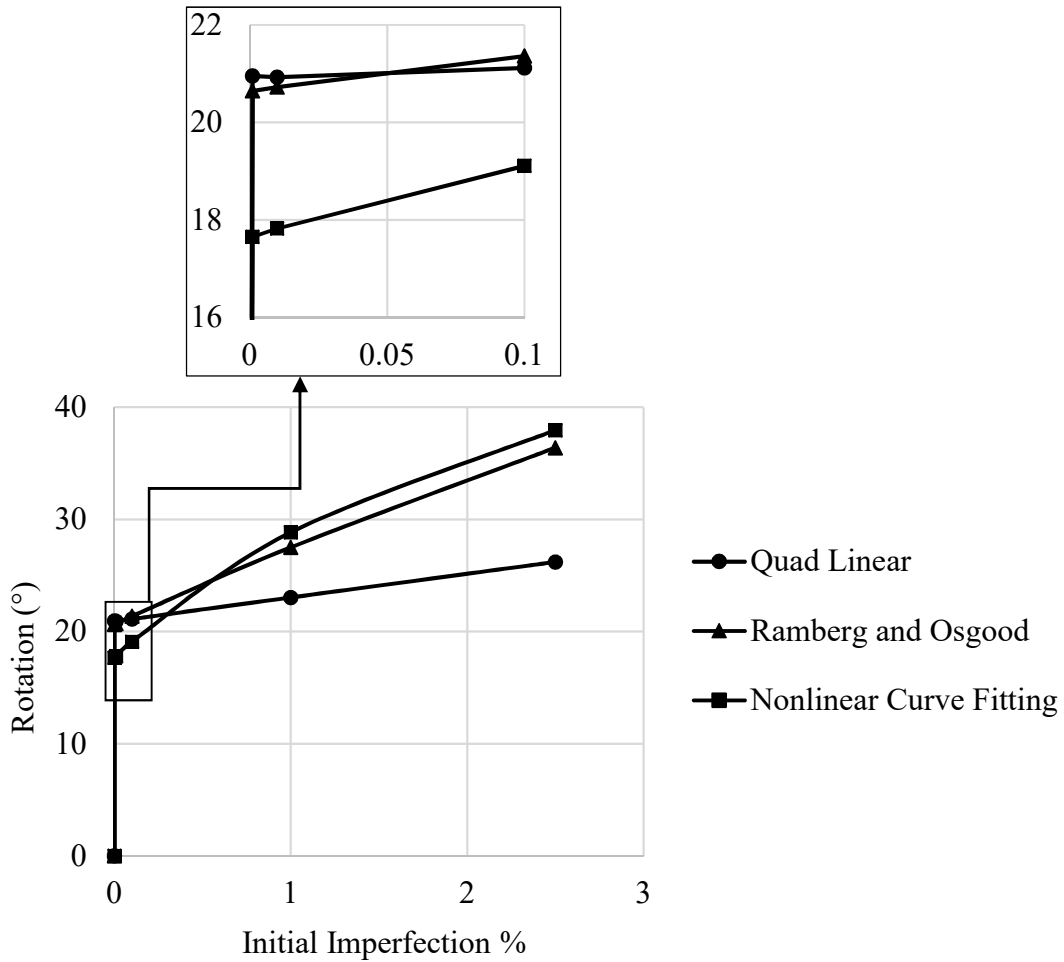


Fig. 5.9. Effect of initial imperfections on the rotation of 24D members in parallel

5.2.3. Analytical Conclusions

A tension model that defines the pre- and post-peak stiffness of the line element, respectively, through bilinear post-peak model, modified Ramberg Osgood pre-peak with bilinear post-peak and nonlinear curve fitting are used in a simple truss structure to evaluate its effectiveness in predicting the post-peak response of a collapsing structure. The analyses showed that the members with even a slight imperfection can cause lateral displacement or rotation that is not be present in a perfect case. The lateral displacement in the V-truss system with 24D long members was found to be almost 1 in, while the rotation in the three

tension members in series was almost 30 degrees. It has also been observed that the more imperfection, the more lateral displacement occurs. The proposed bilinear post-peak model is able to capture most of the structural responses. This allows for a simple model to be effectively used in computational analysis.

It could be concluded from this integrated experimental and computational study that the inevitable imperfection would have a significant effect on how the structures collapse. The amount of lateral displacement or rotation in a collapsing system can change how the members impact each other and how the structure collapses.

5.3. Experimental Study

Nine cylindrical A36 steel specimens were manufactured according to ASTM E8 (2013) as shown in Fig. 5.10. Due to the MTS capacity limit (20 kips), the diameter of all tested specimens was 0.3 in. Three sets of three members in parallel under tension were tested as shown in Fig. 5.11. The fixture was designed so that it has the ability to rotate around the central pin (see Fig. 5.11) when unbalanced forces are produced inside the system. In addition, three single specimens manufactured as shown in Fig. 3.5 ($L=10D$) were tested to determine the material properties and the other parameters (such as localization length and softening factor) that are essential for the numerical model. Table 5.2 and Table 5.3 show the specimen information and key experimental results for the one member and three members in parallel tests, respectively. For increasing the DIC accuracy, all tested specimens were painted with matte white color base, and then a matte black color was sprayed to create a random speckle pattern.

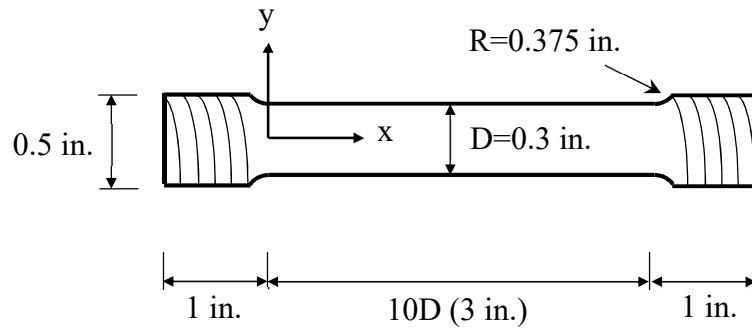


Fig. 5.10. Dimensions of steel specimen (triple tension test)

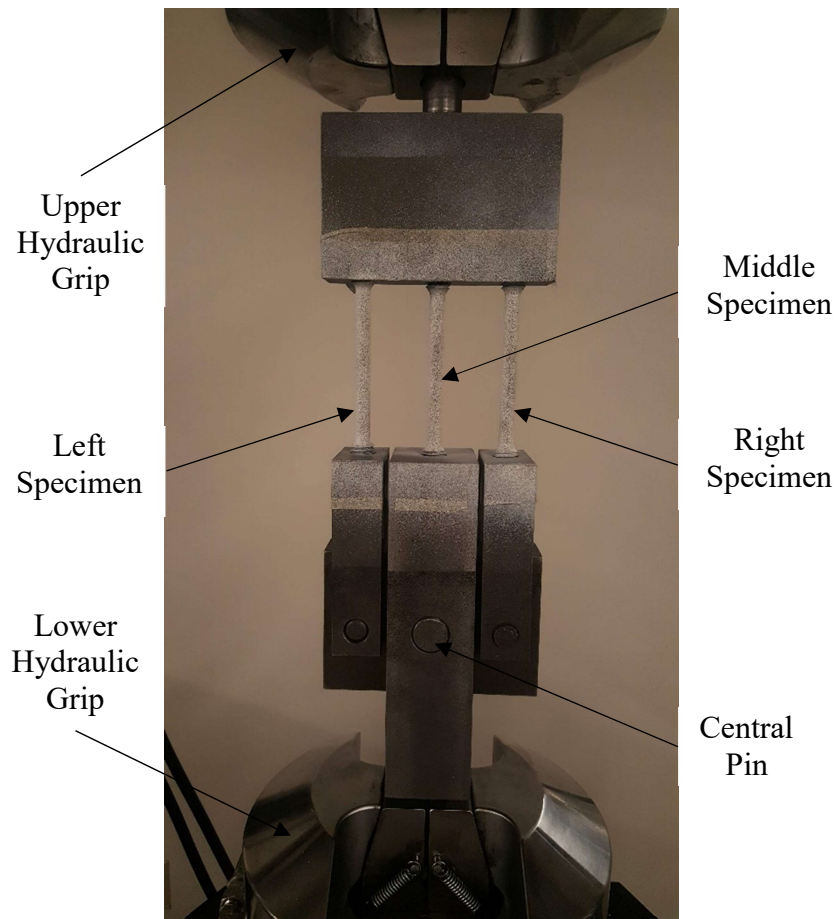


Fig. 5.11. Three members in parallel

Table 5.2. Single member tests

Specimen I.D.	Length (in)	Peak Load (lb)	Rupture Load (lb)	ϵ_x at Peak Load (in/in)	ϵ_x at Rupture Load (in/in)
10D-1	3	5268	3524	0.15543	0.22342
10D-2	3	5308	3510	0.17672	0.27309
10D-3	3	5267	3491	0.16557	0.23554

Table 5.3. Three members in parallel

Specimen I.D.	Length (in)	Peak Load (lb)	Rupture Load (lb)	ϵ_x at Peak Load (in/in)	ϵ_x at Rupture Load (in/in)
Test-1	3	15909	11852	0.17202	0.25250
Test-2	3	16005	11819	0.17040	0.25606
Test-3	3	15928	12955	0.16438	0.20300

5.3.1. Test Setup

The same test setup used in the previous experimental work was used in these tests. Monotonic displacement-controlled tension tests with strain rate of 0.0125 strain per minute before yield and 0.1 strain per minute after yield were performed. The 3D DIC system, shown in Fig. 3.6, was used to capture the deformations along the specimen length. The stress versus strain data were obtained by synchronizing the loads from MTS machine with images captured by the 3D DIC data acquisition system. Fig. 5.12 (single member test) and Fig. 5.13 (three members in parallel test) show the specimens after rupture where the upper ends were attached to the MTS upper fixed part and the lower ends were attached to the MTS lower moving part.



Fig. 5.12. Three specimens of one-member test after rupture

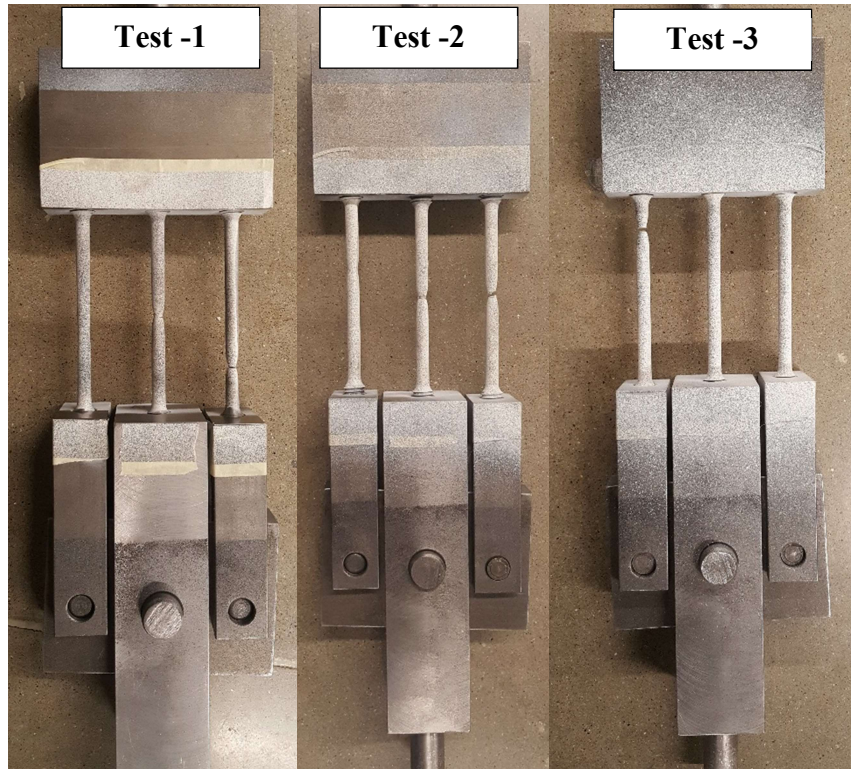


Fig. 5.13. Three members in parallel test after rupture

5.3.2. Experimental Results

5.3.2.1. Single Member Tests

The engineering stress versus engineering strain curves of single tension test specimens are plotted in Fig. 5.14. All the specimens failed at approximately same load but different displacements. The specimen 10D-2 failed at larger displacement than the other two specimens. This may be due to the amount of imperfection in diameter with parallel section (see Table 5.5) because the diameter of the specimens is 0.3 which is more susceptible to have more initial imperfection than specimen with 0.5 in. of diameter. As recommended by ASTM E8 (2013), the ends of the reduced parallel section must be not more than 1 % larger in diameter than the center of the specimen. However, Table 5.5 shows that the ends of the reduced parallel section 10D-2 specimen are less than 1% but the others are more than 1%. Hence, the more variation in diameter along the specimen length, the specimen more likely to fail with less displacement. For example, the specimen 10D-1 whose diameter at the ends are 2% more than the diameter at the center fails at 18% less than 10D-2 specimen which has 0.2% variation in diameter along the length.

The normalized longitudinal engineering strains and (ϵ_{xx}) for specimens 10D-1, 10D-2 and 10D-3 along the specimen length are plotted at the rupture load in Fig. 5.15. The average of maximum longitudinal strain of all specimens is 1.366 in/in. As this strain is related to the rupture load, all specimens also failed at a similar load. However, the specimen 10D-2 experienced higher average longitudinal strain than the others which leads to larger displacement. This may be due to the manufacturing. The data provided in Table 5.4 is the localization length and softening factor of all tested specimens which are important factors for the numerical model.

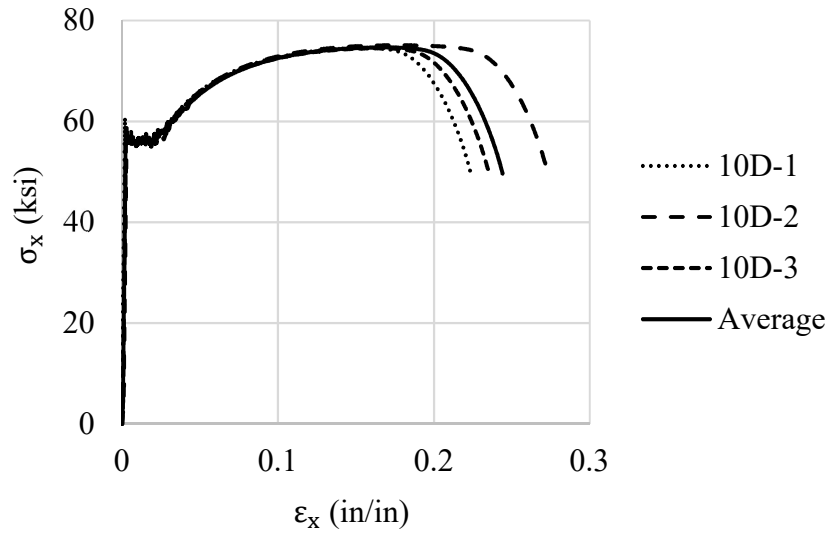


Fig. 5.14. Engineering stress vs. strain for single tension tests

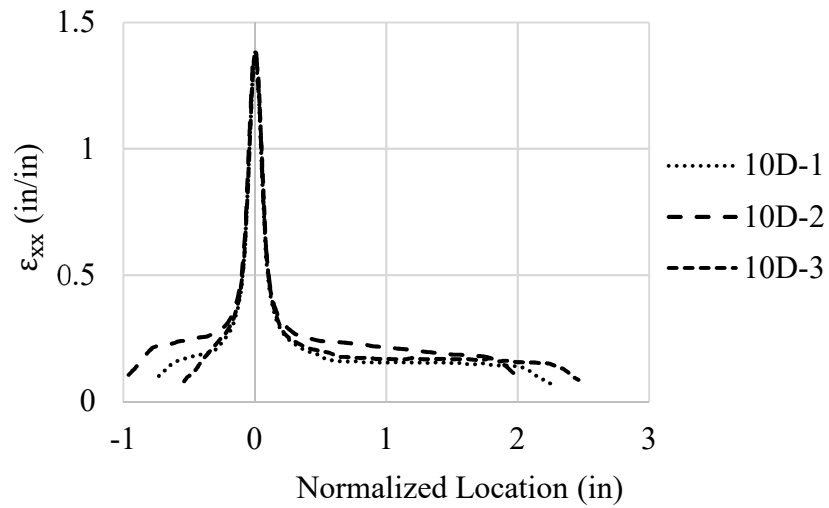


Fig. 5.15. Longitudinal engineering strain along length of single tension tests at rupture load

Table 5.4. Localization length and softening factor determined longitudinal strain method

Specimen I.D.	Lc at Bifurcation Point (in)	Softening Factor
10D-1	1.382	0.00537
10D-1	2.264	0.00720
10D-2	1.508	0.00566

Table 5.5. Difference in diameters along the specimen to the diameter at the middle

Specimen ID	Difference in diameter (%)
10D-1	1.9
10D-1	0.1
10D-2	1.2

5.3.2.2.Parallel Tension Tests

In order to examine the effect of post-peak behavior on adjacent specimens, test of three tension members in parallel were conducted. Load versus center displacement obtained from the MTS machine for the three members in parallel tests are plotted in Fig. 5.16. Fig. 5.16 shows that Test-1 and Test-2 fail approximately at the same load and relatively similar displacement (see Table 5.3). The third test, however, fails at load 10% higher and at displacement 21% less than the other two tests. This is because, in the third test, only one member softens and eventually fails while in the Test-1 and Test-2, at least two members soften and fail almost simultaneously as shown in Fig. 5.13. This behavior is predicted by the analytical study that is performed in Section 5.2. The curves of load versus displacement along every member in the test are plotted in Fig. 5.17 and Fig. 5.18.

Both figures show that all members pass the peak load which means that all members experience softening. Furthermore, all members in Test-2 fail within almost the same displacement while in Test-1, one member starts to unload at a displacement 90% of the post-peak region. Unfortunately, most of the acquired 3D DIC images of Test-3 were lost due to the large number of images that were being acquired.

The unbalanced forces inside the system are redistributed causing relative deformations of outer members which eventually make the system to rotate around the central pin as shown in Fig. 5.19. Up to the yield load, almost no rotation in the system is noticed. At the yield load, the system experiences a sudden rotation of 1° due to yielding one member before the others. Then drop back to 0.1° . During the hardening stage, the rotation remains within 0.2° up to the peak load where the average of rotation (the amount of relative displacement of the outer members in degrees) of the Test-1 and Test-2 is almost 0.2° . Fig. 5.20 shows that the rotation remains approximately 0.2° till after the peak load (normalized displacement=1 at the peak load). However, after around 1% drops in load, the increase in rotation of the system becomes larger because one of the outer members begins to soften while the others unload elastically. The rotation of Test-1 increases to around 4° which is 63% more than the Test-2 due to unloading one of the members. Less amount of rotation of Test-2 is noticed because one member starts to unload close to rupture load of the system.

To investigate the post-peak behavior of three members in parallel even further, the longitudinal engineering strain along every member at the rupture load is plotted in Fig. 5.21 and Fig. 5.22. The maximum longitudinal engineering strain in all members in Test-1 and Test-2 is more than 0.49 in./in. which is 36% of the maximum longitudinal

engineering strain. Even though Fig. 5.13 shows that two members in Test-1 and Test-2 fail, Fig. 5.21 and Fig. 5.22 shows that the member in the middle does not reach the maximum engineering strain at rupture load. So, the member in the middle fails due to the amount of energy released by the first member that fails. Table 5.6 shows the maximum longitudinal engineering strain of every specimen of members in parallel and what percent every member reaches with respect to the amount of the maximum longitudinal engineering strain.

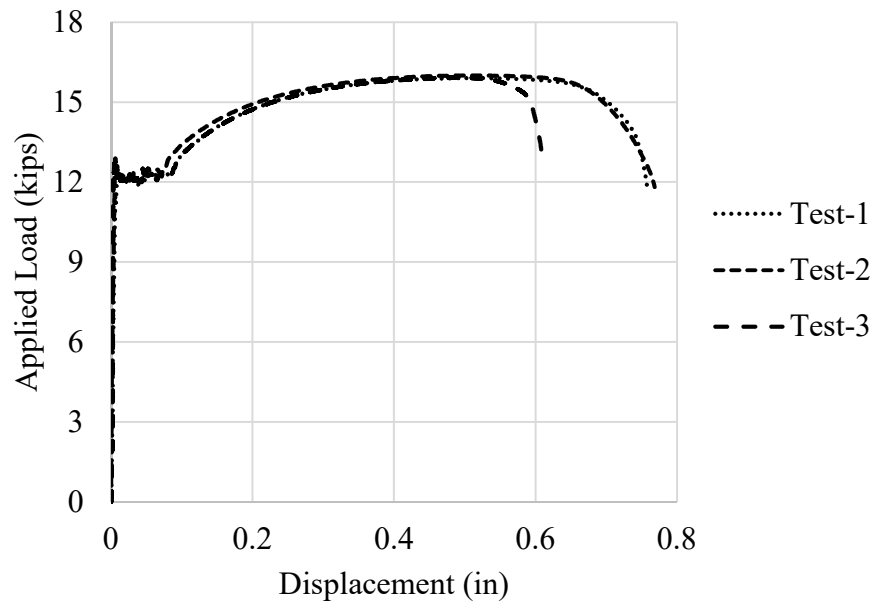


Fig. 5.16. Load-displacement of all triple tension tests

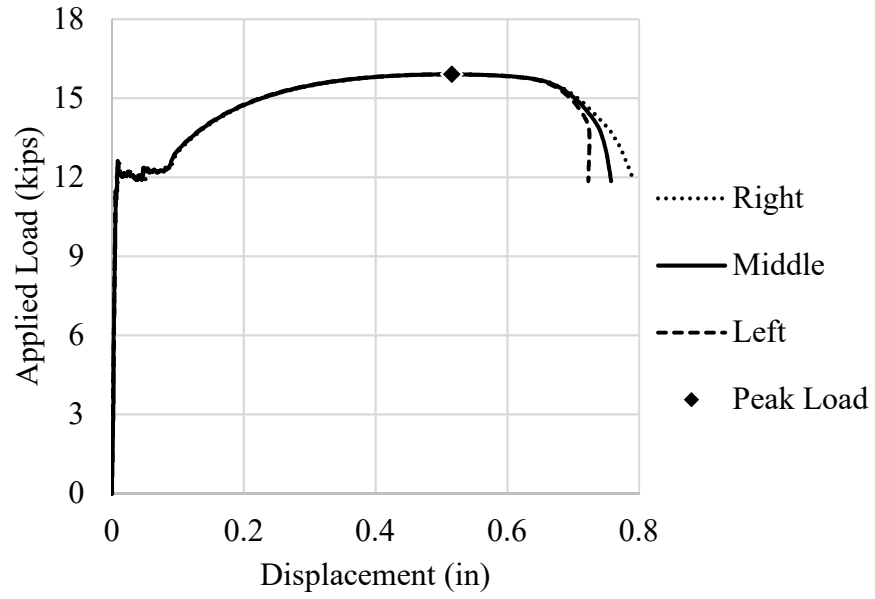


Fig. 5.17. Load-displacement of specimens of Test-1

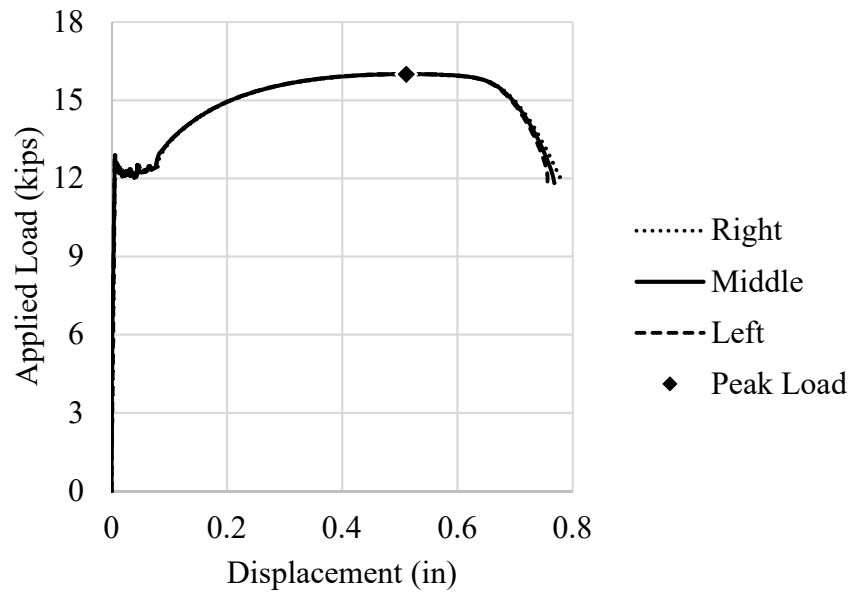


Fig. 5.18. Load-displacement of specimens of Test-2

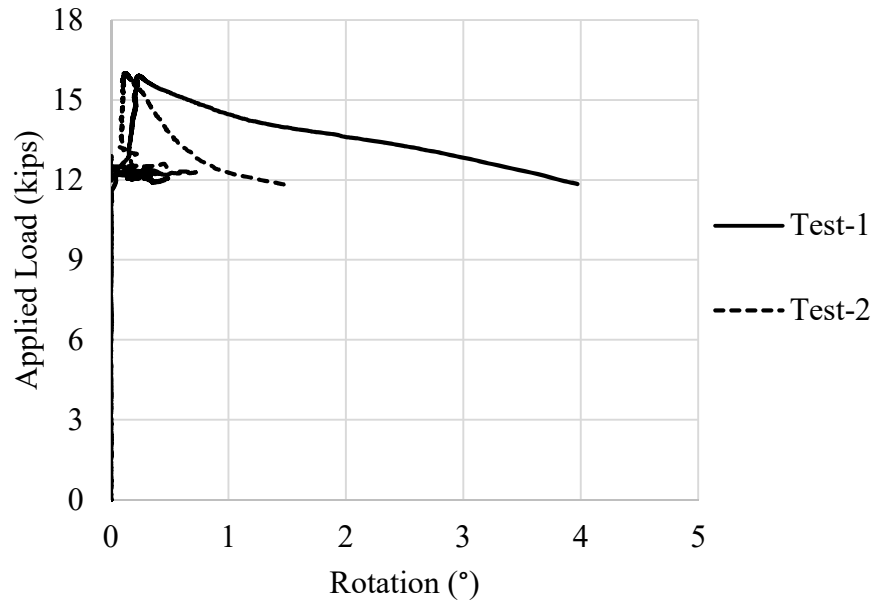


Fig. 5.19. Load versus rotation of parallel tension tests

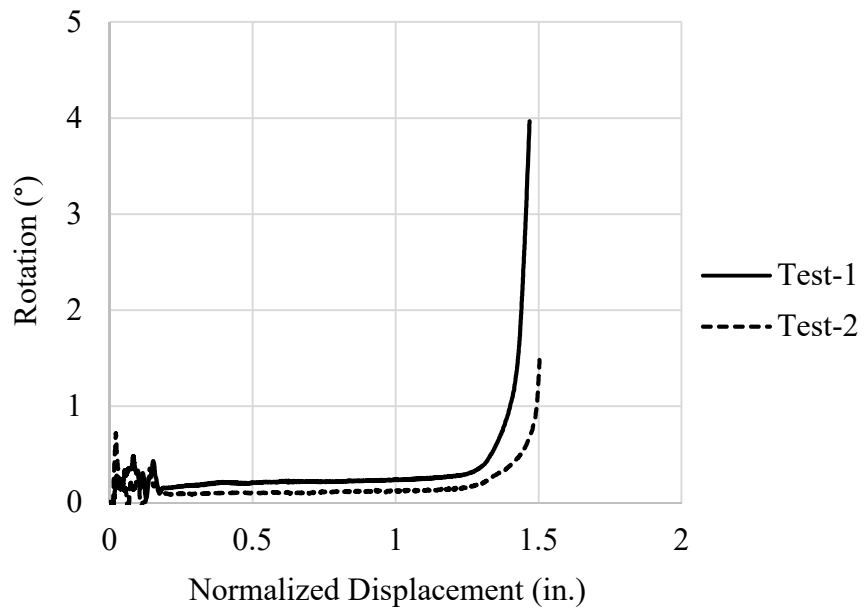


Fig. 5.20. Normalized displacement versus rotation of parallel tension tests

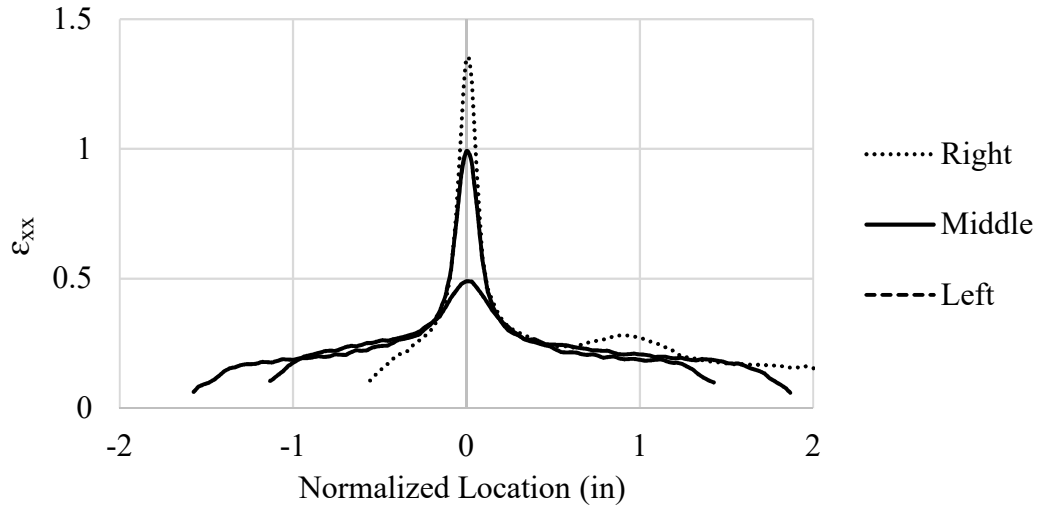


Fig. 5.21. Longitudinal engineering strain along length of specimens of Test-1 at rupture
load

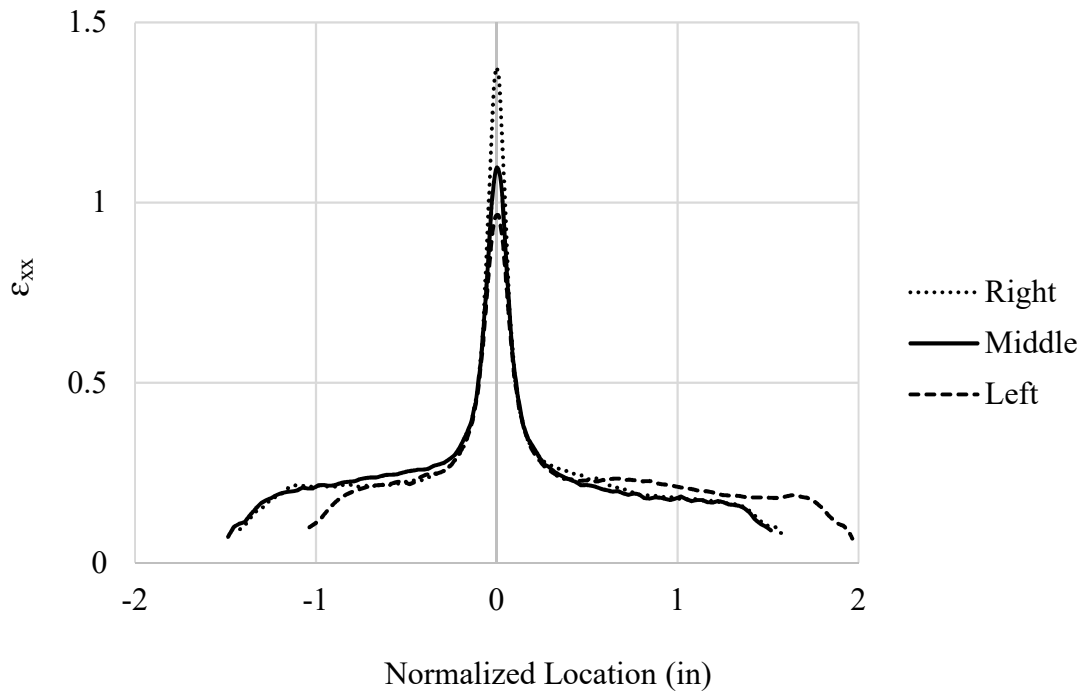


Fig. 5.22. Longitudinal engineering strain along length of specimens of Test-2 at rupture
load

Table 5.6. Maximum longitudinal engineering strain of every specimen of members in parallel at rupture load

Specimen	Test-1		Test-2	
	Maximum ϵ_{xx} (in./in.)	Ratio of maximum ϵ_{xx} to the maximum ϵ_{xx} of first member that fails (%)	Maximum ϵ_{xx} (in./in.)	Ratio of maximum ϵ_{xx} to the maximum ϵ_{xx} of first member that fails (%)
Right	1.351	100	0.964	70
Middle	0.992	73	1.0971	80
Left	0.490	36	1.375	100

5.3.3. Comparison of Numerical Bilinear Post-Peak Model with Experiments

The bilinear post-peak model developed in Chapter four is compared with Test-1 and Test-2 results, to study the effectiveness of the numerical model of capturing the post-peak response of steel system. The pre- and post-peak stiffnesses were determined based on the average data of the three single member tests. The localization length is 1.395 in. and the softening factor is 0.003776. These data are used to predict the post-peak response of three members in parallel for perfect case (no initial imperfection) and imperfect case (an initial imperfection). The perfect case when all members undergo softening which causes no rotation while the imperfect (cross-sectional area has initial imperfection of 0.5%) case where only one member softens causes rotation in the system. Fig. 5.23 shows the comparison of load versus displacement of bilinear post-peak model and the experiments. With no initial imperfection, the bilinear post-peak model fails at load 4% higher and displacement 1% more than the experiment. However, due to considering perfect case, the bilinear post-peak model predicts no rotation while, in Fig. 5.19, experiments show that Test-2 has a rotation of 4° at rupture load.

To study the influence of initial imperfection of the post-peak response on members in parallel, initial imperfection of 0.5% is used to predict the bilinear post-peak behavior. Fig. 5.24 shows that the bilinear post-peak model with 0.5% imperfection is able to predict the post-peak response. The bilinear post-peak model fails at load 1% higher and displacement 4% more than the experiment.

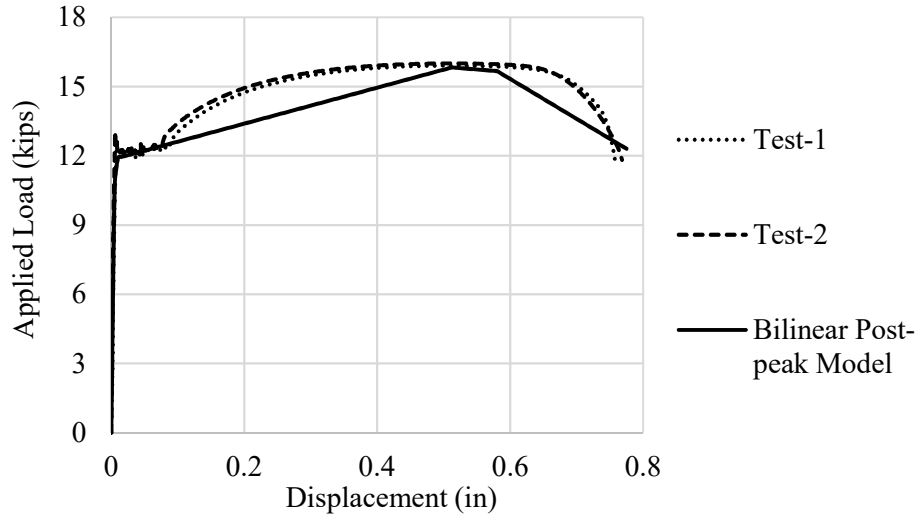


Fig. 5.23. Comparison the load-displacement of experiments (Test-1 and Test-2) and bilinear post-peak model

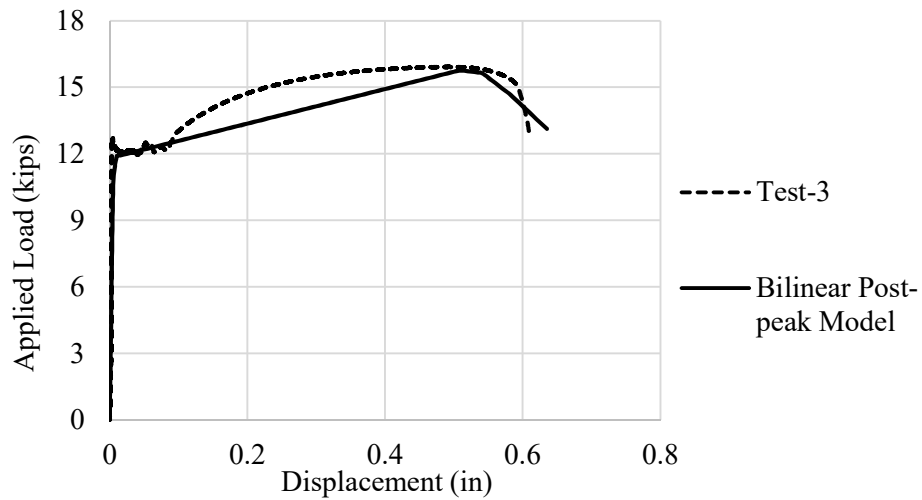


Fig. 5.24. Comparison the load-displacement of experiments (Test-3) and bilinear post-peak model with 0.5% initial imperfection

5.4. Summary and Conclusions

Simulation of structures under collapse requires accurate prediction of their post-peak behaviors. In order to investigate the post-peak response of steel structures, two simple structural systems were analyzed analytically, and one system tested experimentally.

Analytical study is performed. An alternative approach is proposed which consists of a one-dimensional single line element that includes the effect of localization. The model defines the pre- and post-peak stiffness of the line element, respectively, through a bilinear post-peak model. This tension model is used in a simple truss structure to evaluate its effectiveness in predicting the post-peak response of a collapsing structure. The analyses show that the members with even a slight imperfection can cause lateral displacement or rotation that is not present in a perfect case. The lateral displacement in the V-truss system with 24D long members was found to be almost 1 in, while the rotation in the three tension members in parallel was almost 30 degrees. It has also been observed that the more imperfection, the more lateral displacement occurs. The proposed bilinear post-peak model is able to capture most of the structural responses. This allows for a simple model to be effectively used in computational analysis.

Experiments are conducted to study the post-peak response of three members in parallel. Experiments show that two tests fail approximately at the same load and relatively similar displacement while the third test fails at load 10% higher and at displacement 21% less than the other two tests. The reason behind this behavior is that, in the first two tests, at least two members soften and fail almost simultaneously. While in the third test, only one member softens and fails. Due to unbalanced behavior of all members in the system,

rotation of the system occurs. After the bifurcation point, rotation of the system becomes larger because one of the outer members begins to soften while the others unload elastically. The second test rotates less than the other tests because all members soften and only one member starts to unload at a displacement 90% of the post-peak region. This behavior is also studied by looking at the longitudinal engineering strain along every member. The bilinear post-peak model that is developed in Chapter four is used to predict the post-peak behavior of three members in parallel. Perfect case and imperfect case with initial imperfection of 0.5% are simulated and compared with the experimental results. The results show that the bilinear post-peak model is efficiently capable of capturing the post-peak behavior of three members in parallel with a difference of 4%.

It could be concluded from this integrated experimental and computational study that the inevitable imperfection would have a significant effect on how the structures collapse. The amount of lateral displacement or rotation in a collapsing system can change how the members impact each other and how the structure collapses.

CHAPTER SIX

CHAPTER 6: CONCLUSIONS AND FUTURE WORK

6.1. Summary

Accurate simulation of extreme limit states in structures subjected to abnormal loads, earthquake or blast requires detailed understanding of the post-peak behavior. In steel structures, these extreme-limit states are associated with local or global instability such as local buckling, tension necking and fracture. The accompanying loss of component strength may lead to structural collapse. Several methods have been developed to simulate such extreme limit states such as fiber models, hinge models, nonlocal models and finite element analysis (FEA). However, disadvantages of some of these methods arise when the structural elements pass the peak response and experience post-peak softening. Furthermore, there is a lack of experimental data to validate the numerical solutions especially for the nonlocal models.

The overall goal of this research is to improve understanding of structural response during extreme limit states and collapse through improved simulation capabilities during post-peak response. The first objective of this research was to experimentally and numerically investigate the length scale of the post-peak behavior of steel members subjected to monotonic tension. A novel method to determine the localization length based on experimental data was proposed and evaluated. The second objective sought to develop an analytical formulation to represent post-peak behavior of steel members under tension. A numerical localization model based on the experimental data was developed to simulate the post-peak response of a one-dimensional steel member subjected to monotonic tension

in order to eliminate mesh sensitivity. The third objective sought to experimentally and analytically investigate the load redistribution of three members in parallel under monotonic tension to investigate how the post-peak behavior of one member affects the loading or unloading in other members.

6.2. Conclusions

The following conclusions were drawn from this study:

- The experimental results confirmed that the post-peak behavior is influenced by the specimen length. Longer specimens have steeper, almost brittle, post-peak curves.
- The experimental results showed that longitudinal and transverse strain fields as a function of longitudinal axis (x-axis) are similar at rupture load near the center of the localization, but as the length of the specimen decreases so does the longitudinal engineering strains away from the center of the localization.
- Two methods of determination of localization length (average strain method and longitudinal strain methods) were evaluated. In the average strain method, the localization length is defined to be the distance between the two points at which the longitudinal engineering strain field at a load and the engineering strain field intersect. The results indicate that the strain localization starts significantly before the peak load, which does not comply with theory. Furthermore, the localization length calculated by this method depends on the specimen length, i.e. longer localization lengths for longer specimens. In the longitudinal strain method, the localization length is defined to be the distance between the two points at which the longitudinal engineering strain field starts to touch the one at failure load. The

results illustrated that the strain localization occurs beyond the peak load at the bifurcation point where the localized necking initiates. By normalizing the strains at the bifurcation point for all specimens, the evolution of localization length was approximately identical for specimens whose lengths are at least 6 times the diameter. The experimental results also showed that the engineering stress-strain curve of a localization length corresponding to the instantaneous localization zone was almost identical. In both methods, the experimental results showed that the localization length is not constant, but evolves as the member moves through the post-peak region. The localization length for the longitudinal strain method was approximately 5 times the diameter at the bifurcation point and reduced to 0.6 times at failure.

- Three post-peak models (linear - based on the average strain method, bilinear and nonlinear - based on the longitudinal strain method) were developed. The bilinear and the nonlinear used a new failure criterion (when the longitudinal engineering strain inside the localization length at rupture load reaches 0.354 in./in.). The differences in displacement at the rupture load between linear, bilinear and nonlinear post-peak models and experiments were 10%, 6% and 3%, respectively. While the differences in rupture load between linear post-peak model and bilinear and nonlinear post-peak models and experiments were 16% and 8%, respectively. The results also showed that the nonlinear post-peak model could predict the displacement at rupture load to 1% of the experimental results.
- A FEA model using isotropic strain hardening was developed to capture the post-peak behavior of steel members under tension. The FEA model, which uses an

isotropic strain hardening law, causes the localized necking to occur at the peak load not at the bifurcation point as in the experiments. The comparison of load displacement of specimens simulated by FEA with experimental ones showed that the difference in displacement at the rupture load between FEA simulations and experiments was as much as 12%. The percentage of difference between the maximum experimental and simulated longitudinal engineering strain at the bifurcation is around 33%. This error percentage increases to be around 50% at the rupture load. The FEA simulated localized necking at the peak load caused the simulated steel member to fail at less displacement and have larger amount of maximum longitudinal engineering strain compared to experiments.

- An analytical study of a system of tension members showed that the members with even a slight imperfection can cause lateral displacement or rotation. The lateral displacement in the V-truss system with 24D long members was found to be almost 1 in., while the rotation in the three tension members in parallel was almost 30 degrees.
- Experiments were conducted to study the post-peak response of three members in parallel. The experiments showed that the rotation remains almost constant after the peak load and increased dramatically when the bifurcation point was reached. For one test, in which only one member experienced softening, did so at a load 10% higher and at displacement 21% less than the system in which two or more of its members experienced softening.
- The numerical localization model based on the bilinear post-peak stiffness was able to simulate the post-peak behavior of three members in parallel. The difference in

displacement at the rupture load between the numerical simulations and the experiments was 4%.

6.3. Future work

Future work in the area of numerical localization model and load redistribution in collapsing systems needs to be conducted in:

- Additional tests for the specimens of different materials and sizes. The numerical localization model can be enhanced and made more generic by taking into account the different steel bars diameters, shapes, and material properties.
- Additional tests for the specimens under compression. Developing numerical localization model for steel members subjected to compression will enhance the numerical model that will be used to predict the post-peak of indeterminate steel structures.
- Further developing the FEA model. The internal longitudinal engineering strain and the global displacement can be simulated accurately by making the FEA model account for the strain rate and adding the failure criterion.
- Experimental investigation into the post-peak behavior of 3D steel trusses and indeterminate steel structures. Many simplifying assumptions (symmetrical loading, determinant structure, no lateral movement) were made in the analysis and more experimental and analytical investigations are needed to clarify these factors.
- Application of model to structural systems. By dividing the system element into finite segments or fiber within the cross section, the localization model may be an alternative method to modeling fiber within the cross section or extended for modelling the post-peak response of finite segment within structural element.

REFERENCES

- ASTM A370-17. (2017). *Standard Test Methods and Definitions for Mechanical Testing of Steel Products*. 49. <https://doi.org/10.1520/A0370-17>
- ASTM Committee on Mechanical Testing. (2013). Standard Test Methods for Tension Testing of Metallic Materials. *ASTM International, ASTM Stds.*(Designation: E8/E8M-13a), 1–28. <https://doi.org/10.1520/E0008>
- Bao, C., Francois, M., & Le Joncour, L. (2016). A Closer Look at the Diffuse and Localised Necking of A Metallic Thin Sheet: Evolution of the Two Bands Pattern. *Strain*, 52(3), 244–260. <https://doi.org/10.1111/str.12184>
- Bažant, Z. P. (1976). Instability, Ductility and Size-effect in Strain-Softening Concrete. *Journal Of The Engineering Mechanics Division*, 1976(April), 331–343.
- Bažant, Z. P. (2003a). Asymptotic Matching Analysis of Scaling of Structural Failure Due to Softening Hinges. I: Theory. *Journal of Engineering Mechanics*, 129(6), 641–650. [https://doi.org/10.1061/\(ASCE\)0733-9399\(2003\)129:6\(641\)](https://doi.org/10.1061/(ASCE)0733-9399(2003)129:6(641))
- Bažant, Z. P. (2003b). Asymptotic matching analysis of structural failure due to softening hinges. 2: Implications. *ASCE J. Engng Mech.*, 129(June), 651–654.
- Bazant, Z. P., Belytschko, T. B., & Chang, T. P. (1984). Continuum Theory for Strain Softening. *ASCE J. Eng. Mech.*, 110(12), 1666–1692.
- Bažant, Z. P., & Cedolin, L. (2010). Stability of Structures. In *Elastic, inelastic, fracture and damage theories (1st ed.) Oxford University Press, New York* (Vol. 60). <https://doi.org/10.1142/7828>
- Bigoni, D. (2012). *Nonlinear Solid Mechanics : Bifurcation Theory and Material Instability*. Cambridge University Press.

- Bondok, D. (2017). *Roof Truss Systems Under Blast Loads*. University of Missouri--Columbia.
- Cabot, G. P., Bažant, Z. P., & Tabbara, M. (1988). Comparison of various models for strain-softening. *Engineering Computations*, 5(2), 141–150. <https://doi.org/10.1108/eb023732>
- Chen, Z., Gan, Y., & Labuz, J. F. (2008). Analytical and Numerical Study of the Size Effect on the Failure Response of Hierarchical Structures. *International Journal for Multiscale Computational Engineering*, 6(4), 339–348.
- Chen, Z., & Schreyer, H. L. (1990). A numerical solution scheme for softening problems involving total strain control. *Computers & Structures*, 37(6), 1043–1050. [https://doi.org/10.1016/0045-7949\(90\)90016-U](https://doi.org/10.1016/0045-7949(90)90016-U)
- Considère, M. (1885). Memoire sur l'emploi du fer et de l'acier dans les constructions. *Annales Des Ponts et Chaussées*, 9, 574–775. Retrieved from https://scholar.google.com/scholar?cluster=5898883448872487343&hl=en&as_sdt=5,26&scioldt=0,26
- Cooke, R. J., & Kanvinde, A. M. (2015). Constitutive parameter calibration for structural steel: Non-uniqueness and loss of accuracy. *Journal of Constructional Steel Research*, 114, 394–404. <https://doi.org/10.1016/j.jcsr.2015.09.004>
- Dai, H.-H., Zhu, X., & Chen, Z. (2011). An Analytical Study on the Post-Peak Structural Response. *Journal of Applied Mechanics*, 78(4), 044501. <https://doi.org/10.1115/1.4003740>
- Dantec Dynamics. (2017). *ISTRA 4D - Software Manual Q-400 System 4.4.6 v2*. Retrieved from <https://www.dantecdynamics.com/>

- Elices, M., & Planas, J. (1989). Material models. *Fracture Mechanics of Concrete Structures*, 16–66.
- Jansen, D. C., & Shah, S. P. (1997). Effect of Length on Compressive Strain Softening of Concrete. *Journal of Engineering Mechanics*, Vol. 123, pp. 25–35.
[https://doi.org/10.1061/\(ASCE\)0733-9399\(1997\)123:1\(25\)](https://doi.org/10.1061/(ASCE)0733-9399(1997)123:1(25))
- Jirásek, M., & Rolshoven, S. (2003). Comparison of integral-type nonlocal plasticity models for strain-softening materials. *International Journal of Engineering Science*, 41(13–14), 1553–1602. [https://doi.org/10.1016/S0020-7225\(03\)00027-2](https://doi.org/10.1016/S0020-7225(03)00027-2)
- Jirásek, M., & Rolshoven, S. (2009a). Localization properties of strain-softening gradient plasticity models. Part I: Strain-gradient theories. *International Journal of Solids and Structures*, 46(11–12), 2225–2238. <https://doi.org/10.1016/j.ijsolstr.2008.12.016>
- Jirásek, M., & Rolshoven, S. (2009b). Localization properties of strain-softening gradient plasticity models. Part II: Theories with gradients of internal variables. *International Journal of Solids and Structures*, 46(11–12), 2239–2254.
<https://doi.org/10.1016/j.ijsolstr.2008.12.018>
- Joun, Mansoo, Choi, I., Eom, J., & Lee, M. (2007). Finite element analysis of tensile testing with emphasis on necking. *Computational Materials Science*, 41(1), 63–69.
<https://doi.org/10.1016/j.commatsci.2007.03.002>
- Joun, ManSoo, Eom, J. G., & Lee, M. C. (2008). A new method for acquiring true stress-strain curves over a large range of strains using a tensile test and finite element method. *Mechanics of Materials*, 40(7), 586–593.
<https://doi.org/10.1016/j.mechmat.2007.11.006>
- Kolwankar, S., Kanvinde, A., Kenawy, M., & Kunnath, S. (2017). Uniaxial Nonlocal

- Formulation for Geometric Nonlinearity–Induced Necking and Buckling Localization in a Steel Bar. *Journal of Structural Engineering*, 143(9), 04017091. [https://doi.org/10.1061/\(ASCE\)ST.1943-541X.0001827](https://doi.org/10.1061/(ASCE)ST.1943-541X.0001827)
- Kolwankar, S., Kanvinde, A., Kenawy, M., Lignos, D., & Kunnath, S. (2018). Simulating Local Buckling-Induced Softening in Steel Members Using an Equivalent Nonlocal Material Model in Displacement-Based Fiber Elements. *Journal of Structural Engineering*, 144(10), 04018192. [https://doi.org/10.1061/\(ASCE\)ST.1943-541X.0002189](https://doi.org/10.1061/(ASCE)ST.1943-541X.0002189)
- Kotronis, P., Al Holo, S., Bésuelle, P., & Chambon, R. (2008). Shear softening and localization: Modelling the evolution of the width of the shear zone. *Acta Geotechnica*, 3(2), 85–97. <https://doi.org/10.1007/s11440-008-0061-4>
- Kumar, V., German, M. D., & Shih, C. F. (1981). *Engineering approach for elastic-plastic fracture analysis*. <https://doi.org/10.2172/6068291>
- Li, Y., & Karr, D. G. (2009). Prediction of ductile fracture in tension by bifurcation, localization, and imperfection analyses. *International Journal of Plasticity*, 25(6), 1128–1153. <https://doi.org/10.1016/j.ijplas.2008.07.001>
- Markeset, G., & Hillerborg, A. (1995). Softening of Concrete in Compression-Localization and Size Effects. *Cement and Concrete Research*, 25(4), 702–708.
- Needleman, A. (2016). Effect of size on necking of dynamically loaded notched bars. *Mechanics of Materials*, 116, 180–188. <https://doi.org/10.1016/j.mechmat.2016.09.007>
- Okazawa, S. (2010). Structural bifurcation for ductile necking localization. *International Journal of Non-Linear Mechanics*, 45(1), 35–41.

<https://doi.org/10.1016/j.ijnonlinmec.2009.08.010>

Pan, B., Xie, H., Wang, Z., Qian, K., & Wang, Z. (2008). Study on subset size selection in digital image correlation for speckle patterns. *Optics Express*, 16(10), 7037.

<https://doi.org/10.1364/OE.16.007037>

Pijaudier-Cabot, G., & Bazant, Z. P. (1988). NONLOCAL DAMAGE THEORY By Gilles Pijaudier-Cabot," S. M. ASCE and Zdenek P. BaSant,* F. ASCE. *Journal of Engineering Mechanics*, 113(10), 1512–1533.

Ramberg, W., & Osgood, W. R. (1943). Description of stress-strain curves by three parameters. *National Advisory Committee for Aeronautics*, 1–29.

<https://doi.org/10.1016/j.matdes.2009.07.011>

Rolshoven, S., & Jirasek, M. (2002). Nonlocal formulations of softening plasticity. *WCCMV, Fifth World Congress on Computational Mechanics*, 1–10.

Saif, A., Sarah, O., & Zhen, C. (2019, July 12). Effect of the Post-Peak Behavior on Collapse of Structural Systems. *Structures Congress 2019*, pp. 114–126.

<https://doi.org/doi:10.1061/9780784482247.011>

Salehi, M., & Sideris, P. (2017). Refined Gradient Inelastic Flexibility-Based Formulation for Members Subjected to Arbitrary Loading. *Journal of Engineering Mechanics*,

143(9), 04017090. [https://doi.org/10.1061/\(ASCE\)EM.1943-7889.0001288](https://doi.org/10.1061/(ASCE)EM.1943-7889.0001288)

Schreyer, H. L., & Chen, Z. (1986). One-Dimensional Softening With Localization.

Journal of Applied Mechanics, 53(4), 791. <https://doi.org/10.1115/1.3171860>

Sideris, P., & Salehi, M. (2016). A Gradient Inelastic Flexibility-Based Frame Element Formulation. *Journal of Engineering Mechanics*, 142(7), 04016039.

[https://doi.org/10.1061/\(ASCE\)EM.1943-7889.0001083](https://doi.org/10.1061/(ASCE)EM.1943-7889.0001083)

Yalcinkaya, T., & Lancioni, G. (2014). Energy-based Modeling of Localization and Necking in Plasticity. *Procedia Materials Science*, 3(2004), 1618–1625.
<https://doi.org/10.1016/j.mspro.2014.06.261>

VITA

Saif Altai was born and raised in Babylon City, Iraq. After he finished his high school, he attended the University of Babylon where he earned a Bachelor of Civil Engineering in 2007. In December 2008, he attended the University of Babylon, where he received a Master of Structural Engineering in 2010. From 2011 to 2013, he worked in a private collage as an instructor. In 2013, he granted a scholarship to pursue his PhD degree in the USA. Late 2013, he travelled to the USA to start his study. He started his graduate program in January 2015. After four years, he graduated and earned his PhD degree in Structural Engineering form University of Missouri-Columbia.

G-mail: saifaltai85@gmail.com

This dissertation was typed by Saif Altai